

**BIOMATERIAL TECHNIQUES TO EVALUATE AND ENGINEER
THE TUMOR IMMUNE MICROENVIRONMENT IN BREAST
CANCER AND MELANOMA**

A Dissertation
Presented to
The Academic Faculty

by

Meghan J. O'Melia

In Partial Fulfillment
of the Requirements for the Degree
Doctor of Philosophy in Biomedical Engineering

Georgia Institute of Technology and Emory University
May 2021

COPYRIGHT © 2021 BY MEGHAN J. O'MELIA

**BIOMATERIAL TECHNIQUES TO EVALUATE AND ENGINEER
THE TUMOR IMMUNE MICROENVIRONMENT IN BREAST
CANCER AND MELANOMA**

Approved by:

Dr. Susan N. Thomas, Advisor
School of Mechanical Engineering
Georgia Institute of Technology

Dr. Douglas Graham
Department of Pediatrics
Emory University

Dr. Edward Botchwey
Department of Biomedical Engineering
Georgia Institute of Technology

Dr. Cheng Zhu
Department of Biomedical Engineering
Georgia Institute of Technology

Dr. Andrés García
School of Mechanical Engineering
Georgia Institute of Technology

Date Approved: March 30, 2021

*To my Mom, Grandad, Grammy O, Grandpa, Aunt Kathy, and Great Aunt Jeanne in
honor of their battles with cancer*

And to my Dad and Charlie for their unconditional love and support.

ACKNOWLEDGEMENTS

I want to thank first and foremost, my advisor (the Best BioE advisor), Susan Thomas, for everything she has done for me over the past four and a half years. At every stage of this journey, Susan has been exactly what I needed, pushing me in ways that helped me grow immensely, and supporting me at the times I needed it. I don't think I would be the scientist or person I am today without her guidance and support. Susan balances encouraging high achievement in science, creating opportunities for each of her students to achieve our goals, and showing tremendous care for her students' health and happiness – I don't know how she manages to do it all, but I am incredibly grateful.

Next, I would like to thank current and past members of the Thomas lab whom I've had the honor of working alongside. They've helped me to grow, challenged me, and been a team and support system every step of the way. In particular, I want to thank Dr. Nate Rohner whose work launched mine and who taught me how to deal with mice; Dr. Alex Schudel and Dr. Erin Edwards who first showed me what this level of science looked like and who have been some of my biggest cheerleaders and supporters since I joined the lab; Dr. David Francis, who I shared an office with for most of graduate school, who I learned immunology with, and who I've always been able to have meaningful and productive chats about science with; Dr. Jihoon Kim, one of the most brilliant and kind chemists I have ever met who somehow respected me from the start; my “kids” Paul Archer and Maggie Manspeaker, who I got to teach to work with animals and who have both ended up helping me with their own unique skills; and Lauren Hester, who I had the honor of mentoring for 2 years, and who is without a doubt going to change the world for the better.

I would also like to thank those who I've had the pleasure and honor of collaborating with, and who have served on my committee: Dr. Andrés García, who taught me how to read a paper before I even joined the Thomas lab, has been a close collaborator since 2016, spanning multiple different projects, and funded me as a Cell and Tissue Engineering Training Grant Trainee; Dr. Cheng Zhu, whose long-time collaboration gave me a crash course in T cell immunology, which has been fundamental to this work; Dr. Doug Graham, who with incredible graciousness, let me work with mice in his lab, and has always approached this work with the kindest of words and ideas; and Dr. Ed Botchwey, who has had the perfect insight to push my work forward every single time I present in front of him, no matter the context. I could not have accomplished any of this without all of your support and collaboration.

Finally, I'd like to thank Dr. Ammasi Periasamy, who took a chance on me as a work study student in 2013, and gave me tremendous opportunities, sending me to international conferences and letting me write a first author paper and co-author a textbook chapter as an undergrad; Horst Wallrabe, who taught me most of what I know about cells and did so with the most utmost patience and grace; and Dr. Shagufta Rehman, one of the most caring post docs I have met, who helped make science exciting and fun in Dr. Peri's lab (and made sure I was well fed in college).

There are many other people who made this work possible, so thank you for your help and encouragement throughout the years, it will not be forgotten.

TABLE OF CONTENTS

ACKNOWLEDGEMENTS	iv
LIST OF FIGURES	ix
LIST OF SYMBOLS AND ABBREVIATIONS	xi
SUMMARY	xiv
CHAPTER 1. Introduction	1
1.1 Motivation	1
1.2 Specific Aims	3
1.3 Significance	4
CHAPTER 2. Background and Literature Review	6
2.1 Immunology of Melanoma and TNBC	6
2.1.1 Immune Remodeling in Melanoma and TNBC	6
2.1.2 Immunotherapies for Melanoma and TNBC	8
2.2 The Lymphatic System in Immunity	10
2.2.1 Lymph Formation and Ag Transport	10
2.2.2 Lymphatics in Cancer	13
2.3 Current Systems to Model Cancer <i>In Vivo</i>	15
CHAPTER 3. Quality of CD8⁺ T Cell Immunity Evoked in Lymph Nodes Is Compartmentalized by Route of Antigen Transport and Functional in Tumor Context [118] 17	
3.1 Introduction	17
3.2 Materials and Methods	21
3.2.1 Cell Culture	21
3.2.2 Animal Tumor Models	22
3.2.3 Fluorescent Tracers	22
3.2.4 Tracer Injections	23
3.2.5 In Vivo Imaging System	23
3.2.6 Tumor and LN Immunohistochemistry and Imaging	24
3.2.7 CD8 ⁺ T Cell Isolation	24
3.2.8 Adoptive Transfer	25
3.2.9 Flow Cytometry Analysis	25
3.2.10 Peptide-Conjugated Nanoparticle (NP) Synthesis and Administration	28
3.2.11 Tracer Biodistribution Analysis	28
3.2.12 Ex Vivo Restimulation	29
3.2.13 Tumor Resection Surgery	29
3.2.14 ICB Therapeutic Analysis	30
3.2.15 Statistical Analysis	30
3.3 Results	31

3.3.1	Constitutive Transport Barriers and Mechanisms Regulate Access by LN-resident Immune Cells to Skin-derived Macromolecules	31
3.3.2	Melanomas Mature Peripheral DCs and Alter the Dynamics of Cell-trafficked Ag to dLNs, Resulting in Modified Ag Presentation	34
3.3.3	Melanomas Alter Access of Lymph-derived Nanoscale Solutes and DC Phenotypes within LNs	38
3.3.4	Melanoma dLNs are Niches that Support Survival and Ag Experience by Tumor Ag-specific T Cells	41
3.3.5	Mechanism of Lymphatic Transport Regulates Ag Presentation and T Cell Sensing within the LN	43
3.3.6	Therapeutically Functional Antitumor T Cell Responses in the TME Result from Ag Priming of CD8 ⁺ T Cells within TdLNs	46
3.4	Discussion	51
CHAPTER 4. Tumor-draining Lymph Nodes are Survival Niches that Support T Cell Priming Against Lymphatic Transported Tumor Antigen and Effects of Immune Checkpoint Blockade in TNBC [164]		56
4.1	Introduction	57
4.2	Materials and methods	59
4.2.1	Cell Culture	59
4.2.2	Animal Tumor Models	59
4.2.3	Flow Cytometry Analysis	59
4.2.4	CD8 ⁺ T Cell Isolation	61
4.2.5	Adoptive Transfer	62
4.2.6	Micro-computed Tomographic Imaging (μ CT)	62
4.2.7	Enzyme-linked Immunosorbence Assay (ELISA)	62
4.2.8	Fluorescent Tracers	63
4.2.9	Tracer Injections	64
4.2.10	Tracer Biodistribution Analyses	64
4.2.11	LN Mapping	64
4.2.12	mAb Biodistribution	64
4.2.13	Therapeutic Evaluation	65
4.2.14	Statistical Analysis	65
4.3	Results	66
4.3.1	E0771 Mammary Tumor Growth is Associated with TME-localized Immune Suppression and Vascular Remodelling	66
4.3.2	E0771 Disease Progression Effects on Lymphoid Tissue Immune Microenvironments and Molecular Dissemination from the TME	70
4.3.3	Primary and Secondary TdLNs are Niches Enriched in Factors Derived from the TME that Support Lymphocyte Viability, Ag Experience, and Proliferation	77
4.3.4	Both Primary and Secondary TdLNs are Therapeutic Targets for ICB Immunotherapy	83
4.4	Discussion	85
CHAPTER 5. Novel Engineered <i>In Vivo</i> Platform for Physiologically relevant Breast Cancer Immunotherapeutic Testing		89
5.1	Introduction	89

5.2	Materials and Methods	91
5.2.1	Cell Culture	91
5.2.2	Animal Tumor Models	92
5.2.3	Flow Cytometry	93
5.2.4	Gel Formulation	94
5.2.5	IVIS Imaging	95
5.2.6	μ CT	95
5.2.7	Cytokine Analysis	96
5.2.8	Therapeutic Studies	96
5.2.9	Statistical Analysis	97
5.3	Results	97
5.3.1	Current Mouse Models of Breast Cancer are Insufficient for Immunotherapeutic Testing	97
5.3.2	An Engineered Hydrogel System Induces Consistent and Controllable Breast Tumors	101
5.3.3	Hydrogel-tethered Adhesive Ligands Allow for Induction of Different Immune Microenvironments	104
5.3.4	Novel Engineered System Can Be Used to Test Immunotherapeutic Regimens for Breast Cancer	108
5.4	Conclusion	109
CHAPTER 6.	Conclusions	111
6.1	Conclusions	111
6.2	Contributions to the Field	111
6.2.1	Improved Understanding of T cell Priming and Immune Responses in Melanoma and TNBC	111
6.2.2	Development of Engineered Biomaterial Tools for Preclinical Study	112
6.2.3	Insights into Improved Immunotherapeutic Guidelines for the Treatment of Melanoma and TNBC	113
6.3	Future Directions	114
6.3.1	Synthetic Ag System Uses Beyond CD8 ⁺ T Cell Responses in Melanoma	114
6.3.2	Targeting TdLN in a surgically relevant setting	115
6.3.3	Broad Application of In Vivo Engineered Breast Cancer Model	116
REFERENCES		117

LIST OF FIGURES

Figure 2.2	Mechanism of lymphatic transport alters molecular access within lymph nodes	11
Figure 2.2	LN's are structured to allow for access to different, spatially regulated immune cells	12
Figure 3.1	Engineered systems allow for probing of steps leading to development of anti-tumor CD8 ⁺ T cells	21
Figure 3.2	Hydrodynamic size regulated biomolecular access to different regions and cells of LN's draining site of intradermal injection	32
Figure 3.3	APC migration from the skin to the dLN in naïve and melanoma contexts	35
Figure 3.4	Passive lymphatic drainage in the naïve and melanoma contexts	39
Figure 3.5	The TdLN is a niche that supports Ag-specific CD8 ⁺ T cell priming and survival	42
Figure 3.6	Extent of expansion and quality of Ag-specific CD8 ⁺ T cell pool in response to Ag is dependent on the mechanism of lymphatic transport to the dLN	45
Figure 3.7	Expansion of CD8 ⁺ T cells in TdLN's in response to administration of synthetic Ag systems affects tumor-infiltrating T cells and has antitumor functions	49
Figure 4.1	The tumor immune microenvironment remodels throughout E0771 disease progression and supports poor priming and viability of tumor Ag-specific CD8 ⁺ T cells	67
Figure 4.2	The tumor vasculature remodels throughout E0771 disease progression	69
Figure 4.3	E0771 progression alters lymphoid tissue microenvironments	71
Figure 4.4	Dynamics of macromolecular distribution from the MFP are size-dependent	73
Figure 4.5	Molecular dissemination from breast tumors is altered by E0771 disease and progression	75

Figure 4.6	E0771 disease progression impacts accumulation of intra-MFP injected tracers within inguinal and axillary LNs	78
Figure 4.7	Tumor Ag-specific T cell priming occurs in E0771 TdLNs	80
Figure 4.8	Quality of endogenous CD8 ⁺ T cells within lymphoid tissues and TME changes during E0771 disease progression	82
Figure 4.9	Locoregional administration of mAb directed to either primary or secondary TdLN improves therapeutic and immunomodulatory effects of α PD1 ICB	84
Figure 5.1	Current preclinical models of breast cancer are insufficient	98
Figure 5.2	Engineered hydrogels induce consistent and controllable tumor immune microenvironments	103
Figure 5.3	Adhesive ligands alter immune responses in engineered hydrogels	105
Figure 5.4	Immune status is affected by both tumor-specific and adhesive ligand-specific responses	108
Figure 5.5	Altered tumor immune microenvironments direct responses to immunotherapies	109

LIST OF SYMBOLS AND ABBREVIATIONS

μ CT	Micro-computed tomographic imaging
Ag	Antigen
ANOVA	Analysis of variance
APC	Antigen-presenting cell
AUC	Area under curve
cDC	Conventional dendritic cell
CFSE	Carboxyfluorescein succinimidyl ester
CTLA	Cytotoxic T-lymphocyte-associated protein
DC	Dendritic cell
dDC	Dermal dendritic cell
dLN	Draining lymph node
D-PBS	Dulbecco's phosphate-buffered saline
ELISA	Enzyme-linked immunosorbence assay
FITC	Fluorescein isothiocyanate
FSC	Forward scatter
GEMM	Genetically engineered mouse model
Gzm	Granzyme
ICB	Immune checkpoint blockade
i.d.	Intradermal
IFN	Interferon
i.p.	Intraperitoneal
i.t.	Intratumoral

i.v.	Intravenous
IVIS	<i>In vivo</i> imaging system
LC	Langerhans cell
LEC	Lymphatic endothelial cell
LN	Lymph node
mAb	Monoclonal antibody
MCM	Medullary cord macrophage
MDSC	Myeloid-derived suppressor cell
MFI	Mean fluorescence index
MFP	Mammary fatpad
MHC	Major histocompatibility complex
MP	Microparticle
MSM	Medullary sinus macrophage
NdLN	Non-draining lymph node
NP	Nanoparticle
NSG	NOD scid gamma
pDC	Plasmacytoid dendritic cell
PD1	Programmed death-1
PDL1	Programmed death-ligand 1
PDS-NP	Pyridyl disulfide-functionalized nanoparticles
PDX	Patient-derived xenograft
PE	Phycoerythrin
PEG	Polyethylene glycol
PEG-4MAL	Polyethylene glycol-4 maleimide
RM-ANOVA	Repeated measures analysis of variance

SCS	Subcapsular sinus
SSM	Subcapsular sinus macrophage
TdLN	Tumor-draining lymph node
TME	Tumor microenvironment
TNBC	Triple-negative breast cancer
TNF	Tumor necrosis factor
Treg	Regulatory T cell
TRITC	Tetramethylrhodamine
VEGF	Vaso endothelial growth factor

SUMMARY

Immunotherapy has emerged as the most promising new approach to increase cancer patient survival through its potential to treat both advanced disseminated disease and protect against recurrence. However, response rates in advanced melanoma and the most aggressive and deadliest type of breast cancer, triple-negative breast cancer (TNBC) are disappointingly low: only 20-40% and ~16% of patients, respectively, respond to immune checkpoint blockade (ICB) therapy. Despite immunotherapy's potential in boosting anti-tumor immune response, tumor-induced immune suppression subverts both its development and effects. Overcoming tumor immune suppression, the mechanisms of which are still poorly understood, is thus a critical hurdle to improving the efficacy of immunotherapy in reducing the mortality associated with advanced melanoma and TNBC. Through this research, sophisticated immunological characterization approaches and engineered biomaterial techniques have been applied to preclinical tumor models to analyze and engineer the *in vivo* melanoma and breast tumor immune microenvironment. The central hypothesis of this work is that modeling immune suppression underlying melanoma and TNBC disease progression will reveal mechanisms of immunotherapeutic resistance to inform the development of improved immunotherapeutic strategies. The goal of this work is to utilize bioengineering approaches and techniques to manipulate and analyze immune suppressive mechanisms within the tumor microenvironment (TME) that result in disease progression. This has resulted in the following outcomes: 1) improved understanding of the tumor immune microenvironment throughout the development and progression of melanoma and TNBC; 2) novel models with which to analyze antigen (Ag)

sensing and model the breast TME; and 3) insight into optimal immunotherapeutic strategies for both melanoma and TNBC.

CHAPTER 1. INTRODUCTION

1.1 Motivation

Breast cancer represents the most common cancer among women worldwide, and melanoma is the sixth most common cancer among all people [1–3]. Only ~20% of both breast cancer and melanoma patients survive at least five years after the diagnosis of advanced disease with a high rate of recurrence for both disease types (~15-20% and 41-55%, respectively) [1, 4, 5]. As tumor immune suppression is highly involved in disease development and progression [6], immunotherapy has emerged as the most promising new approach to increase cancer patient survival through its potential to treat both advanced disseminated disease via systemic immune activation and protect against recurrence through immunological memory [7–9]. While the most promising therapeutic strategies for cancer treatment, response rates in advanced melanoma and the most aggressive and deadliest type of breast cancer, TNBC, are disappointingly low: only ~20-40% and ~16% of patients, respectively, respond to ICB therapy [10, 11]. Despite immunotherapy’s potential in boosting anti-tumor immune responses, tumor-induced immune suppression subverts its development and effects. Overcoming tumor immune suppression, the mechanisms of which are still poorly understood, is thus a critical hurdle to improving the efficacy of immunotherapy in reducing the mortality associated with advanced melanoma and TNBC.

The immune system must be locally suppressed for a tumor to develop and progress [6], which allows immunotherapies to be functional in reinvigorating immune responses against the tumor itself [7–9]. However, the immune system is not restricted to the TME;

in fact, the adaptive immune system is housed within the lymphatic system, including secondary lymphoid organs such as LNs [12]. Lymphatic vessels allow for connections between the TME and LNs, with the potential to alter anti-tumor responses [13, 14]. Unfortunately, the role of the lymphatic system and extra-tumoral immune cells throughout tumor development and progression, and their role in immunotherapy responses, are currently poorly understood. The interplay between these systems has the potential to alter the course of immunotherapy drug development and therapeutic strategies and demonstrates an opportunity to fill the current gap in the success of immunotherapies in the clinic.

Currently, the factors which lead to differences in survival after immunotherapeutic treatment are poorly understood – some hypotheses have included expression of PDL1, PD1 or infiltration of certain immune cell subtypes such as CD8⁺ T cells or macrophages [15–18]. These factors have been included in clinical trials [10, 11, 19–21] with limited success, and the lack of appropriate biomarkers is understood to be a significant impediment to development of optimal immunotherapeutic strategies [22–26]. Current preclinical systems are not developed to address the wide variation in immune cell infiltration into the tumor, demonstrating a clear need for improved models, with the potential to better inform clinical responses to immunotherapies.

The **overall goal** of this work is to utilize bioengineering approaches and techniques to manipulate and analyze immune suppressive mechanisms within the tumor microenvironment that result in disease progression. We addressed this need by developing two novel engineered systems, a synthetic Ag system and a novel *in vivo* immunotherapeutic testing platform, which were combined with sophisticated

immunological assays and preclinical models of melanoma and TNBC. The **central hypothesis** of this work is that modeling immune suppression underlying melanoma and TNBC disease progression using biomaterials will reveal mechanisms of immunotherapeutic resistance that will inform the development of improved immunotherapeutic strategies to treat advanced disease. Our engineered biomaterial tools were utilized to test this hypothesis and showed improved responses to both ICB and cancer vaccines in unique ways in both melanoma and TNBC.

1.2 Specific Aims

Specific Aim 1: Evaluate the effects on anti-tumor adaptive response of the remodeled skin microenvironment that develops in melanoma using advanced immune phenotyping techniques and bioengineered technologies. My *working hypothesis* is that tissue remodeling associated with disease progression alters the Ag priming and function of T cells resulting in anti-tumor immune suppression. Using biomaterial-based approaches, I have demonstrated that tumor development effects on response to tumor-derived Ag differ by mechanism of sensing within sentinel lymph nodes (LN), that these sensing methods are altered by remodeling of the tumor during disease progression, and can be reversed by engineered immunotherapies. This work is presented in Chapter 3.

Specific Aim 2: Evaluate and engineer using advanced biomaterial technologies the breast tumor immune microenvironment. My *working hypothesis* is that the microenvironment of developing and progressing breast tumors both redirects and is directed by the development of the anti-tumor adaptive immune response. I have demonstrated that the efficacy of Ag

sensing by T cells is diminished within breast tumors throughout disease progression. However, dissemination of tumor-derived material induces a source of tumor Ag-bathed, stem-like T cells within tumor-draining LNs, which have the potential to respond to immunotherapy. I have shown that these tumor Ag-specific T cells can be harnessed to improve responses to immunotherapy. This work is presented in Chapter 4.

Specific Aim 3: Utilize advanced biomaterial technologies to engineer the breast tumor microenvironment. My *working hypothesis* is that immune infiltration into the breast TME will modulate tumor growth kinetics and responses to immunotherapeutic intervention. I have shown that instructive biomaterials directing myeloid and lymphocytic infiltration into tumors reshapes the tumor growth characteristics. These biomaterial-based approaches have been used to modulate the local immunological microenvironment to better mimic the variety of immune responses to human disease. I have assessed immune microenvironment effects on sensitivity to immunotherapies such as a cancer vaccine to show that local immune microenvironmental milieus alter therapeutic responses. This work is presented in Chapter 5.

1.3 Significance

The work herein generates provides valuable insight into how immunological remodeling impacts tumor development and progression, and how this in turn alters responses to immunotherapeutic strategies. Here, we developed two novel, engineered systems to approach impacts of mechanism of lymphatic dissemination on anti-tumor immune responses; and to more closely mimic immune responses seen in human disease

in an *in vivo* preclinical model. This has allowed us to provide insight into 1) the impacts of Ag dispersal from melanoma tumors resulting in anti-tumor CD8⁺ T cell immunity; 2) impacts of disseminated TNBC Ag on development of a reservoir of Ag-specific T cells; and 3) how local immune milieu impacts responses to cancer vaccines. The knowledge generated across each of these aims was utilized to inform cancer treatment strategies, and demonstrate improved responses to cancer vaccination and ICB therapy in both melanoma and TNBC, and better predict what subgroups of TNBC patients will respond to different types of immunotherapy.

CHAPTER 2. BACKGROUND AND LITERATURE REVIEW

Melanoma is the sixth most common cancer worldwide [2], and breast cancer is the most common cancer among women worldwide [2, 3]. Only ~20% of melanoma patients survive at least 5 years following diagnosis of advanced disease, with ~50% of melanoma patients demonstrate recurring disease [1]. Breast cancer results in the highest deaths due to cancer among women worldwide [2], and TNBC is the most aggressive breast cancer type with the poorest outcomes due to its high propensity to metastasize and limited available treatment modalities [27]. Thus, melanoma and TNBC are significant public health threats requiring further study and show a clear need for improved therapies.

2.1 Immunology of Melanoma and TNBC

Immunotherapy, which focuses on reinvigorating antitumor immune responses, has emerged as the most promising previously unidentified approach to increase patient survival through its potential to both treat advanced disseminated disease and protect against recurrence. However, response rates to ICB, one of the most common clinically applied immunotherapeutics, are only ~10-33% in melanoma patients [28] and ~16% in breast cancer patients [29], demonstrating a clear need for improvement. The immunology of these tumors is highly important in the application and enhancement of these strategies to improve these unfortunate statistics.

2.1.1 Immune Remodeling in Melanoma and TNBC

The immune system is tasked with regulating homeostasis in the body, preventing infection and cancer development while mitigating off-target responses against self-Ag

[30]. However, the immune system can be modified and suppressed, allowing for cancer development and progression [30]. This modification and suppression involves both the innate and adaptive arms of the immune system, along with the cancer cells themselves [30]. The immune system and the manners in which it remodels in TNBC and melanoma are highly complex and currently incompletely understood [30]. However, it is clear that immune infiltration into solid tumors plays an important role in the manner in which disease develops, metastasizes to other tissues, and responds to treatment: dendritic cells (DC) and CD8⁺ T cells are dysfunctional in the human TME [31, 32], and immunosuppressive cell subtypes, regulatory T cells (Treg) and myeloid-derived suppressor cells (MDSC), infiltrate to a high degree [33–36]. However, immune infiltration can also be beneficial in the TME: enhanced melanoma survival is independently associated with the number and phenotype, as measured by granzyme (Gzm) B, interferon (IFN)- γ , programmed death-1 (PD1), and *Tcf1* expression, of CD8⁺ T cells entering tumors [28, 37–41]. Likewise, quantity and quality of CD8⁺ T cells within the TNBC TME are associated with enhanced survival in TNBC patients [42–44].

As mentioned, T cells can play very prominent roles in anti-tumor responses: if properly stimulated, these cells can kill off cancerous cells, preventing the growth of a tumor. However, cytotoxic T cells are often anergic or exhausted within the TME [45, 46], with many T cells exhibiting a regulatory phenotype, contributing to immune suppression [47, 48]. The stimulation of T cells depends upon Ag-presenting cells (APC), including DCs and macrophages, which take up Ag in the periphery or in secondary lymphoid organs, such as LNs, and present it to naïve T and B cells [30]. However, these APCs can be either tolerogenic or stimulatory, which will define the manner in which the T cell is activated.

DCs can present Ag along with costimulatory molecules (such as CD28), leading to efficient T cell stimulation, or they can exist in a tolerogenic state, presenting Ag but low levels of costimulatory molecules and inhibitory molecules (such as programmed death ligand-1 (PDL1)), inducing T cell anergy and Treg activation [49]. Similarly, macrophages can exhibit an M1 phenotype, in which they can prime efficient immune responses against tumor Ag, or an M2 phenotype, facilitating immune suppression [30]. Tumor-associated macrophages tend to be polarized towards the M2 phenotype, making them tumorigenic and creating an immunosuppressive microenvironment [50]. These tumor-associated macrophages facilitate angiogenesis, necessary for tumor growth, along with metastasis, and polarize other immune cells towards immune suppressive phenotypes through the secretion of cytokines and direct cell-cell contact [50]. This immune suppression induced locally can subvert immunotherapeutic intervention, but is currently poorly understood [17, 51], demonstrating the need for further study.

2.1.2 Immunotherapies for Melanoma and TNBC

As the immune system has the potential to mount a response against tumor Ag to induce responses against both disseminated and recurrent disease, immunotherapies have emerged as promising strategies to combat disease. ICB therapy includes anti-cytotoxic lymphocyte-associated protein (CTLA)-4 and anti-PD1 monoclonal antibody (mAb) treatment, which aim to re-energize exhausted and anergic T cells to combat disease [52]. CTLA-4 is expressed by activated T cells, and inhibits CD28 interactions, thus impairing co-stimulatory signaling in these T cells, inducing T cell anergy [53]. Similarly, PD-1 is expressed by T cells which have experienced Ag, and upon engagement, induces T cell exhaustion [54]. Treatments have also focused on targeting the receptor for PD-1, PDL1,

to curtail PD-1 engagement [55]. Currently, atezolizumab, an anti-PDL1 mAb and pembrolizumab, an anti-PD1 mAb, in combination with paclitaxel, are approved for TNBC patients who cannot undergo surgical resection and who show PDL1 expression in tumor biopsies, and are the only ICB strategies approved for breast cancer [29, 56]. Several ICB mAbs are approved for advanced melanoma, including pembrolizumab and nivolumab which target PD-1, and ipilimumab, which targets CTLA-4 [9]. However, responses to ICB are limited to approximately 10% response rates with anti-CTLA-4 treatment and 25-33% with anti-PD-1 treatment in melanoma [52], and ~16% in TNBC patients treated with atezolizumab [29]. Additionally, these therapies lead to significant off-target immune-related adverse effects, limiting their use in the clinic [52].

Cancer vaccines are another promising strategy which aim to enhance DC activation or Ag presentation, improving CD8⁺ T cell-DC interactions for a better immune response. Currently, sipuleucel-T, for use in prostate cancer, and T-VEC, for use in advanced melanoma, are the only FDA-approved cancer vaccines [57, 58]. T-VEC induces durable responses in only ~17% of melanoma patients, with a median survival of 23.3 months [58]. Vaccines have been tested in clinical trials for breast cancer, with ~4 to ~13 months improvement in patient survival compared to standard of care in Phase I-II trials [59, 60]. These vaccine trials demonstrate improvements upon previous therapeutics but are insufficient in their broad application to human disease. As such, while promising, these therapies require additional knowledge and development in order to improve melanoma and TNBC survival clinically.

2.2 The Lymphatic System in Immunity

[Adapted from O'Melia MJ, Lund AW, Thomas SN. (2019), The biophysics of lymphatic transport: engineering tools and immunological consequences. *iScience*. 22:28-43. [12]]

The lymphatic system is composed of a hierarchy of vessels that facilitate directional lymph transport from peripheral tissues to secondary lymphoid organs where adaptive immune responses are initiated. As such, lymphatic vessels are appreciated as necessary physical conduits that facilitate immune surveillance, but an understanding for how changes in lymphatic transport, the movement of lymph, cells, and Ag through this system, is actively regulated during inflammatory processes, and how these changes impact immunity is only beginning to emerge.

2.2.1 *Lymph Formation and Ag Transport*

Lymph is formed in the periphery, where vascular transudate is transported through the interstitium and subsequently enters initial lymphatic capillaries through characteristic gaps between lymphatic endothelial cells (LEC) [61, 62]. Interstitial fluid flows and intralymphatic lymph propulsion is mediated by intrinsic collecting lymphatic pumping and extrinsic physiological forces [63] that drive net directional fluid flow towards lymphatic vessels and ultimately transport lymph and its contents to LNs (Figure 2.1). Lymph itself is composed of soluble proteins, pre-processed Ag, and metabolites [64], which are most effectively transported by lymphatic vessels and accumulate in LNs [65, 66].

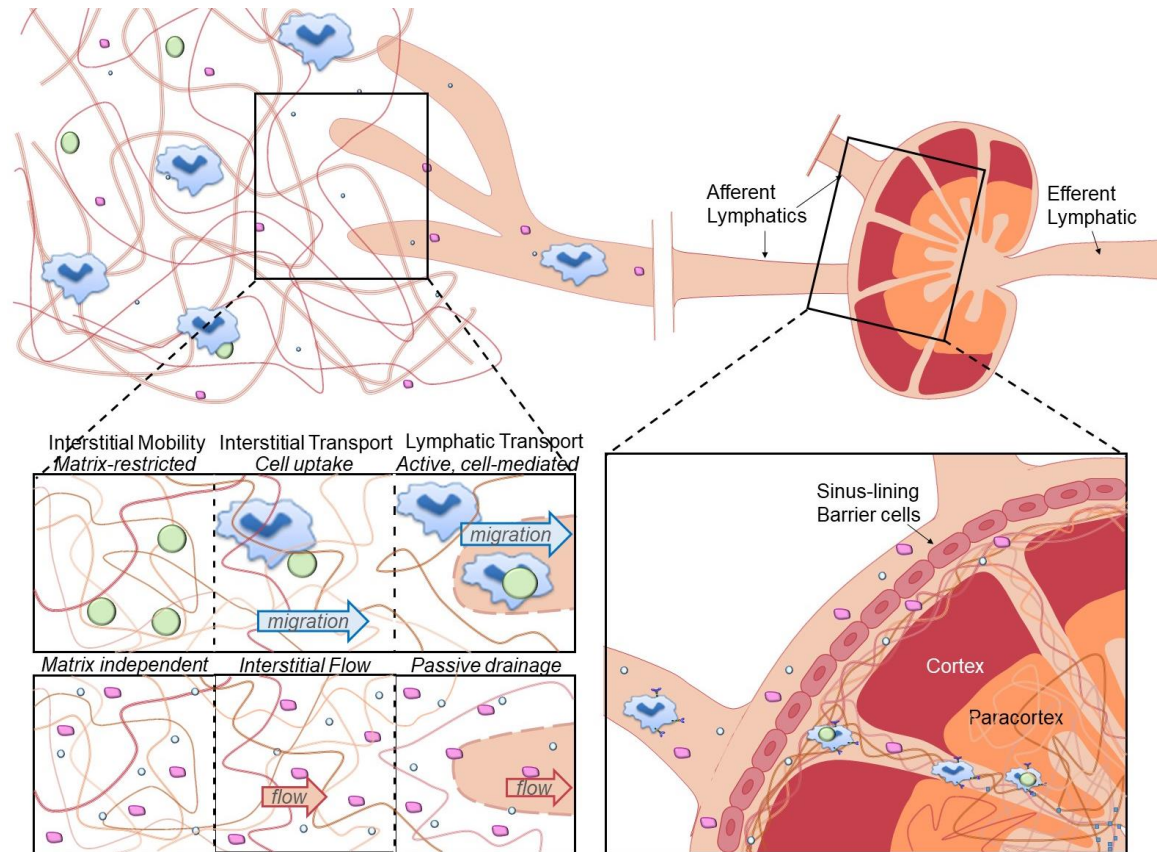


Figure 2.1: Mechanism of lymphatic transport alters molecular access within LNs. Molecular transport within the peripheral tissue and interstitium and into the draining LN.

Afferent lymph enters the LN (Figure 2.2) where cells and Ag are compartmentalized to coordinate and synchronize immune responses. Two layers of LECs facilitate lymph flow through the subcapsular sinus (SCS) and around the LN cortex (Figure 2.2). These specialized LECs support resident SCS macrophages (SSM) [67–69] and DCs [70] that regulate Ag, viral, and bacterial access to B cell follicles for the induction of humoral immunity [68, 71]. Lymph either flows around the SCS or through the LN parenchyma via a network of reticular collagen conduits ensheathed by fibroblastic reticular cells [68, 72–74] (Figure 2.2). Large particulates (>70 kDa), including intact pathogens, are unable to access reticular conduits and are restricted to the SCS, while

soluble Ag moves freely into the paracortical network for sampling by resident DCs [73–76]. Specialized diaphragms in LECs that line the SCS floor actively filter lymph-borne macromolecules and determine the size exclusion properties of the conduits [77].

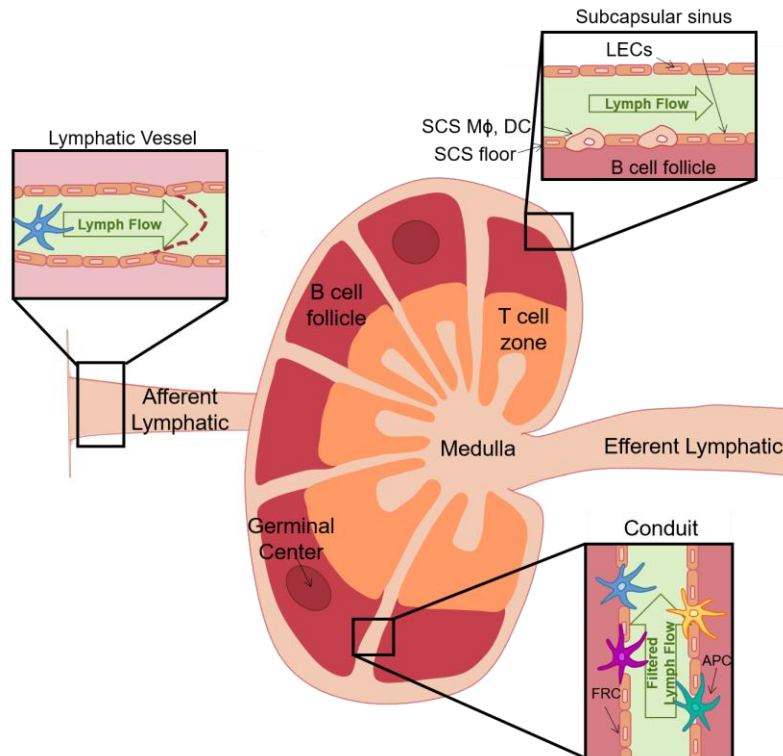


Figure 2.2: LNs are structured to allow for access to different, spatially regulated immune cells. The typical structure of a LN, demonstrating normal partitioning and structures, including the T cell zone, medulla, B cell follicle and germinal center, SCS, conduits, and afferent and efferent lymphatics, is represented, along with enhanced visualization of regions of fluid flows, including flow of lymph through afferent lymphatic vessels and the SCS, and the flow of filtered lymph through the conduit system.

Even in the presence of rapid, soluble Ag transport, active delivery of Ag by migratory, professional APCs is critical to the generation of adaptive immune responses [78] (Figure 2.1). Lymphatic vessels are necessary for DC migration to LNs [79–81], actively facilitate DC homing and transendothelial migration [82–85], and shape

chemokine gradients to permit migration into the LN paracortex [86], making them critical features of an efficient adaptive immune response. It is within the LN paracortex, and specifically along the reticular conduit network that mature resident and migratory DCs interact with naïve T cells in a CCR7-dependent manner [87–89]. Following activation and expansion, T cells exit LNs [90–92] leading to eventual recirculation in the blood and homing to sites of inflammation. It is therefore the movement and filtration of lymph through LNs that determines both cellular localization and Ag distribution to enable rapid development of immune responses following peripheral challenge [93].

2.2.2 *Lymphatics in Cancer*

The contribution of lymphatic vessels and their transport function in cancer progression has long been attributed to their role in regional dissemination of metastatic tumor cells [94]. LN metastasis is associated with poor outcomes across a variety of solid tumor types [94]. In addition to their contribution to metastasis, progressive lymphatic vessel dysfunction in tumors [95] and regional fibrosis significantly alters solute efflux out of tumors. The implications of lymphatic transport on anti-tumor immunity are of increasing interest to the field. Tumor-associated lymphangiogenesis drives intratumoral inflammation that at baseline favors immune suppression [96] but is more readily activated by immunotherapy [97] indicating enhanced tumor-host communication. Consistently, complete loss of dermal lymphatic vessels dampens host tumor recognition leading to an immunologically cold TME [98]. These studies argue that the extent to which lymphatic vessels are engaged with a developing tumor is a significant control point for host immune responses.

The major site for the priming of anti-tumor immune responses is the tumor-draining LN (TdLN) [13]. Tumor Ag transport through lymphatic vasculature is maintained by both passive and active mechanisms (Figure 2.1) [65, 93, 99, 100]. This provides a role for TdLNs in contributing to the regulation of T cell priming and Treg function [13, 79], implicating the TdLN in the development of anti-tumor immune responses. However, in the context of disease, the TdLN is often suppressed: Tregs and MDSCs expand in both the human melanoma and breast cancer TdLNs [34, 35, 101–103], implying tumor-mediated immune suppression within the TdLN which diminishes immune responses to disease. Biophysical remodeling also alters the local TdLN microenvironment, with altered tissue stiffness and intranodal pressures [104], and enhanced fibroblastic reticular cell leakiness in TdLN barriers [105], with the potential to alter anti-tumor immunity. However, the remodeling and its effects on Ag processing and presentation, along with ultimate effects on the development of anti-tumor immune responses, are poorly understood.

In addition to the role lymphatic vessels play as active conduits to TdLNs, evidence indicates that, at least in skin, tumor-associated lymphatic vessels may directly inhibit effector lymphocyte accumulation and function through multiple mechanisms. Tumor-associated and LN-resident LECs scavenge and cross-present tumor Ag leading to the dysfunctional activation of naïve CD8⁺ T cells [96, 106]. Furthermore, recent data indicated that peripheral LECs in melanoma and non-malignant skin activate expression of PDL1 in an IFN γ -dependent manner [107]. Loss of IFN γ receptor specifically in lymphatic vessels interrupted crosstalk with infiltrating cytotoxic T cells and improved CD8⁺ T cell-mediated tumor killing in murine melanomas. This suggests direct lymphatic vessel-

mediated control of effector immunity within peripheral tissues. Lymphatic vessels, and their transport function, along with the TdLN are consequently emerging as active, relevant, and targetable players in anti-tumor responses and immunotherapy.

2.3 Current Systems to Model Cancer *In Vivo*

As the immune system is highly complex, and tumors are extremely heterogeneous systems, all current systems to model immune-lymphatic-tumor interaction have limitations in their applicability to human disease. The current preclinical gold standard lies in mouse models, including patient-derived xenografts (PDX), genetically engineered mouse models (GEMM), and syngeneic models [108]. In PDX models, patient-derived samples are implanted into immunocompromised or humanized animals, where tumors grow and develop [109]. However, the need to perform these studies in immunocompromised animals makes the study of the immune system and its interaction with tumors impossible, and humanized animals can be prohibitively expensive. Additionally, only ~40% of attempts to generate PDX in immunocompromised mice are successful, a rate even lower in humanized animals [109]. Finally, immune responses to PDX in humanized mice don't always match human responses [110–112], making PDX inefficient as models to improve currently poor clinical responses. In GEMMs, animals are genetically engineered to express certain genes, such as the polyoma tumor virus, under the restriction of different parts of the genome [26, 113]. The MMTV-PyMT model consists of the polyoma tumor virus under the control of the mouse mammary gene, leading to spontaneous development of breast tumors [114], and is used in a portion of this work. While the closest model of pathological characteristics of human disease, these tumors are hard to control and can show significant variation between animals [26, 113], making

studies challenging to perform and often adding difficult to impossible to control for variables. In syngeneic models, mouse tumor cells are implanted into mice of the same strain, where they tend to form tumors [115–117]. These can be done orthotopically to improve relevance of the microenvironment interactions with the tumor. Syngeneic tumors allow for rapid tumor formation of tumors in immunocompetent animals in a consistent fashion, making them very useful for application to immunotherapy development [116-118]. However, these models still suffer from very short latency times (much shorter than human disease), unreliable and variable immune responses, and reliance on implantation of foreign material for tumor development, decreasing their applicability to human disease. Thus as a whole, each type of preclinical model is limited, particularly for the improvement of immunotherapeutic strategies.

CHAPTER 3. QUALITY OF CD8⁺ T CELL IMMUNITY EVOKED IN LYMPH NODES IS COMPARTMENTALIZED BY ROUTE OF ANTIGEN TRANSPORT AND FUNCTIONAL IN TUMOR

CONTEXT [118]

Revealing the mechanisms that underlie the expansion of antitumor CD8⁺ T cells that are associated with improved clinical outcomes is critical to improving immunotherapeutic management of melanoma. How the lymphatic system, which orchestrates the complex sensing of Ag by lymphocytes to mount an adaptive immune response, facilitates this response in the context of malignancy is incompletely understood. To delineate the effects of lymphatic transport and tumor-induced lymphatic and LN remodeling on the elicitation of CD8⁺ T cell immunity within LNs, we designed a suite of nanoscale biomaterial tools enabling the quantification of Ag access and presentation within the LN and resulting influence on T cell functions. The expansion of Ag-specific stem-like and cytotoxic CD8⁺ T cell pools was revealed to be sensitive to the mechanism of lymphatic transport to LNs, demonstrating the potential for nanoengineering strategies targeting LNs to optimize cancer immunotherapy in eliciting antitumor CD8⁺ T cell immunity.

3.1 Introduction

Melanoma remains a significant clinical problem, representing the sixth most common cancer worldwide, with only ~20% of patients surviving at least 5 years following diagnosis of advanced disease and ~41 to 55% of patients demonstrating recurrent disease [1]. Immunotherapy, which focuses on reinvigorating antitumor immune responses, particularly on the part of T cells, has emerged as the most promising previously

unidentified approach to increase patient survival through its potential to both treat advanced disseminated disease and protect against recurrence. However, response rates in advanced melanoma are disappointingly low: only ~10 to 33% of patients respond to ICB therapy [10]. Enhanced survival is independently associated with several features of a robust antitumor CD8⁺ T cell immune response including the number of these cells within the tumor [28]. More specifically, higher levels of CD8⁺ T cells expressing GzmB, a marker of degranulation, and IFN- γ , an inflammatory cytokine, along with immune checkpoint Ag experience marker PD1, within the tumor are associated with improved survival [37–39]. The abundance of CD8⁺ T cells expressing PD1 in combination with transcription factor *Tcf1*, which marks a stem-like cell subtype with high proliferative potential and capacity to differentiate into cells with antitumor lytic functions [40, 41], is also a prognostic indicator in melanoma [38, 39]. Thus, the generation of both high-quantity and high-quality Ag-primed T cells in the TME is an important step in inducing effective antitumor immunity, the holy grail to broaden the benefits afforded by cancer immunotherapy.

To this end, the generation of a large and robust pool of tumor-specific CD8⁺ T cells, the target of ICB and many other immunotherapeutic strategies, relies on the priming of T cells by APCs [9]. The activation status and Ag presentation by APCs, which include DCs and macrophages, affect the differentiation of naïve T cells and, thus, their resulting functionality. To facilitate Ag sensing by rare cognate T cells, encounters with APC-presented Ag are tightly orchestrated within lymphocyte-rich secondary lymphoid organs. These include LNs, whose structure is specialized to facilitate both tight interactions between immune cell subsets [12] and Ag dispersal among cell subtypes that are locally distributed in a spatially prescribed manner (Figure 2.2). Specifically, Ag derived from peripheral tissues accesses LNs by lymphatic vessel-mediated lymph drainage to the downstream, draining LN (dLN) [12, 13, 65]. This lymph enters the LN at the SCS, a

barrier lined with fibroblastic reticular cells, APCs, and LECs [12]. From the SCS, lymph-borne solutes diffuse into the LN cortex, where B cells, other APCs, and intrafollicular T cells reside [12, 74, 75] or, in a highly size-restricted manner, enter conduits to reach the T cell zones of the LN paracortex [12, 73, 74]. APCs also patrol peripheral tissues before migration to dLNs under both steady-state and inflamed conditions [13, 65, 99, 100] to disperse in a chemotactically driven manner amongst discrete LN zones [78, 99, 100, 119, 120]. Ag access to strategically distributed APCs colocalized with LN-resident lymphocytes is, thus, dependent on a number of barriers that are sensitive to the mechanism of transport to the LN.

In response to disease, both the tumor and dLN remodel in cancer, with potential impacts on Ag sensing and the resulting magnitude and functions of the antitumor immune response. TME-localized immunosuppression has been widely recognized as a cancer hallmark [121] with consistent and advancing suppression occurring throughout tumor development and progression [6]. In particular, T cell activation in the TME was impaired [28, 38, 39] and tumor-associated DCs show high PD1 ligand and B7 family expression, two features associated with impaired prognosis [39]. Likewise, immunosuppressive tumor-associated macrophages [50] as well as Tregs and MDSCs infiltrate the TME to high extents [17]. Melanomas [122, 123], similar to other cancer types [124–127], have also been shown to have high peritumoral lymphatic expansion, a feature associated with increased lymphatic metastasis [124–127]. As such, multiple immunosuppressive pathways active within the TME have the potential to be recapitulated within LNs downstream of primary tumors (so-called sentinel LNs or TdLNs). These include suppressed T cell responses by tumor-induced MDSCs, inhibition of DC-mediated T cell priming, and local persistence of Tregs [101, 102]. Moreover, cellular components of LN structures also remodel in cancer. For example, fibroblastic reticular cells, which help to maintain the SCS of the LN [128, 129], exhibit increased permeability and activation in

melanoma [105]. Similarly, biophysical features of the remodeled TME associated with tumor immune suppression [130, 131] have been observed to be modified in TdLNs, including alterations in tissue stiffness and intranodal pressures [104] that parallel changes within LNs in other immune-related pathologies [132–134]. How these remodeling pathways affect the distribution of tumor-derived Ag among cells within the TdLN to modulate the development of Ag-specific T cell immunity, however, remains undefined.

In this work, we designed a suite of biomaterial tools (Figure 3.1a) to enable the analysis of lymphatic transport, cellular association, and Ag presentation to delineate the concerted influence of these interrelated processes on the generation of CD8⁺ T cell immunity within LNs. This includes a tracer system for the evaluation of macromolecular transport via lymphatic vessels to cells within the dLN (Figure 3.1b-c) and a synthetic Ag system to evaluate Ag presentation and its sensing by T cells (Figure 3.1d). We applied these systems to assess the impacts of lymphatic transport mechanism on Ag accessibility to and presentation by cells of the dLN, the resulting functions of the expanded Ag-specific CD8⁺ T cell pool, and how each of these processes is modified in the tumor context. CD8⁺ T cell immunity elicited within TdLNs was found to be compartmentalized by route of lymphatic transport and to remain therapeutically functional in a melanoma mouse model. These results provide previously unknown insight into how immunotherapeutic strategies for melanoma could be improved by leveraging the unique microenvironment and Ag-sensing capabilities of TdLNs.

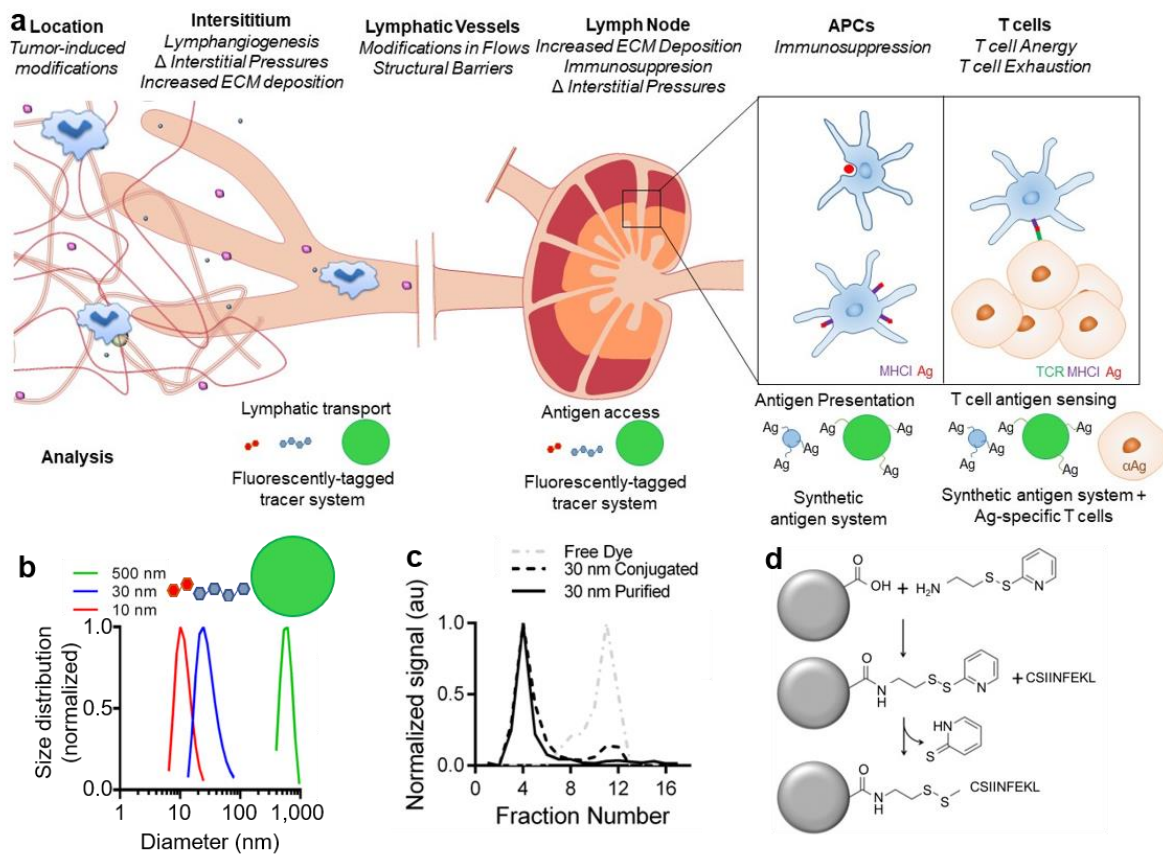


Figure 3.1: Engineered systems allow for probing of steps leading to development of anti-tumor CD8⁺ T cells. (a) Schematic diagram of tumor-induced modifications in the tumor interstitium, lymphatic vasculature, dLNs, APCs, and T cells with potential ramifications on lymphatic transport and T cell Ag-sensing, along with systems used to analyze each step of Ag access and T cell Ag sensing. Dynamic light scattering measurements (b) and representative size exclusion chromatography (c) of tracers post fluorescent labeling. (d) Chemical method of COVA₂₅₇₋₂₆₄ peptide conjugated to MP or NP.

3.2 Materials and Methods

3.2.1 Cell Culture

B16F10 and B16F10-OVA mouse melanoma cells (obtained from Swartz Laboratory, EPFL, Lausanne, Switzerland) were cultured in Dulbecco's modified Eagle medium (Gibco, Thermo Fisher Scientific Inc., Waltham, MA) with 10% heat-inactivated

fetal bovine serum (Gibco, Thermo Fisher Scientific Inc.) and 1% penicillin-streptomycin-amphotericin B (Life Technologies, Carlsbad, CA). Cells were passaged at ~70-80% confluency and maintained at 37°C with 5% CO₂ within a standard cell culture incubator.

3.2.2 *Animal Tumor Models*

C57Bl/6 or B6 CD45.1 mice were purchased at 6 wks of age from the Jackson Laboratory (Bar Harbor, ME). All protocols were approved by the Institutional Animal Care and Use Committee. For tumor-bearing cohorts, 0.5 x 10⁶ melanoma cells were intradermally implanted into the left dorsal skin of 6- to 8-wk-old mice. Tumor dimensions were measured with calipers in three dimensions and reported as ellipsoidal volume.

3.2.3 *Fluorescent Tracers*

Five hundred-nm yellow-green and red fluorescent (505/515 and 580/605 excitation/emission, respectively) carboxylate-modified microspheres (MP) were purchased from Thermo Scientific, Inc. Tetramethylrhodamine isothiocyanate (TRITC) dextran (40 kDa, 10 nm) was purchased from Sigma-Aldrich. Amino-dextran (500 kDa, 30 nm) (Thermo Scientific, Inc.) was covalently labeled by incubation with Alexa Fluor 647 or Alex Fluor 700 *N*-hydroxysuccinimide ester dyes (Thermo Scientific, Inc.) in 0.1 M NaHCO₃ at pH 8.4 for 4 h on a tube rocker. Alexa Fluor 647 and Alexa Fluor 700 dextran-dye conjugates were purified from unreacted free dye by Sepharose CL-6B gravity column chromatography after conjugation (Figure 3.1c). Purified dextran-fluorophore conjugates were further confirmed free of unconjugated dye by a second Sepharose CL-6B column analysis [65]. All reagents were used and maintained under sterile conditions.

Hydrodynamic sizes were confirmed before injection by dynamic light scattering using a Zetasizer Nano ZS (Malvern Instruments Ltd., Malvern, UK; Figure 3.1b).

3.2.4 *Tracer Injections*

Fluorescent tracers suspended in saline were co-infused by a syringe pump at a rate of ~300nL/s directly into the center of the tumors for tumor-bearing groups or into the dermal layer of the skin for naïve groups, using a 27- to 31- gauge needle (Beckton Dickinson, Franklin Lakes, NJ) while mice were under anesthesia via isoflurane. For biodistribution experiments, 500 nm red or yellow-green fluorescent microspheres (19 pM), 30 nm Alexa Fluor 700 or Alexa Fluor 647 dextran (4.8 μ M), and 10 nm TRITC dextran (4.8 μ M) were co-infused in 10 μ L saline total. Mice were euthanized via CO₂ asphyxiation in accordance with American Veterinary Medical Association and local Institutional Animal Care and Use Committee guidelines at the prescribed times after tracer injection for each experiment.

3.2.5 *In Vivo Imaging System*

Animals were injected intratumorally (i.t.) in the left dorsal skin with Alexa Fluor 647-conjugated NPs or 500 nm yellow-green microspheres as described above. Twenty-four h after NP injection or 72 h after MP injection, animals were euthanized via CO₂ asphyxiation in accordance with American Veterinary Medical Association and local Institutional Animal Care and Use Committee guidelines. Animals were then dissected to expose axillary and brachial LNs and imaged using a PerkinElmer *in vivo* imaging system (IVIS) Spectrum CT (Waltham, MA). LNs were then dissected and placed on black plastic and imaged using a PerkinElmer Spectrum CT.

3.2.6 *Tumor and LN Immunohistochemistry and Imaging*

Tumor, skin, and dLNs were frozen in optimum cutting temperature compound (Sakura Finetek USA Inc., Torrance, CA) in 2-methylbutane (Sigma-Aldrich) chilled by liquid nitrogen and frozen tissue blocks immediately stored at -80°C. For imaging of tracer dLNs, coverslips were mounted onto LN slices (10- μ m thickness) using Vectashield mounting medium (Vector Laboratories, Burlingame, CA) with no prior wash steps and within 30 min of imaging. Otherwise, LN, skin, and tumor tissue sections were fixed with pre-chilled acetone for 10 min at 4°C and subjected to standard immunofluorescence protocols using the following antibodies, which were obtained from Thermo Fisher Scientific, Inc. unless otherwise specified: fluorescein isothiocyanate (FITC)-conjugated rat anti-mouse CD31 (1:50), rabbit anti-mouse Lyve-1 (1:250), Alexa Fluor 633 goat anti-rabbit (1:300), Armenian hamster anti-mouse CD3E (1:50), Alexa Fluor 647 goat anti-hamster (1:300, Abcam plc., Cambridge, MA), Alexa Fluor 488-conjugated rat anti-mouse CD169 (1:100; BioLegend Inc., San Diego, CA), biotinylated rat anti-mouse F4/80 (1:200, Life Technologies), streptavidin-Alexa Fluor 555 (1:400, Life Technologies), biotinylated rat anti-mouse B220 (1:250), and Alexa Fluor 488-conjugated Armenian hamster anti-mouse CD11c (1:50; Biolegend, Inc.). Blocking and antibody dilutions were performed in 10% donkey serum (Sigma-Aldrich) in Dulbecco's phosphate-buffered saline (D-PBS). Slides were washed with 0.1% Tween 20 (Sigma-Aldrich) in D-PBS for washing steps, counterstained with 4',6-diamidino-2-phenylindole (VWR International Inc.), and imaged using a 710 NLO confocal microscope (Carl Zeiss Microscopy Ltd., Jena, Germany) with a 20x magnification objective.

3.2.7 *CD8⁺ T Cell Isolation*

OT-I animals were purchased from Charles River Laboratories (Lyon, France) and bred in-house. OT-I animals were euthanized, and the spleens were harvested and disrupted with 18G needles (Becton Dickinson) followed by washing with D-PBS. Cells were passed through a sterile 70- μ m cell strainer (Greiner Bio-One, Monroe, NC), washed, and incubated with ACK Lysing Buffer (Lonza Group AG, Basel, Switzerland) for 60 s at room temperature, quenched with D-PBS, washed, and resuspended for counting. Cells were resuspended at 10^8 cells/mL buffer (2% bovine serum albumin in D-PBS), blocked with normal rat serum, and mixed with CD8⁺ T cell isolation antibody cocktail (Stemcell Technologies, Vancouver, Canada), followed by streptavidin-coated magnetic beads (Stemcell Technologies). Buffer was added to the mixture and placed in a magnet (Stemcell Technologies) and the supernatant was collected. Cells were then counted and resuspended in carboxyfluorescein succinimidyl ester (CFSE; Life Technologies) and then quenched with ice-cold RPMI medium containing >10% heat-inactivated fetal bovine serum (Life Technologies). Purity, viability, and CFSE labeling were confirmed via flow cytometry on a customized BD LSRFortessa before adoptive transfer. Cells were maintained in sterile conditions before adoptive transfer.

3.2.8 Adoptive Transfer

Isolated CD8⁺ T cells were suspended in sterile saline at a concentration of 2×10^6 cells per 200 μ L of sterile saline. After induction of isoflurane anesthesia, the hair over the neck of mice was removed using depilatory cream and cleaned using warm water and ethanol wipes, and suspended cells were injected intravenously (i.v.) via the jugular vein.

3.2.9 Flow Cytometry Analysis

Axillary and brachial dLNs were pools and incubated with collagenase D (1mg/mL) (Sigma-Aldrich) in D-PBS with calcium and magnesium for 1 h at 37°C, passed through a 70- μ m cell strainer (Greiner Bio-One), washed, and resuspended in a 96-well U-bottom plate (VWR International, Inc.) for staining. Spleen capsules were disrupted using 18G needles, and the cell suspension was passed through a 70 μ m strainer, pelleted and then incubated with red blood cell lysis buffer (Sigma-Aldrich) for 7 min at room temperature, diluted with D-PBS, washed, and resuspended. All antibodies for flow cytometry were obtained from BioLegend, Inc. unless otherwise stated. Cells were blocked with anti-mouse CD16/32 (clone, 2.4G2) (Tonbo Biosciences, San Diego, CA) for 5 min on ice, washed, and then stained with a fixable viability dye eFluor 455UV (1:1000; eBioscience, San Diego, CA) for 15 min on ice or fixable viability dye Zombie Aqua (1:100; BioLegend Inc.) for 30 min at room temperature, before quenching with 0.1% bovine serum albumin in D-PBS (flow cytometry buffer). Antibodies were prepared in flow cytometry buffer at the following dilutions on the basis of preliminary titrations: phycoerythrin (PE) anti-mouse CD45.2 (1.25:100), Alexa Fluor 700 anti-mouse CD25 (0.5:100), Brilliant Violet 785 anti-mouse PD1 (1.25:1000), Alexa Fluor 647 anti-mouse CXCR5 (0.5:100), PerCP anti-mouse CD3 (2.5:100), APC-Cy7 anti-mouse CD8 (2.5:100), PE-Cy7 anti-mouse CD39 (5:100), and Brilliant Violet 421 anti-mouse CD44 (5:100) for T cell distribution analyses; Brilliant Violet 711 anti-mouse CD45.1 (1.25:100), Brilliant Violet 605 anti-mouse CD3 (2.5:100), APC-Cy7 anti-mouse CD8 (2.5:100), and Brilliant Violet 786 anti-mouse PD1 (1.25:100), PerCP anti-mouse CD69 (1.25:100) or PerCP anti-mouse CD45 (0.5:100) for T cell restimulation analysis; PerCP anti-mouse CD45 (0.625:100), Brilliant Violet 711 anti-mouse CD3 (1.25:100), FITC anti-mouse CD8 (0.3125:100), Brilliant

Violet 786 anti-mouse PD1 (1.25:100), PE-Cy7 anti-mouse CD39 (2.5:100), and Alexa Fluor 700 anti-mouse CD25 (1:100) for T cell vaccination response studies; PE-Cy7 anti-mouse CD11b (0.625:100), Brilliant Violet 421 anti-mouse CD11c (5:100), Brilliant Violet 605 anti-mouse CD169 (5:100), Brilliant Violet 650 anti-mouse B220 (2:100), Brilliant Violet 711 anti-mouse CD3 (1.25:100), Brilliant Violet 785 anti-mouse F4/80 (2.5:100), and PE anti-mouse H-2K^b:SIINFEKL (5:100, clone 25D1.16) for Ag presentation experiments; or PerCP anti-mouse CD45 (1.25:100), Alexa Fluor 700 anti-mouse CD11b (1.25:100), PE-Cy7 anti-mouse CD11c (1.25:100), APC-Cy7 anti-mouse MHC-II (2.5:100), Brilliant Violet 605 anti-mouse CD206 (5:100), PE anti-mouse CD86 (5:100), APC anti-mouse DEC205 (1:100), and Brilliant Violet 711 anti-mouse B220 (1.25:100) for DC phenotyping experiments. Cells were fixed with 4% paraformaldehyde (VWR International Inc.) for Ag presentation and biodistribution experiments. For intracellular staining, cells were incubated with FoxP3/Transcription Factor Fixation/Permeabilization solution (eBioscience) for 60 min on ice in the dark. Cells were then incubated with PE anti-mouse Tcf1 (1.25:100; Beckton Dickinson), APC anti-GzmB (2.5:100), and Brilliant Violet 605 anti-Ki67 (1.25:100) in FoxP3/Transcription Factor Fixation/Permeabilization buffer (eBioscience) for 75 min on ice in the dark. For *ex vivo* cytokine staining, cells were resuspended in IC Fixation Buffer (eBioscience) for 60 min at room temperature in the dark. Cells were then incubated with APC anti-mouse GzmB (2.5:100), PE anti-mouse IFN- γ (1.25:100), AF700 anti-mouse interleukin (IL) -2 (0.5:100), and PE-Cy7 anti-mouse tumor necrosis factor (TNF)- α (1.25:100) in IC Permeabilization Buffer (eBioscience) for 60 min at room temperature in the dark. Cells were then resuspended in flow cytometry buffer and kept at 4°C until analyzed with a customized BD LSRFortessa (BD

Biosciences). Compensation was performed using AbC, ArC or UltraComp compensation beads (Thermo Fisher Scientific Inc.) and data analyzed using FlowJo software version 10 (FlowJo LLC, Ashland, OR).

3.2.10 Peptide-Conjugated Nanoparticle (NP) Synthesis and Administration

Pyridyl disulfide-functionalized NPs (PDS-NPs) were prepared as previously described [135]. Cysteine-modified OVA₂₅₇₋₂₆₄ (CSIINFEKL) was dissolved in Mill-Q water at 1 mg/mL and added 1:1 to PDS-NPs (40 mg/mL). The disulfide displacement reaction proceeded overnight at room temperature with stirring. After reacting, COVA₂₅₇₋₂₆₄-NP was separated from unreacted peptide by size exclusion chromatography using a CL-6B column. Fractions containing peptide were identified by reacting with fluorescamine, and polyethylene glycol (PEG)-containing fractions (NPs) were determined using an iodine assay. Fractions containing COVA₂₅₇₋₂₆₄-NP were combined and concentrated to the appropriate dose using 30 kDa molecular weight cutoff spin filters and sterilized by filtration through a 0.22 µm syringe filter. COVA₂₅₇₋₂₆₄-conjugated NP or MP in sterile saline were injected intradermally in the center of the tumor or into the dermal layer of the skin (naïve animals) of C57/B16 mice.

3.2.11 Tracer Biodistribution Analysis

At 4, 24, and 72 h after tracer injection, mice were euthanized, and the tumor-draining axillary and brachial LNs were harvested and homogenized in D-PBS using 1.4-mm acid-washed zirconium grinding beads with a FastPrep-24 automated homogenizer. Whole-tissue homogenate fluorescence was measured with a Synergy H4 BioTek plate reader (BioTek Instruments, Inc., Winooski, VT), compensation was applied, and

fluorescent tracer amounts and concentrations were calculated from standard curves made by spiking individual naïve homogenates with tracer solution. Tracer concentration within tissues was calculated by application of standard curves generated in tissue homogenates to the fluorescent readouts. To determine percent injection, this concentration was multiplied by a dilution factor to account for the PBS added to the tissue after excision and the portion of the tissue measured on the plate reader (tubes were weighed before tissue was added, after homogenization, and after plating to determine dilution factor). Percent injection was then defined as the amount of tracer divided by the known amount of tracer injected into the animal. We note that in these experiments, only total fluorescence is measured via end point analyses. As such, this method cannot distinguish between rates of lymphatic drainage versus LN accumulation.

3.2.12 Ex Vivo Restimulation

After cell isolation (as above, in flow cytometry), 30% of LN samples, 5% of spleen samples, or 5% of tumor samples were plated in a sterile 96-well U-bottom plate. SIINFEKL peptide (1 $\mu\text{g}/\text{mL}$) in 200 μL Iscove's modified Dulbecco's medium with 10% heat-inactivated fetal bovine serum and 0.05 mM β -mercaptoethanol (Sigma-Aldrich) was added to each sample and then incubated for a total of 6 h at 37°C with 5% CO_2 . Three hours into the incubation period, brefeldin A (50 $\mu\text{g}/\text{mL}$) (Sigma-Aldrich) was added to each sample. Cells were then stained for flow cytometry as above.

3.2.13 Tumor Resection Surgery

Animals were anesthetized using isoflurane in oxygen and then given sustained-release buprenorphine (1 mg/kg) and ketoprofen (5 mg/kg) via intraperitoneal injection as

analgesics. The animals were then placed on a warming bed, and a sterile drape was placed to expose only the tumor and surrounding skin. Povidone-iodine was applied to the skin three times to sterilize the surgical area. Sterile scissors were then used to excise and remove the tumor. Sterile wound clips were used to close the wound. The animal was monitored throughout recovery and returned to its cage. Wound clips were removed 10 d after surgery, and animals are monitored every other day to ensure well-being and examined for infection or irritation surrounding the surgical site. All procedures were approved by the local Institutional Care and Use Committee.

3.2.14 ICB Therapeutic Analysis

On d 7 of B16F10-OVA tumor growth in CD45.1 mice, isolated, CFSE-labeled CD8⁺ OT-I T cells (CD45.2⁺) were administered intravenously via the jugular vein. On d 9 of B16F10-OVA tumor growth, 150 µg of each of anti-PD1 mAb and anti-CTLA-4 mAb was administered either intraperitoneally (i.p.) or intradermally (i.d.) in the forelimb, which results in mAb accumulation within the TdLN but not non-draining LNs (NdLN) [14]. Saline administered i.d. in the forelimb served as control. Animals were euthanized on d 11, and lymphocyte responses were analyzed as described above.

3.2.15 Statistical Analysis

Data are represented as the means accompanied by SEM, and statistics were calculated using Prism 6, 7, and 8 software (GraphPad Software Inc., La Jolla, CA). Statistical significance was defined as $p < 0.05$, 0.01, 0.005, and 0.001, unless otherwise specified. Area under the curve was calculated using the built-in Prism analysis tool

3.3 Results

3.3.1 *Constitutive Transport Barriers and Mechanisms Regulate Access by LN-resident Immune Cells to Skin-derived Macromolecules*

A panel of fluorescent tracers [65, 66] was co-infused into the skin of naïve animals and, at various times after administration, dLNs were analyzed for both total levels of tracer accumulation as well as tracer distribution profiles among resident leukocytes. Thirty and 10 nm dextrans (500 and 40 kDa, respectively) versus 500 nm polystyrene spheres were implemented to compare the extents of lymphatic transport from the periphery – passive lymph drainage versus active transport mediated by emigrating APCs (Figure 3.1).

Ten and 30 nm dextrans accumulated within the dLN at early time points after injection, particularly in the SCS (Figure 3.2a). Correspondingly, an increasing depth of penetration by 10 nm relative to 30 nm dextrans was observed in the parenchyma of dLNs (Figure 3.2b, top), as would be expected given the size exclusion barrier of quiescent (noninflamed) LN conduits [73–75]. MP (500 nm) instead appreciably accumulated at detectable levels within dLNs only 1 to 3 d after injection (Figure 3.2a) and, in contrast to smaller dextran tracers, did so not within the SCS of dLN but instead deeper in the LN parenchyma (Figure 3.2b, bottom, and c). As a result, small dextrans accumulated within the LN far more capsule-proximally compared to the large spheres (Figure 3.2c). This is consistent with the dextrans having been transported by direct uptake into lymph after injection and drainage into dLNs, as is supported by high levels of dLN accumulation at all analyzed times after injection, as well as their restriction to the SCS. Contrastingly, larger spheres were not appreciably detected within dLNs by confocal imaging until after

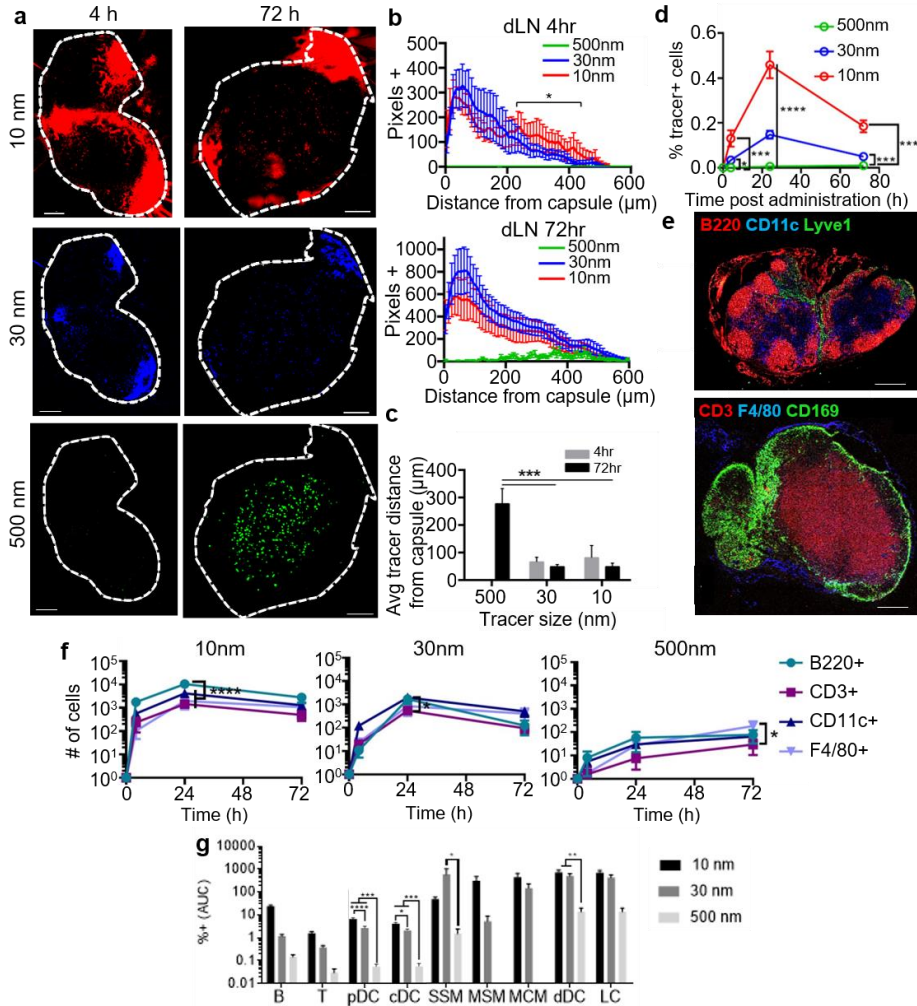


Figure 3.2: Hydrodynamic size regulates biomolecular access to different regions and cells of LNs draining site of intradermal injection. (a-c) Ten, 30 and 500 nm tracer distributions within LN draining the intradermal injection site 4 and 72 h after administration. (d) Total number of tracer⁺ cells within dLNs 4, 24, and 72 h after intradermal injection, as measured by flow cytometry. (e) Immunohistochemically measured distributions of cellular subtypes within LNs. (f) Frequencies of marker-positive cells of total CD45⁺ cells that are tracer positive within LNs draining the injection site 4, 24, and 72 h after intradermal administration, assessed flow cytometrically. (g) Tracer uptake within each cell type analyzed as area under the curve (AUC) from 0-72 h. Scale bars, 200 μm ; * indicates significance by two-way analysis of variance (ANOVA) (b-d) or one-way ANOVA (f) with Tukey's comparison (* indicates $p < 0.05$, * indicates $p < 0.005$, **** indicates $p < 0.001$). $n = 5-8$ mice; a-d and f are representative of at least two independent experiments.**

the 4 h analysis time point. Likewise, the 500 nm tracer appears as punctate points primarily deeper within the parenchyma of the LN, in the locations accessed by skin migratory cells [99, 100, 119]. This is consistent with their transport to dLNs being mediated by cells migrating from the peripheral tissue of administration, a process that transpires more slowly [99, 100, 119]. Resulting levels of total cells within dLNs that associated with tracers were highest for dextrans directly transported via lymph compared to the overall very low level of total 500 nm sphere association with dLN cells (~100 to 1000x difference). The 10 nm dextran associated with a higher number of cells (~5x) compared to 30 nm dextran (Figure 3.2d), a result consistent with the 10 nm dextrans' capacity to more deeply penetrate the LN parenchyma (Figure 3.2a and b) despite overall lower levels of dLN accumulation.

Within LNs, leukocyte distributions are tightly organized in a spatially defined manner, with B cells (the substantial majority of B220⁺ dLN-resident cells), DCs (predominantly CD11c⁺), and SCS macrophages (CD169⁺) versus T cells (CD3⁺) being more LN capsule proximal versus distal, respectively (Figure 3.2e). To determine the effects of lymphatic transport mechanism on patterns of leukocyte uptake, tracer uptake was flow cytometrically assessed using a cell extraction protocol that liberated leukocyte populations of analyzed LNs [136, 137]. Consistent with their distinct patterns of spatial distributions within dLNs, tracers of different sizes exhibited differential access to not only differing numbers of dLN-resident cells (Figure 3.2d) but also differing leukocyte (CD45⁺) subtypes (Figure 3.2f). In particular, 10 nm tracers were found to accumulate at all measured times most prodigiously in B cells, again consistent with their efficient transit into LN conduits after accumulation within the SCS (Figure 3.2f, left) [99, 100, 119]. In

contrast, the 30 nm tracer, which, once transited to the LN, was more restricted to the SCS, was found within more DCs rather than B cells (Figure 3.2f, middle). Further differentiation into more defined cell subtypes [B cells, T cells, plasmacytoid DCs (pDC), conventional DCs (cDC), SSM, medullary sinus macrophages (MSM), medullary cord macrophages (MCM), dermal DCs (dDC), and Langerhans cells (LC)] revealed the 30 but not the 10 nm tracer to be restricted to the LN-resident phagocytic leukocytes positioned at the sinus, while the 500 nm tracer was primarily within the skin migratory cells, e.g., dDCs and LCs (Figure 3.2g). Constitutive barriers to lymphatic transport and transit into the LN parenchyma via conduits thus substantially influence the resulting distribution of tracers among LN-resident leukocytes.

3.3.2 Melanomas Mature Peripheral DCs and Alter the Dynamics of Cell-trafficked Ag to dLNs, Resulting in Modified Ag Presentation

Tumors locally modulate the functions of APCs, which are necessary for the effective generation of antitumor immunity. As such, tumor effects on APCs within TdLNs were evaluated. DCs in both skin/tumor and dLNs of day 10 B16F10 melanoma-bearing mice were found to exhibit both higher CD86 and lower CD206 [by both number of cells and mean fluorescence index (MFI) of positive cells] among DEC205⁺ DCs (both dDCs and LCs) compared to naïve animals (Figure 3.3a-b). Thus, melanomas induce maturation and decreased tolerogenicity among skin-derived DCs in both the tumor and the dLN, with potential effects on DC trafficking, phagocytosis, and Ag presentation.

In addition to the immunological microenvironment, tumors also induce local remodeling of the tissue interstitium and vasculature, hallmarks of disease [121] likely to

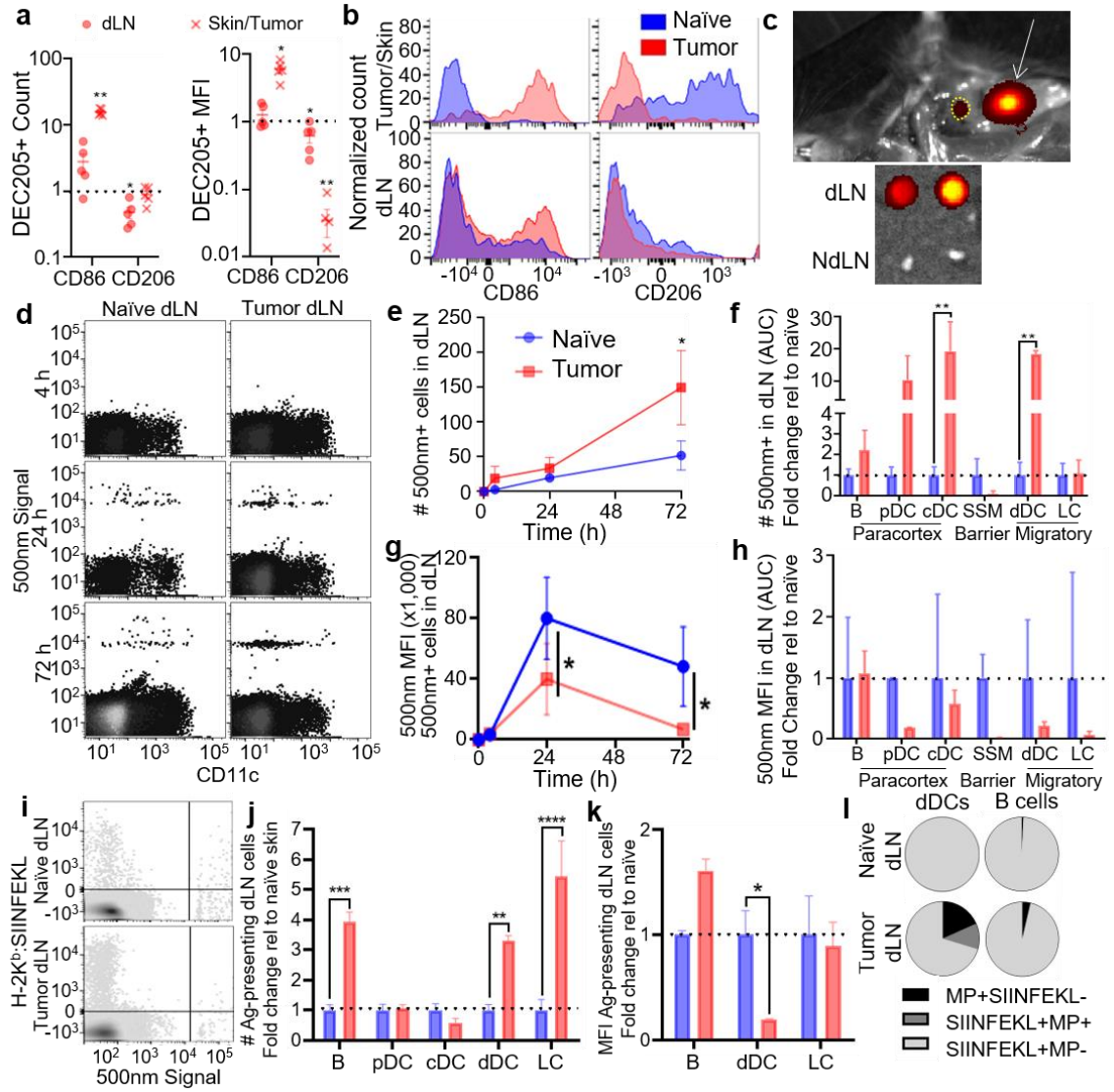


Figure 3.3: APC migration from the skin to the dLN in the naïve and melanoma contexts. CD86 and CD206 signal (a-b) in CD11c⁺DEC205⁺ cells of the skin or tumor and dLN of naïve and d 10 B16F10-bearing animals, with the MFI and number of cells expressing CD86 and CD206 quantified, both normalized to values in the naïve skin/LNs. (c) IVIS imaging showing a site of 500 nm injection (white arrow) and LN drainage (yellow dashed circle), demonstrating specific accumulation in dLNs after 72 h (positive pixels as collected by IVIS imaging are red-yellow, negative background is grey scale). (d) Accumulation of 500 nm tracer⁺ cells in the dLN over time, analyzed flow cytometrically. (e) 500 nm accumulation among CD45⁺ cells in LNs draining skin or d 7 B16F10 melanomas over time, assessed flow cytometrically. (f) Fold change in the AUC (0 to 72 h) of number of cells containing MPs within the dLN relative to naïve accumulation. MFI of MP fluorescent signal (g) in LNs draining the MP-injected skin or B16F10 melanomas over time of all MP-containing cells, and as fold change of AUC (0 to 72 h) within

individual cell subtypes relative to naïve tissues at 4, 24, and 72 h (h). (i) Representative flow cytometry plots of 500 nm tracer uptake and Ag presentation, as assessed by 25 D1.16 staining for H-2K^b:SIINFEKL 72 h after Ag-MP injection into naïve skin or d 7 B16F10 melanomas. Number (j) and MFI (k) of cells presenting SIINFEKL Ag in the TdLN relative to the naïve skin dLN at 72 h after Ag-MP administration as determined by 25D1.16 staining for H-2K^b:SIINFEKL. (l) MP and H-2K^b:SIINFEKL (SIINFEKL) positivity among dLN B cells and dDCs in naïve and tumor contexts 72 h after Ag-MP administration. * indicates significance by one-way ANOVA; n=5-6 animals (*indicates p<0.05, ** indicates p<0.01, * indicates p<0.005, **** indicates p<0.0001); d-h are representative of at least two independent studies.**

influence lymphatic transport and resulting Ag access within the TdLN. B16F10 melanomas, for example, exhibit increased lymphatic vascularization and T cell infiltration compared to the naïve skin, recapitulating spontaneous melanoma models [105]. As such, the tracer panel (Figure 3.1) was implemented to probe lymphatic transport effects on Ag access and how this is affected by disease. After injection into d 7 B16F10 tumors, 500 nm tracers were transported to TdLNs (Figure 3.3c) and were associated with dLN-resident cells at extents greater than those seen in LNs draining the naïve skin, as determined by flow cytometric measurement of tracer fluorescence (Figure 3.3d-e). Of the migratory cells assessed, numbers of 500 nm⁺ dDCs but not LCs were increased (Figure 3.3d, f). Numbers of 500 nm⁺ cDCs, an LN-resident cell subtype, were also increased (Figure 3.3d, f), presumably due to tracer handoff from immigrating 500 nm⁺ cells [78, 138]. As mature APCs tend to be more migratory [120, 139], this is in line with changes in APC maturation induced by the tumor (Figure 3.3a-b). When evaluated on a per-cell basis, more cells within dLNs were 500 nm⁺ overall (Figure 3.3e), although among all CD45⁺ 500 nm⁺ cells, 500 nm tracer MFI was decreased at both 24 and 72 h after injection in tumor-bearing animals compared to naïve animals (Figure 3.3g). Likewise, the 500 nm MFI trended downward within individual cell subtypes (Figure 3.3h). These data can be interpreted in two ways.

As tumors induce APCs to mature and become more migratory, they may also become less phagocytic, bringing less Ag per cell to the dLN. It is also possible that decreases in measured per-cell tracer MFIs result from tracer dilution within the TME because of rapidly growing tissue mass. Nevertheless, these data demonstrate that, overall, APC trafficking from the skin is sustained within melanomas.

As alterations in APC maturation, total migrating cell numbers, and their carried payload are likely to affect Ag presentation within dLNs, animals were subjected to antigenic challenge via an engineered synthetic Ag system. In this configuration, 500 nm MP were covalently attached via a disulfide linkage that is reversible within the reducing intracellular environment of APCs to the H-2K^b peptide of chicken ovalbumin (OVA₂₅₇₋₂₆₄) with an N-terminus cysteine [140, 141] (Figure 3.1d). These COVA₂₅₇₋₂₆₄-MPs were injected into the skin of naïve or tumor of B16F10 melanoma-bearing animals, and Ag presentation was assessed 72 hours later through measurement of H-2K^b:OVA₂₅₇₋₂₆₄ staining (Figure 3.3i) [142]. Consistent with the known transfer of lymphatic-transported Ag between LN-resident cells [78, 138], most cells presenting Ag within dLNs were found to not contain the 500 nm MP (Figure 3.3i). Examining all H-2K^b:OVA₂₅₇₋₂₆₄⁺ cells, numbers of lymph-migrating dDCs and LCs along with LN-resident B cells presenting Ag were found to be increased by the tumor (Figure 3.3j). However, Ag presentation by dLN-resident cDCs or pDCs was not modified by the presence of a tumor (Figure 3.3j). Simultaneously, the amount of Ag presented by each H-2K^b:OVA₂₅₇₋₂₆₄⁺ dDC (flow cytometrically assessed per cell MFI) was lower in LNs draining Ag-MP-injected tumors compared to LNs draining Ag-MP-injected skin (Figure 3.3k). LCs and B cells, on the other hand, exhibited Ag presentation MFI that was unchanged in the tumor compared to

the naïve context (Figure 3.3k). The increase in the number of Ag-presenting LCs, which interact primarily with CD8⁺ T cells [99, 119, 143], thus suggests an increase in presentation of tumor-derived Ag to LN-resident CD8⁺ T cells in melanoma-bearing animals. dDCs, on the other hand, are reported to prime/interact with CD4⁺ T cells and B cells [99, 119, 143]. The diminished ratio of Ag-presenting MP⁺ cells (Figure 3.3l) is suggestive of dDCs transferring Ag for presentation by B cells (Figure 3.3i and l), thus providing a mechanism for enhanced presentation of peripheral tissue-derived Ag to B cells of the dLN, a hypothesis that requires further experimentation to confirm. These results overall suggest that changes in APC maturation and migration induced by the tumor result in enhanced access of 500 nm MP to TdLN cells as well as increased Ag presentation by dDCs, LCs, and B cells within TdLNs.

3.3.3 Melanomas Alter Access of Lymph-derived Nanoscale Solutes and DC Phenotypes within LNs

Disease influences on lymph-draining Ag accumulation and uptake by cells within dLNs were next interrogated. Tracers 30 and 10 nm in hydrodynamic diameter simultaneously administered as one injection into d 7 B16F10 melanomas accumulated within TdLNs over 72 h at reduced levels compared to that seen in dLNs after injection into naïve skin (Figure 3.4a). Nevertheless, levels of both 30 and 10 nm tracer association with B cells within TdLNs remained high with respect to per-tracer positive cell MFI over 72 h (Figure 3.4b, left, and c). With respect to pDCs, which reside more distal from the LN SCS within the LN parenchyma and are thus more restricted from lymph access [144], tracer association was increased within tumor- compared to naïve skin-dLN (Figure 3.4b, right, and c). This is consistent with the increased permeability of the LN fibroblastic

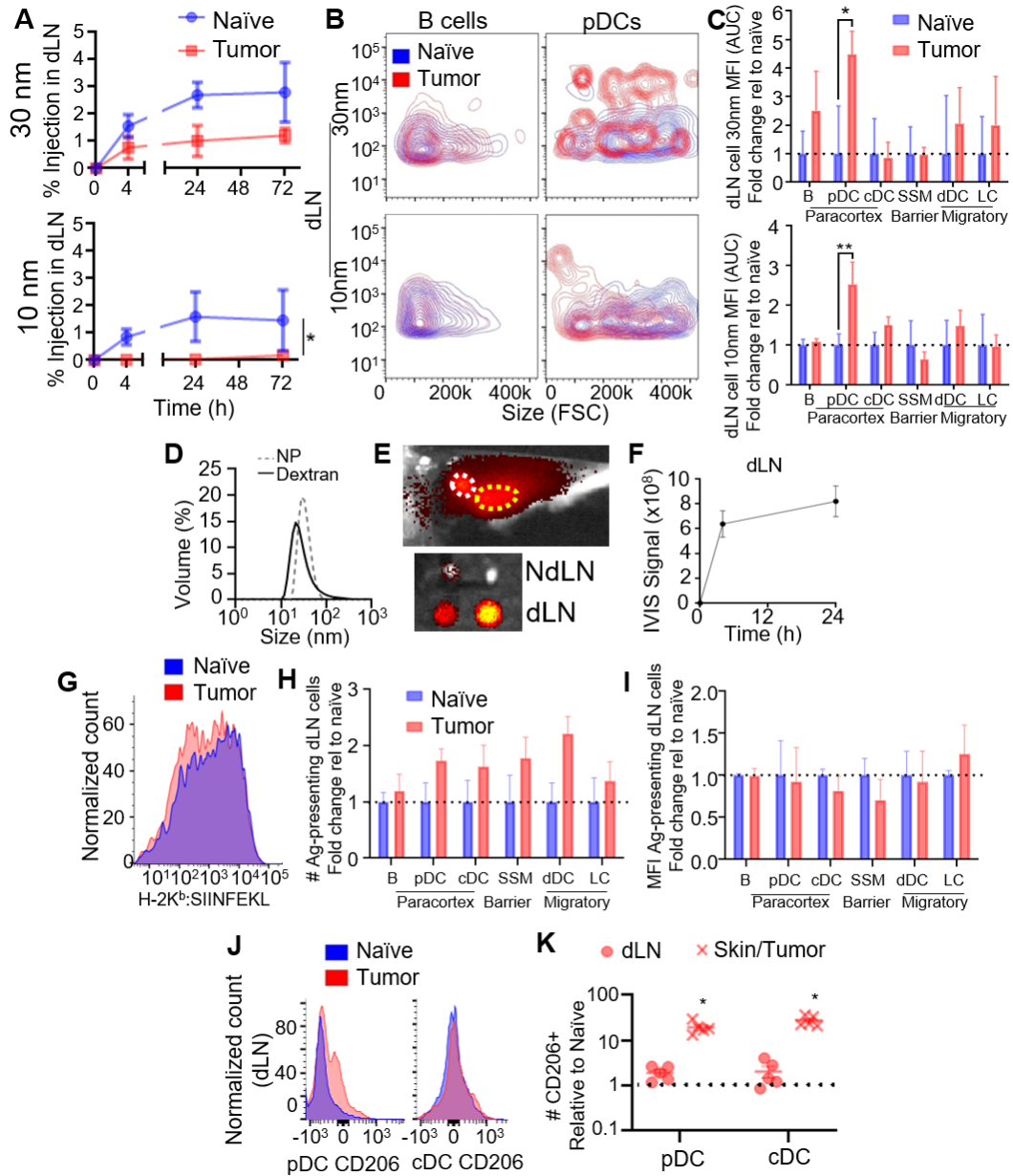


Figure 3.4: Passive lymphatic drainage in the naïve and melanoma contexts. (a) Thirty and 10 nm dextran bulk accumulation in LNs draining skin or d 7 B16F10 melanomas over time. **(b)** Representative flow cytometry plots of 30 and 10 nm dextran accumulation within B cells and pDCs of the dLN. FSC, forward scatter. **(c)** MFI of 30 and 10 nm tracer signal in LNs draining the skin or B16F10 melanomas over 72 h after injection (AUC). **(d)** Dynamic light scattering measurements of 500 kDa (30 nm) dextrans and Ag-NPs. **(e)** NPs (30 nm) injected intradermally accumulate within axillary (white circle) and brachial (yellow circle) dLNs 24 h after intradermal injection (positive pixels as collected by IVIS imaging are red-yellow, negative background is grey scale), quantified in **(f)**. Flow cytometry histograms of Ag presentation (25D1.16 staining for H-2K^b:SIINFEKL) among

CD45⁺ cells within dLNs (g), number of dLN cells presenting Ag relative to naïve condition (h), and as MFI of H-2K^b:SIINFEKL signal of positive dLN cells (i) 24 h after intradermal injection of Ag-NP. CD206 signal (j) among pDCs and cDCs in the skin/tumor and dLN of naïve and d 10 B16F10-bearing animals, quantified in (k), normalized to values in naïve skin and dLN. * indicates significance by one-way ANOVA with Tukey's comparison (* indicates $p < 0.05$, ** indicates $p < 0.01$); n=5-6 animals; a-f are representative of at least two independent experiments.

reticular cell-lined conduits within LNs draining melanomas [65, 105], suggesting that 30 nm tracers in TdLNs are available to be sampled by previously inaccessible cell types within LNs draining the naïve (tumor-free) skin. These results suggest that despite disease-induced alterations in lymphatic drainage, TdLN remodeling sustains access of lymph-draining solutes to resident leukocytes.

The influence of these changes in lymph-borne nanoscale solute access by TdLN cells on Ag presentation was assessed using the synthetic Ag system instead composed of COVA₂₅₇₋₂₆₄ disulfide tethered to lymphatic-draining NP composed of Pluronic-stabilized poly(propylene sulfide) NPs [13, 140, 141, 145–147]. By virtue of their size (Figure 3.4d), these NPs transit the interstitium, drain into lymphatic vessels, and accumulate rapidly within the dLN (Figure 3.4e) for prolonged times after injection (Figure 3.4f) in a manner similar to that of the fluorescent dextran tracers (Figure 3.4d). Administration of these lymph-draining Ag-NPs thus allows cross-presentation by APCs of lymph-accessed Ag to be assessed through measurement of H-2K^b:OVA₂₅₇₋₂₆₄ staining. Lymph drainage of Ag tethered to the NPs administered intratumorally did not result in increased numbers of cross-presenting total (Figure 3.4g) or individual cell subtypes within TdLNs (Figure 3.4h), nor was the mean per-cell MFI of H-2K^b:OVA₂₅₇₋₂₆₄ staining altered relative to naïve dLNs (Figure 3.4i). Consistent with this, CD206 expression, which is associated with DC tolerogenicity [148], was enhanced among pDCs within both the tumor and the TdLN and

among cDCs of the tumor (Figure 3.4j-k). This suggests that despite increased tracer access (Figure 3.4b-c), cross-presentation of lymph-borne Ag by LN-resident APCs, which overall exhibit higher tolerogenicity, is unaffected by the tumor. This is in opposition to trends in Ag presentation resulting from Ag-MP treatment phenotype (Figure 3.3a-b), further motivating the elucidation of the ramifications of these lymphatic transport mechanism-specific changes on T cell Ag sensing in the tumor context.

3.3.4 Melanoma dLNs are Niches that Support Survival and Ag Experience by Tumor Ag-specific T Cells

Changes in Ag presentation and phenotype of APCs induced by melanomas have the potential to substantially affect Ag sensing and responses by T cells. As such, CD8⁺ T cell immunity that develops against endogenous tumor Ag in various immune microenvironments of melanoma-bearing animals was interrogated. Both the tumor and TdLNs were found to be highly enriched in presented tumor Ag in animals bearing d 7 B16F10 melanomas that expressed OVA (Figure 3.5a-b). Accordingly, proliferation 72 h after transfer of tumor Ag-specific (OT-I) CD45.2⁺ cells into recipient CD45.1 mice bearing B16F10-OVA tumors 7 d after implantation was extensive in both the tumor and its TdLNs but not the NdLN or spleen (Figure 3.5c). With respect to the density of live tumor Ag-specific donor cells per total live cells, proliferating OT-I donor cells were highly concentrated in the TdLN but not other analyzed tissues (Figure 3.5d). Notably, however, proliferating donor CD8⁺ T cells within the tumor exhibited low or poor viability, in contrast to cells within TdLNs (and to a lesser extent, NdLNs and spleens) that were largely viable (Figure 3.5e-f). Frequencies of PD1 but not CD39 expressing donor CD8⁺ T cells, which have presumably experienced Ag but did not become exhausted [54, 149], within

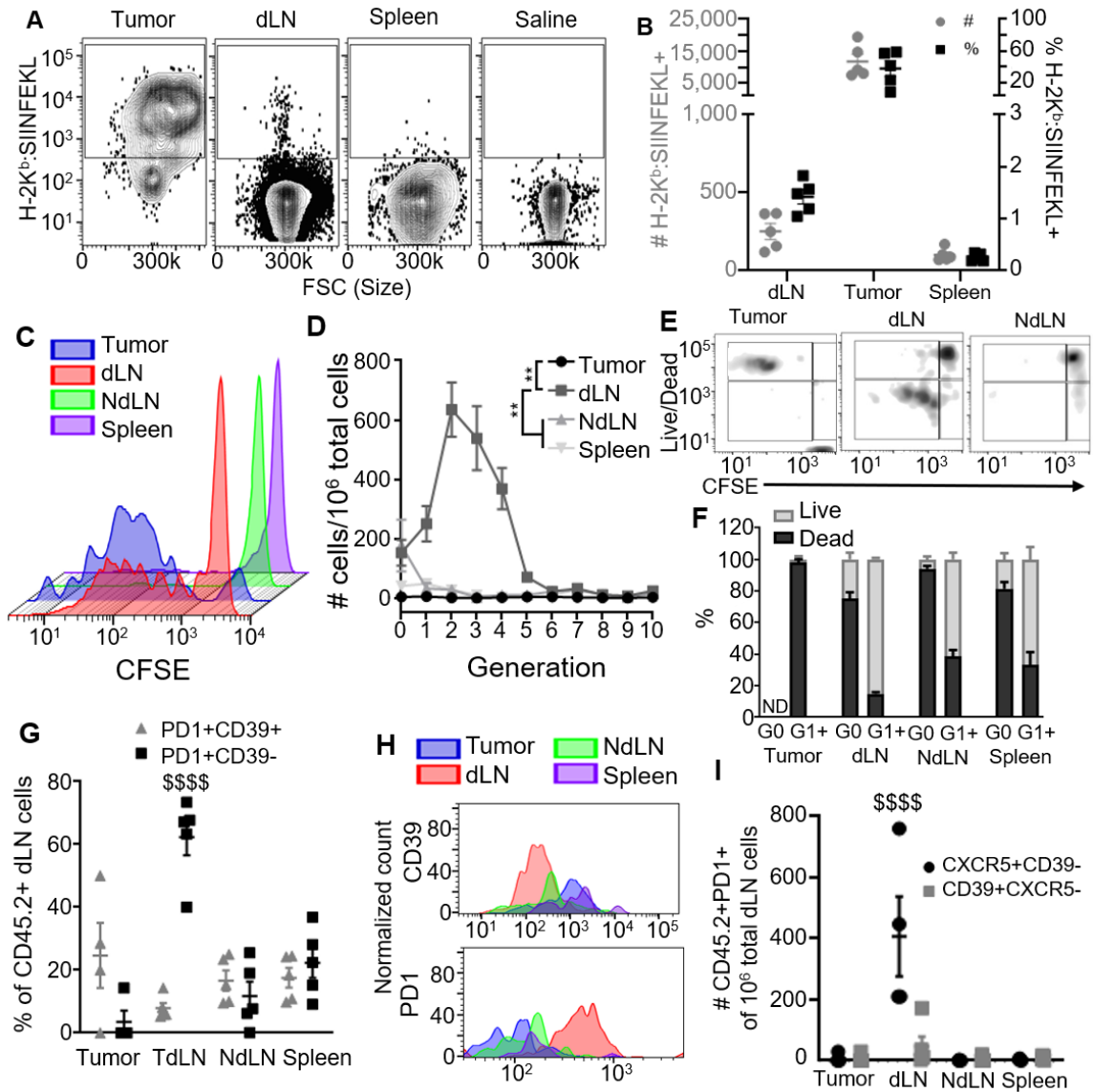


Figure 3.5: The TdLN is a niche that supports Ag-specific CD8⁺ T cell priming and survival. SIINFEKL presentation (measured by 25D1.16 staining for H-2K^b:SIINFEKL) by CD45⁺ cells (a) and cDCs (b) of the tumor, dLN, and spleen in B16F10-OVA tumor-bearing animals. Representative CFSE dilution histograms (c) showing proliferation by tumor Ag-specific CD45.2⁺ donor cells in the tumor, dLN, NdLN, and spleen 72 h after transfer into d 7 tumor-bearing CD45.1 animals, as quantified in (d). Representative flow cytometry plots (e) and quantification (f) of proliferative generation (CFSE signal) and viability of tumor Ag-specific donor cells in the tumor, dLN, and NdLN. Phenotype of tumor Ag-specific donor cells in the tumor, dLN, NdLN, and spleen 72 h after transfer into d 7 tumor-bearing CD45.1 mice: CD44, CD39, and PD1 expression quantification (g) and representative histograms (h); CXCR5 and CD39 expression quantification (i). * indicates significance by two-way ANOVA with Tukey's comparison (** indicates p<0.01); \$

indicates significance relative to all other groups by two-way ANOVA with Tukey's comparison (\$\$\$\$ indicates $p < 0.0001$); $n = 5-8$ animals; a-i are representative of two experiments.

TdLNs were also high, in contrast to donor cells measured within tumors, spleens, and NdLNs (Figure 3.5g-h). Densities of a stem-like subtype of PD1-expressing donor CD8⁺ T cells that are CXCR5⁺CD39⁻, which provide the proliferative burst in response to anti-PD1 ICB therapy [40, 41], were greater in TdLN compared to the tumor, spleen, and NdLN (Figure 3.5i). Thus, the TdLN supports the enhanced proliferation and survival of tumor Ag-specific CD8⁺ T cells, a subset of which is stem-like [40, 41], in contrast to the tumor and other lymphoid tissues, and could act as a source of tumor Ag-specific T cells to regulate antitumor immunity and response to immunotherapy.

3.3.5 Mechanism of Lymphatic Transport Regulates Ag Presentation and T Cell Sensing within the LN

To assess how the mechanism of lymphatic transport of Ag from peripheral tissues to dLNs influences response by Ag-specific CD8⁺ T cells localized to within dLNs (Figure 3.6a), the synthetic Ag system that leverages either an MP or NP carrier to restrict lymphatic transport to dLN via cell-mediated versus passive lymph drainage, respectively, was administered into naïve animals. Responses 3 d after administration by both recipient CD8⁺ T cells and donor CD45.2 OT-I CD8⁺ T cells adoptively transferred 1 d before Ag challenge (Figure 3.6b, i) or endogenous CD8⁺ T cells 7 d after administration (Figure 3.6b, ii) were subsequently monitored. As would be expected given programmed proliferation by CD8⁺ T cells in response to Ag experience [150], the extent of proliferation by responding T cells within dLNs 3 d after Ag challenge was equivalent between animals

challenged with NPs versus MPs for both responding donor and recipient cells (Figure 3.6c). However, NP-mediated Ag challenge resulted in sustained high levels of dLN CD8⁺ T cells, whereas the number of CD8⁺ T cells after MP challenge was reduced at 7 d after challenge (Figure 3.6d). This suggests that CD8⁺ T cells primed via NPs versus MPs exhibit differences in their dLN recruitment, retention, and/or viability during response to Ag priming. Consistent with the substantially higher levels of PD1⁺ cells within dLNs compared to MP-primed cells both 3 and 7 d after challenge (Figure 3.6e-f). More PD1⁺ donor cells 3 d and endogenous cells 7 d after Ag challenge were also Tcf1⁺Tim3⁻ (Figure 3.6f), indicating that antigenic priming via drained NPs results in greater expansion of stem-like CD8⁺ T cell pool within dLNs compared to cell-trafficked MP-tethered Ag. The number of recipient/endogenous CD25⁺ T cells was somewhat higher 3 but not 7 d after MP challenge, a difference not seen in donor cells (Figure 3.6e-f). Functional responses assessed by *ex vivo* restimulation with OVA₂₅₇₋₂₆₄ revealed more GzmB⁺ and IFN γ -producing donor cells 3 days after challenge in response to MP- as opposed to NP-mediated Ag challenge (Figure 3.6g-h). Numbers of GzmB-expressing cells within dLNs were also higher in response to Ag challenge using MPs compared to NPs both 3 and 7 d after treatment, and IFN- γ -producing cells were higher in OT-I cells responding to MP challenge at d 3 (Figure 3.6g-h).

Together, these results reveal that Ag sensing and elicitation of functional cytotoxic CD8⁺ T cells are compartmentalized between the mechanism of Ag transport to dLNs. Specifically, lymphatic transport to dLNs via trafficking APCs leads to induction of T cells with more cytotoxic functions. However, lymph drainage of Ag results in higher overall levels of Ag experience with dLNs, effects reflected by higher numbers of induced PD1⁺

cells and the generation of more stem-like CD8⁺ T cells. Both of these cell subsets have the potential to induce protective benefits against skin Ag and tumor development.

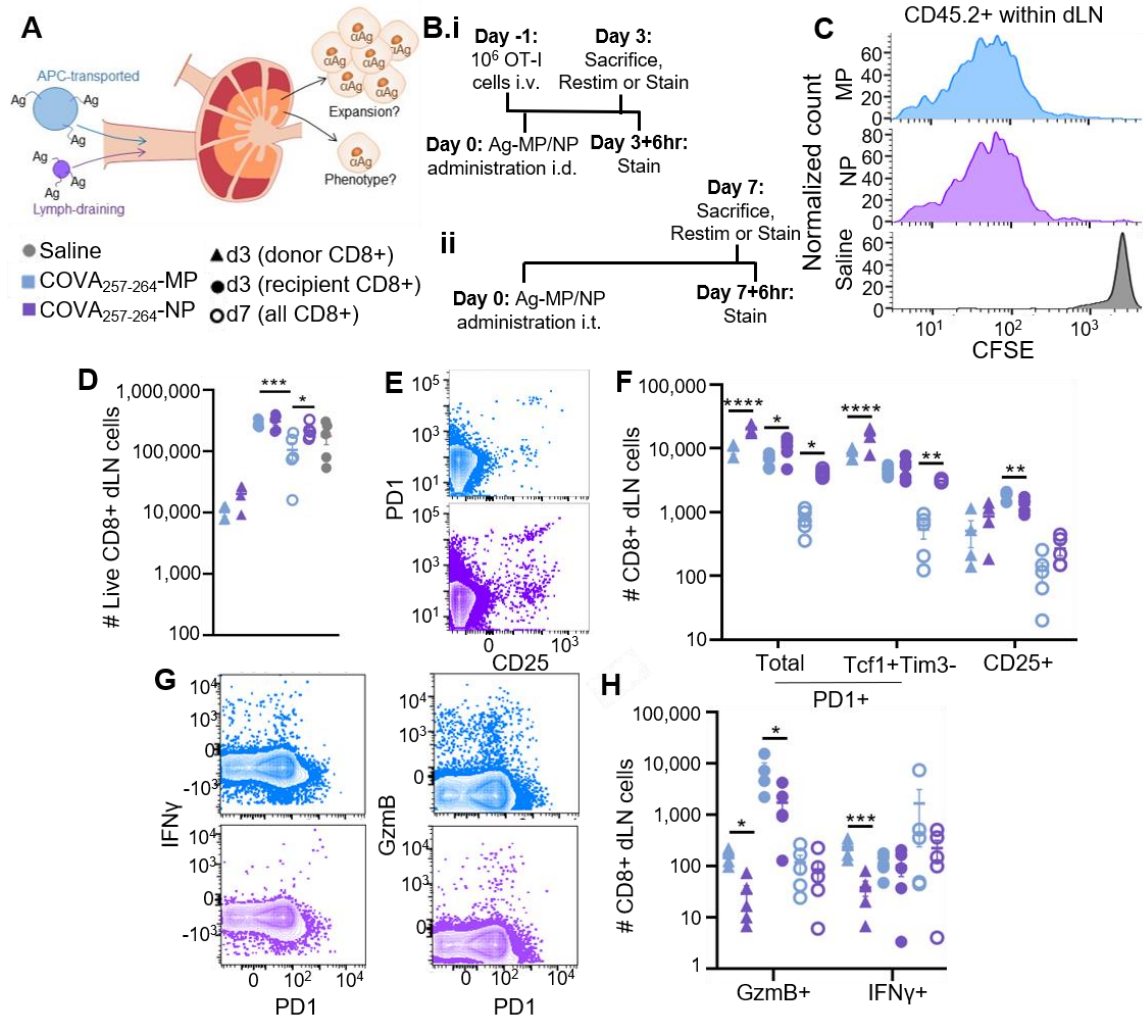


Figure 3.6: Extent of expansion and quality of Ag-specific CD8⁺ T cell pool in response to Ag is dependent on the mechanism of lymphatic transport to the dLN. Schematic outlining the approach (a) and experimental design (b) for synthetic Ag system to assess the influence of lymphatic transport mechanism on CD8⁺ T cell responses elicited in dLNs. (c) Representative CFSE plots of viable Ag-specific, CD45.2⁺CD8⁺ dLN donor cells 72 h after treatment with synthetic Ag systems. (d) Number of live CD8⁺ donor and recipient cells in dLNs 3 or 7 d after treatment with synthetic Ag systems. Saline includes pooled data from T cells collected both 3 and 7 d after treatment with synthetic Ag systems. (e) Representative flow cytometry plot of PD1 and CD25 expression by dLN CD8⁺ T cells 7 d after treatment with synthetic Ag systems. (f) Number of marker-expressing cells in the dLN 3 or 7 d after

treatment with synthetic Ag systems. (g) Representative flow cytometry plot of IFN- γ , GzmB, and PD1 expression by CD8⁺ T cells in the dLN 3 d after treatment with synthetic Ag systems. (h) Number of cytokine-producing Ag-specific donor cells 3 or 7 d after treatment with synthetic Ag systems. * indicates significance by one-way ANOVA (* indicates $p < 0.05$, ** indicates $p < 0.01$, * indicates $p < 0.005$, **** indicates $p < 0.00001$); n=5-7 mice.**

3.3.6 Therapeutically Functional Antitumor T Cell Responses in the TME Result from Ag Priming of CD8⁺ T Cells within TdLNs

The ramifications of altered APC Ag access, maturation, and Ag presentation within TdLNs as a result of melanoma lymphatic drainage with respect to elicited functional T cell responses were assessed using the synthetic Ag system. Specifically, Ag-MPs or -NPs were administered intratumorally on d 0 into animals bearing parental (non-OVA-expressing) B16F10 melanomas 7 d after implantation. End point analyses of both donor CD45.2⁺ OT-I CD8⁺ T cells adoptively transferred 1 d before Ag challenge and recipient CD8⁺ T cells 3 d after administration (i) or endogenous CD8⁺ T cells 3 d after administration (ii) were performed. Similar to responses observed in tumor-free animals (Figure 3.6), proliferation of donor Ag-specific T cells within TdLNs 3 d after treatment was roughly equivalent regardless of the mechanism of lymphatic transport of Ag and irrespective of the presence of the d 7 B16F10 melanoma (Figure 3.7a). In contrast to responses seen in naïve animals (Figure 3.6c), CD8⁺ T cell numbers within TdLNs in response to MP- and NP-tethered Ag were also roughly equivalent (Figure 3.7b). However, when evaluating the quality of responses elicited, subtle differences were noted. Ag-MP treatment resulted in an increase in PD1⁺ and PD1⁺Tcf1⁺Tim3⁻ CD8⁺ T cell numbers within TdLNs 7 d but not 3 d after administration (Figure 3.7c). However, with Ag-NP treatment, the levels of both PD1⁺ and PD1⁺Tcf1⁺Tim3⁻ Ag-specific donor and PD1⁺ recipient CD8⁺

T cells were decreased within TdLNs relative to LNs draining tumor-free skin 3 d after administration (Figure 3.7c). CD25⁺ and CD39⁺ cell numbers showed less consistent trends across time in Ag-NP-treated tumor-bearing animals, with a decrease in CD25⁺ cells 3 d and endogenous CD39⁺ cells 7 d after treatment. However, Ag-MP treatment resulted in diminished levels of CD25⁺ cells 3 d after treatment but increases in both CD25⁺ and CD39⁺ cells 7 d after treatment. With respect to cytotoxic CD8⁺ T cell immunity, levels of cytokine-producing cells (both donor and endogenous) within TdLNs elicited by Ag-MP treatment, on the other hand, were largely unchanged, save a reduction in IL-2-expressing cells 3 d after treatment. Ag-NP treatment resulted in diminished IFN- γ - and IL-2-expressing CD8⁺ T cells within TdLNs 7 d after administration. However, numbers of GzmB-expressing CD8⁺ T cells, which are degranulated and can directly kill tumor cells, elicited by Ag-MP, but not Ag-NP, treatment were diminished within TdLNs at both 3 and 7 d after administration compared to LNs draining tumor-free skin (Figure 3.7d). This decrease within the TdLN coincided with a substantial increase in GzmB⁺ CD8⁺ T cells in the TME 7 d after treatment compared to saline-treated tumors (Figure 3.7e). In contrast, although stem-like (PD1⁺Tcf1⁺Tim3⁻) CD8⁺ T cells were expanded within TdLNs by both synthetic Ag systems, their numbers within the TME remained relatively unchanged irrespective of treatment type (Figure 3.7f). However, numbers of PD1⁺Tim3⁺Tcf1⁻ cells, which are derived from stem-like PD1⁺Tcf1⁺Tim3⁻ cells as they transition to an effector phenotype [40, 41], were substantially increased within the TME d 7 after administration of either Ag-MP or -NP treatment (Figure 3.7f). Moreover, ~20 to 30% of tumor-infiltrating CD8⁺ donor cells were found to be viable in response to either Ag-MP or -NP treatment (Figure 3.7f), in sharp contrast to tumor Ag-specific CD8⁺ T cells infiltrating

tumors that are largely (>90%) nonviable (Figure 3.5e-f) [151]. Overall, Ag-NP/MP treatment resulted in higher total CD8⁺ T cell infiltration into tumors (Figure 3.7g), a characteristic that has been independently associated with increased survival in patients with melanoma [28]. These results suggest that priming of CD8⁺ T cell immunity within TdLNs results in improved quality and quantity of TME-infiltrating CD8⁺ T cells.

To assess the impacts of enhanced tumor infiltration of effector-like PD1⁺Tim3⁺Tcf1⁻ and effector GzmB⁺ CD8⁺ T cells on therapeutic responses, two classes of tumor immunotherapy were evaluated. First, we evaluated the effects of mAb-mediated blockade of PD1 signaling, which results in a proliferative burst by stem-like PD1⁺Tcf1⁺Tim3⁻ CD8⁺ T cells [40]. We recently reported [14] the improved immunotherapeutic effects of this therapy when directed to TdLNs using locoregional administration, e.g., administration in the skin ipsilateral to the tumor, resulting in co-drainage by mAb to the TdLN, compared to administration using either a conventional systemic route of mAb administration (i.p.). When the effects of TdLN-directed versus systemic ICB using anti-PD1 mAb on tumor Ag-specific donor OT-I (CD45.2⁺) CD8⁺ T cells 3 d after transfer into CD45.1 mice bearing B16F10-OVA melanomas were assessed, the former was associated with higher densities of both circulating CXCR5⁺Tim3⁻ [stem-like [40]; Figure 3.7j] and Ki67⁺ (proliferating; Figure 3.7k) CD8⁺ T cells. With respect to proliferative generation traced via analyses of CFSE dilution, TdLN-directed ICB (ipsilateral) also resulted in higher numbers of circulating donor cells in later (G4 to 8) generations compared to saline or i.p. ICB-treated animals (Figure 3.7l). In contrast, earlier generations of donor cells were generally found within TdLNs compared to tumors irrespective of treatment (Figure 3.7l). Together with observations of increased tumor

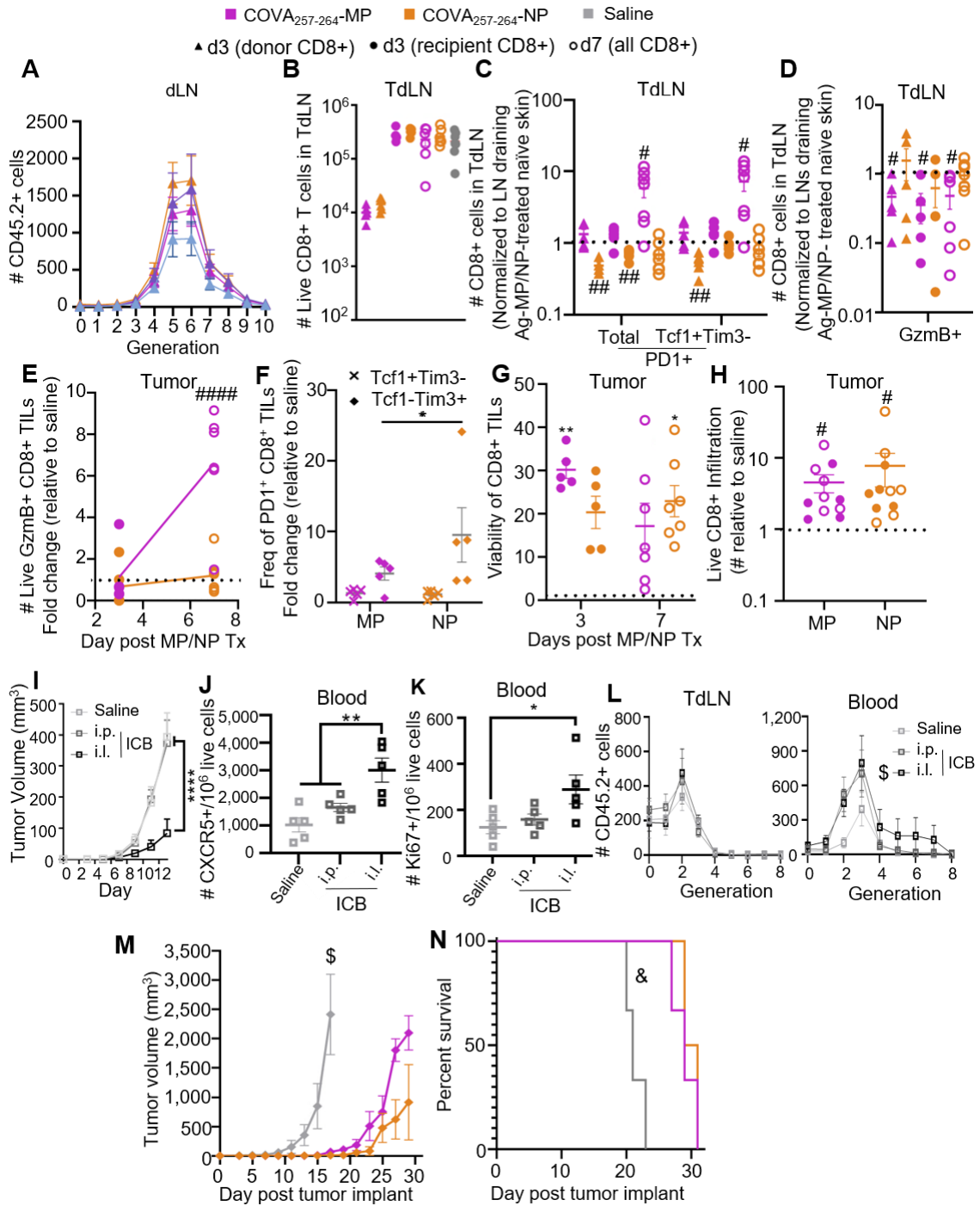


Figure 3.7: Expansion of CD8⁺ T cells in TdLNs in response to administration of synthetic Ag systems affects tumor-infiltrating T cells and has antitumor functions. (a) Quantification of Ag-specific donor cell proliferation within dLN 3 d after treatment of naïve and melanoma-bearing animals with Ag-MP or –NP. (b) Number of viable CD8⁺ T cells in TdLN 3 and 7 d after Ag-MP or –NP treatment. Saline includes T cells collected both 3 and 7 d after treatment with synthetic Ag systems,

with no difference between analysis day. (c) Responding phenotype of Ag-specific donor cells 72 h after Ag-MP or –NP treatment and endogenous cells 3 and 7 d after Ag-MP or –NP treatment normalized to naïve condition. (d) Quantification of GzmB producing Ag-specific donor cells as in c. (e) Number of TME-localized GzmB⁺ CD8⁺ cells in Ag-MP or –NP treated B16F10 tumors of CD45.1 mice relative to saline-treated tumors. (f) Frequency of Tcf1 and Tim3 expressing PD1⁺ Ag-specific donor (CD45.2⁺) CD8⁺ cells in Ag-MP or –NP treated B16F10 tumors of CD45.1 mice relative to saline-treated tumors. (g) Viability (as %) of CD8⁺ T cells within the TME. Dashed line indicates viability of CD8⁺ T cells in B16F10-OVA tumors, statistics relative to dashed line. (h) Number of live CD8⁺ T cells infiltrating Ag-MP/NP treated tumors relative to saline-treated tumors. (i) Tumor growth of B16F10 tumor after α PD1 treatment in the ipsilateral forearm skin or i.p. or saline treatment d5, 7, 9 post tumor implantation. Number of tumor Ag-specific CXCR5⁺Tim3⁻CD45.2⁺ (j) and Ki67⁺CD45.2⁺ (k) donor cells in blood of tumor-bearing CD45.1 mice in response to 150 μ g α PD1 mAb administered in the ipsilateral forelimb skin or i.p. d 5, 7, 9 post tumor implantation. (l) Proliferative generations of tumor Ag-specific donor CD8⁺ T cells in the TdLN (left), and blood (right). B16F10-OVA tumor growth (m) and animal survival (n) after i.t. treatment in contralateral B16F10 tumor resected 3 d post treatment with saline of Ag-MP or –NP. # indicates significance against normalized value of 1.0 (representing no change relative to control) by one-sample t-test; * indicates significance by one-way ANOVA with Tukey's comparison; \$ indicates significance relative to all other groups by repeat measures (RM) ANOVA with Tukey's comparison; & indicates significance relative to all other groups by log-rank test; n=3-10 animals; h, m-n are representative of two independent experiments.

infiltration by PD1⁺Tim3⁺Tcf1⁻ CD8⁺ T cells resulting from Ag-MP/NP treatment (Figure 3.7f), this is consistent with stem-like PD1⁺Tcf1⁺Tim3⁻ cells expanded within TdLNs being mobilized and accumulating in their differentiated state as effector-like cells within the TME. This is also consistent with reports of T cells disseminating from the dLN subsequently losing *Tcf1* expression [152]. Augmented immunotherapeutic effects from TdLN-directed ICB thus appear to be associated with mobilization of stem-like and responding CD8⁺ T cells from TdLNs into the circulation to result in TME infiltration and antitumor effects.

Second, the potential for the synthetic Ag-MP/NP system that expands the effector CD8⁺ T cell pool to protect against tumor growth was evaluated. To assess the effectiveness

of the different subpopulations of T cells primed by each Ag system at controlling tumor growth, Ag covalently tethered to either MPs or NPs was administered intratumorally into a d 7 B16F10 (non-OVA expressing) melanoma. On d 3 after synthetic Ag administration, the primary tumor was excised. In so doing, animal survival was determined not by the treated primary tumor but instead by growth of a secondary, OVA-expressing B16F10 tumor that was implanted in the contralateral dorsal skin. Irrespective of conjugation to either MPs or NPs, treatment with the synthetic Ag resulted in retardation of growth of the contralateral B16F10-OVA melanoma (Figure 3.7m), effects that prolonged animal survival (Figure 3.7n) in two independent experiments. In these studies, the excision of the primary tumor (receiving the Ag-MP/NP injection) left only primed cells within TdLNs in addition to those that had already disseminated from the treated TME. As cells expanded within the TME exhibit low viability (Figure 3.5e-f), therapeutic effects can, thus, be interpreted to be dLN-mediated. This implicates tumor lymphatic transport of passively drained or cell-trafficked Ag as inducing CD8⁺ T cell immunity that has antitumor functionality. Of note, both the MP and NP treatment resulted in decreased tumor growth and enhanced survival benefits, indicating that expansion of either stem-like or effector cells within the dLN can enhance antitumor responses to a similar degree. Together, these data support the concept that the TdLN represents a niche for expansion of therapeutically relevant CD8⁺ T cell subsets implicated in the efficacy of tumor immunotherapy.

3.4 Discussion

Long overlooked for other than their prognostic value, LNs represent increasingly attractive therapeutic targets in cancer therapy applications [13, 14, 93, 147]. LNs function as “transit hubs” of the adaptive immune system that facilitate co-mingling of APCs and

lymphocytes within microenvironments conducive to generation of adaptive immune responses. We show here two engineered material systems inspired by the way Ag is transported to LNs via the lymphatic vasculature to delineate in a quantitative fashion how lymphatic transport mechanism influences LN-localized signaling to CD8⁺ T cells and the impacts of malignancy on these processes. By applying these biomaterials tools to the integrated analysis of lymphatic physiology effects on CD8⁺ T cell immunity relevant to tumor immunotherapy, this work expands upon the currently limited understanding of how Ag transport and interactions between the tumor and LN-resident cells, as mediated by the lymphatic system, occur in melanoma. Our findings elaborate the potential for nanoengineering approaches to harness various lymphatic transport mechanisms to optimize melanoma immunotherapy in eliciting and mobilizing various classes of antitumor CD8⁺ T cell immunity.

A fluorescent tracer panel designed to quantify lymphatic transport as mediated by migrating APCs versus lymph drainage revealed that alterations in cellular uptake and LN remodeling compensate to sustain access of tumor-derived solutes by LN-resident cells. Specifically, skin-resident DCs become more migratory, reaching the dLN in higher numbers. This is in line with reports of enhanced migratory and decreased phagocytic capacity of activated DCs [120, 153]. Others have shown that CD11b⁺ dDCs that express major histocompatibility complex (MHC)-II access the melanoma dLN at similar rates to the naïve skin dLN [154]; however, by examining all dDCs and LCs, we demonstrate enhanced mobility of the skin DC population as a whole. Evaluating this entire cell population facilitates examination of CD8⁺ T cell responses in this context, instead of CD4⁺ T cell responses elicited by MHC-II⁺ DCs. In addition, lymph-derived, nanoscale solutes

are also accessible to cells normally restricted from sampling lymph by the SCS and other structural barriers within the LN. The melanoma dLN has been shown to remodel [105], enhancing intra-LN access to tracers of this size range. Thus, these findings are in line with current understandings of melanoma-induced remodeling locally and within the TdLN. Despite its simplicity, limitations in the tracer system used herein include the comparisons between dextrans and spheres, which differ in physical and chemical properties [66].

A synthetic Ag system was used to elaborate the influence of disease on Ag presentation by LN-localized cells resulting from Ag delivered to dLNs via different lymphatic transport mechanisms. Despite sustained access by LN-resident cells to lymph-draining Ag, the extent of Ag presentation by dLN-resident cells was unchanged in the melanoma context, suggesting that Ag presentation is locally suppressed. In contrast, presentation of cell-transported Ag, which is taken up and whose presentation occurs first within the periphery or during intralymphatic transit [100, 155], was increased within TdLNs. We hypothesize that differences in tumor effects between these mechanisms are due to the phenotypes of DCs differentially accessed by each lymphatic transport mechanism. Passively draining Ag was presented primarily by pDCs and cDCs, which exhibit a tolerogenic phenotype, while actively transported Ag was presented by dDCs and LCs, which are more activated in the tumor context. These results are consistent with previous reports demonstrating that both pDCs and cDCs express immunosuppressive molecules within the melanoma dLN [156, 157], while tumor-resident DCs are mature [154]. Furthermore, mature DCs have decreased phagocytic capacity but maintain Ag presentation functions [120, 153]. The induction of tolerogenic phenotypes in LN-resident DCs by the tumor results in levels of presentation by lymph-draining Ag that are relatively

unchanged compared to naïve animals, while activation of skin-resident DCs by the tumor enhances Ag presentation within the TdLN. We note that these studies omitted the analysis of stromal populations, despite their robust Ag presentation and immunomodulatory properties, particularly in the context of melanoma [158].

The combined effects of lymphatic transport mechanism and microenvironment on resulting responses by CD8⁺ T cells were interrogated using the synthetic Ag system. Lymph-draining Ag was found to increase the expansion of the stem-like CD8⁺ T cell reservoir within the dLN over cell-trafficked Ag, an effect largely unaltered by the presence of melanoma. These cells, which provide the proliferative burst in response to anti-PD1 ICB therapy [40, 41] and whose presence in patients is associated with improved survival [38, 41], can recirculate and differentiate, reaching the TME at higher numbers to improve immunotherapeutic effects. Conversely, CD8⁺ T cells with effector functions associated with improved survival in melanomas [28, 37] were more robustly induced within dLNs by cell-trafficked Ag and were mobilized to the TME in the tumor context. Each CD8⁺ T cell subtype that expanded locally within the TdLN in response to lymphatic-transport Ag was furthermore functional and associated with reductions in tumor growth and enhanced survival of melanoma-bearing animals in response to ICB or *in situ* vaccine immunotherapy. We note that this investigation was limited to the relatively lymphatic-rich B16F10 melanoma model as human melanomas tend to be lymphatic infiltrated [122, 123]. However, recent seminal work has demonstrated the correlation between tumor lymphangiogenesis and tumor immune microenvironment and responsiveness to immunotherapy [97, 98], effects attributed directly to the TME. Future studies elaborating immunological responses within TdLNs as they relate to the extent of lymphatic infiltration

within the melanoma, in combination with the work presented here, have the potential to benefit the treatment of disease that is resistant to current immunotherapy regimens through LN-directed immunomodulation. Examples include tumors that are poorly infiltrated [159], lack niches that support stem-like CD8⁺ T cell survival and functions [160], and are stroma dense and into which therapeutic delivery is largely restricted [161].

The finding that different subsets of T cells with antitumor functions expand within LNs as a result of Ag transport mechanism has the potential to inform improved immunotherapeutic management of melanoma, particularly the examples described above. ICB therapies have been most effective in patients with expression of immune checkpoints and higher T cell infiltration [162]. We show here that lymph-draining vaccines have the potential to further enhance the application of these therapies by robustly expanding the pool of CD8⁺ T cells that provide the proliferative burst of tumor Ag-specific CD8⁺ T cells in response to ICB therapy. Immunotherapies have also been found to be more effective in patients with immunologically “hot” tumors that exhibit higher immune infiltration [163]. MP-based or depot vaccines that locally recruit and activate APCs within peripheral tissues before T cell expansion within dLNs represent a potential strategy to make tumors more hot by increasing infiltration of functional, effector T cells into the TME, which has been independently associated with survival [28, 37]. With the advent of bioengineering approaches in cancer immunotherapy and the emerging appreciation of LNs as druggable, therapeutically relevant tissues, lymphatic-directed drug delivery innovations therefore represent novel approaches to improve translational management of melanoma.

**CHAPTER 4. TUMOR-DRAINING LYMPH NODES ARE
SURVIVAL NICHEs THAT SUPPORT T CELL PRIMING
AGAINST LYMPHATIC TRANSPORTED TUMOR ANTIGEN
AND EFFECTS OF IMMUNE CHECKPOINT BLOCKADE IN
TNBC [164]**

TNBC is a significant clinical problem to which immunotherapeutic strategies have been applied with limited success. Using the syngeneic E0771 TNBC mouse model, this work explores the potential for antitumor CD8⁺ T cell immunity to be primed extratumorally in lymphoid tissues and therapeutically leveraged. CD8⁺ T cell viability and responses within the TME were found to be severely impaired, effects coincident with local immunosuppression that is recapitulated in lymphoid tissues in late stage disease. Prior to onset of a locally suppressed immune microenvironment, however, CD8⁺ T cell priming within LNs that depended on tumor lymphatic drainage remained intact. These results demonstrate TdLNs to be lymphoid tissue niches that support the survival and antigenic priming of CD8⁺ T lymphocytes against lymph-draining Ag. The therapeutic effects of and CD8⁺ T cell response to ICB were furthermore improved when directed to LNs within the tumor-draining lymphatic basin. Therefore, TdLNs represent a unique potential tumor immunity reservoir in TNBC for which strategies may be developed to improve the effects of ICB immunotherapy.

4.1 Introduction

Breast cancer is the most common cancer among women worldwide [2, 3] making it a significant public health threat. TNBC is the most aggressive breast cancer type with the poorest outcomes due to its high propensity to metastasize and limited available treatment modalities [27]. As such, there is a clear need for improved therapies to treat TNBC. Immunotherapy has emerged as one of the most promising strategies to combat TNBC due to its potential to treat local as well as disseminated disease and the fact that TNBC is a relatively immunogenic breast cancer type. ICB is an immunotherapy class that can re-energize anergic and exhausted T cells by inhibiting signaling that dampens the cytotoxic functions of T lymphocytes [52]. Atezolizumab and pembrolizumab, mAbs against PDL1 and PD1, respectively, are the only currently approved ICB strategies for a subset of TNBC patients, in combination with paclitaxel [29, 56]. However, rates of response are severely limited overall (~16%) [29]. Improving immunotherapy therefore represents a clinical hurdle to diminishing TNBC mortality.

Although its effects are elicited within the TME, antitumor immunity in TNBC can occur extratumorally [165–167]. This suggests the potential for approaches leveraging such extratumoral microenvironments to improve ICB. To this end, secondary lymphoid tissues, including spleens and LNs, are organs that house a substantial fraction of the cells of the adaptive immune system and are specialized to facilitate Ag presentation and lymphocyte priming, activation, and expansion [12, 30]. Lymphoid tissues of TNBC patients have been shown to house tumor-specific lymphocytes [165], although whether these cells locally expand in response to Ag or infiltrate after antigenic priming elsewhere remains ill-defined. Although spleens access Ag in the circulation, sampling of Ag within

LN is facilitated by the transport functions of the lymphatic system. Lymph, which contains solute and small, nanoscale particulate (10-50 nm)-laden interstitial fluid, is formed in the periphery and is drained through lymphatic vessels into downstream LNs where it is accessed by resident APCs [61, 62, 64, 65, 168]. APCs within peripheral tissues also facilitate Ag access by phagocytosing Ag and migrating to these dLN where they can interact with lymphocytes [78–81]. Whether splenic access to tumor-derived factors in the circulation and lymphatic transport from mammary tissues to LNs are influenced by malignancy to regulate the lymphoid tissue immune microenvironment, however, is poorly understood. Moreover, lymphoid tissues, like the TNBC TME, have been reported to be immunosuppressed: Tregs and MDSC are increased in the TME and premetastatic TdLN environments of TNBC patients [33–36, 103]; and DCs and effector T cells tend to be dysfunctional in the human TNBC TME [32]. However, increased quantity and quality of CD8⁺ T cell infiltration into the tumor increases survival [42–44], and enhanced CD8⁺ T cell-DC interactions with the TdLN are associated with enhanced survival in TNBC patients [169]. Likewise, TdLN-resident macrophages have been shown to enhance antitumor responses in TNBC [167]. The potential for lymphoid tissues to not only access tumor Ag but facilitate priming of tumor-specific immunity that has functional anti-tumor effects thus remains poorly defined.

Herein, the potential for lymphoid tissues to support extratumoral lymphocyte priming was evaluated in the syngeneic mouse model of E0771 TNBC. The results suggest that despite TNBC disease that manifests in TME-localized immune suppression and disrupts tumor vascular functions that regulate Ag access to APCs, LNs within the tumor lymphatic drainage basin, e.g., TdLNs, are lymphoid tissue niches that support the survival

and antigenic priming of CD8⁺ T lymphocytes. TdLNs therefore represent a unique potential tumor immunity reservoir that when therapeutically targeted can improve the effects of ICB immunotherapy.

4.2 Materials and methods

4.2.1 Cell Culture

E0771 and E0771-OVA (kind gift of Dr. Zachary Harman, Duke University) mouse mammary carcinoma cells were cultured in Dulbecco's Modified Eagle Medium with 10% heat-inactivated fetal bovine serum and 1% penicillin/streptomycin/amphotericin B (Life Technologies), the latter with the addition of 1 µg/mL puromycin (Gibco Laboratories).

4.2.2 Animal Tumor Models

C57Bl/6 (either CD45.2 or CD45.1) mice were purchased at 6 wks of age from the Jackson Laboratory. All protocols were approved by the Institutional Care and Use Committee. The hair on the skin over the fourth (inguinal) mammary fatpad (MFP) was removed using depilatory cream (Church & Dwight, Ewing Township, NJ) and cleaned using warm water and ethanol wipes. For tumor-bearing cohorts, 0.5×10^6 E0771 or E0771-OVA cells were injected into the fourth (inguinal) MFP of 6-8 wk old mice on d 0. Tumor dimensions were measured with calipers in three dimensions and reported as ellipsoidal volume.

4.2.3 Flow Cytometry Analysis

LNs were incubated in 1 mg/mL Collagenase D (Sigma-Aldrich) in D-PBS with calcium and magnesium for 75 min at 37°C, passed through a 70 µm cell strainer (Greiner Bio-One), washed, and resuspended in a 96-well U-bottom plate (VWR International, Inc.) for staining. Spleen capsules were disrupted using 18G needles and the cell suspension was passed through a 70 µm cell strainer, pelleted by centrifuging at 350G for 5 min, and then incubated with red blood cell lysis buffer (Sigma Aldrich) for 7 min at room temperature, diluted with D-PBS, washed, and resuspended in 1mL D-PBS. 50 µL of the resulting solution was plated for staining. Tumors and MFP tissues were mechanically disrupted using 18G needles, then incubated in 1 mg/mL collagenase D (Sigma Aldrich) in D-PBS with calcium and magnesium for 4 h at 37°C, passed through a 70 µm cell strainer (Greiner Bio-One), washed with D-PBS, pelleted, and plated. All antibodies for flow cytometry were from Biolegend, Inc., unless otherwise specified. Cells were blocked with anti-mouse CD16/CD32 (clone 2.4G2; Tonbo Biosciences) for 5 min on ice, then washed. Cells were stained with fixable viability dye Zombie Aqua (1:100) for 30 min at room temperature, then washed with D-PBS with calcium and magnesium. Antibodies were prepared in flow cytometry buffer (D-PBS with calcium and magnesium + 1% bovine serum albumin (Sigma Aldrich)) at the following dilutions based upon preliminary titrations: PerCP-Cy5.5 anti-mouse CD45.2 (1.25:100) or Brilliant Violet 711 anti-mouse CD45.2 (1.25:100), PerCP anti-mouse CD3 (2.5:100) or Brilliant Violet 711 anti-mouse CD3 (1.25:100), APC-Cy7 anti-mouse CD8 (2.5:100), Alexa Fluor 700 anti-mouse CD25 (1:100), Brilliant Violet 786 anti-mouse PD-1 (1.25:100), PE-Cy7 anti-mouse CD39 (5:100), Brilliant Violet 605 anti-mouse Tim3 (1.25:100), and Brilliant Violet 421 anti-mouse CD44 (5:100). Cells were incubated with antibody solution for 30 min on ice in the dark, then washed with flow

cytometry buffer. Cells were fixed and permeabilized using FoxP3/Transcription Factor Staining Buffer Set (Thermo Fisher Scientific, Inc.) per manufacturer instructions. Tcf1 staining solution was prepared using PE anti-mouse Tcf1 (Beckton Dickinson) at a concentration of 1.25:100 in permeabilization buffer. Cells were resuspended in Tcf1 staining solution and incubated for 75 min on ice in dark, then washed with flow cytometry buffer. Cells were resuspended in flow cytometry buffer and kept at 4°C until analyzed with a customized BD LSRFortessa (BD Biosciences).

4.2.4 *CD8⁺ T Cell Isolation*

OT-I animals were purchased from Charles River Laboratories and bred in house. OT-I animals were sacrificed, and the spleens harvested and disrupted using 18G needles followed by washing with D-PBS. Cells were passed through a 70 µm cell strainer (Greiner Bio-One), washed with D-PBS, and incubated with ACK Lysis Buffer (Lonza Group AG) for 60 s at room temperature, quenched with D-PBS, washed with D-PBS, and resuspended for counting. Cells were resuspended at 10⁸ cells/mL buffer (2% bovine serum albumin in D-PBS), blocked with Normal Rat Serum, and mixed with CD8⁺ T cell isolation antibody cocktail (StemCell Technologies), followed by streptavidin-coated magnetic beads (StemCell Technologies). Buffer was then added to the mixture, and placed in a magnet (StemCell Technologies), and the supernatant collected. Cells were then counted and resuspended in CFSE (Life Technologies), and then quenched with ice-cold RPMI medium (Life Technologies) containing at least 10% heat-inactivated fetal bovine serum (Life Technologies). Purity, viability, and CFSE loading were confirmed via flow cytometry on a customized LSRFortessa flow cytometer (Beckton Dickinson) before adoptive transfer.

4.2.5 *Adoptive Transfer*

Isolated CD8⁺ T cells were suspended in sterile saline at a concentration of 1×10^6 cells/200 μ L sterile saline. The hair over the neck of the mice was removed using depilatory cream, cleaned using warm water and ethanol wipes, and the suspended cells injected i.v. via the jugular vein.

4.2.6 *Micro-computed Tomographic Imaging (μ CT)*

Animals were perfused with saline at the heart followed by neutral buffered formalin (Thermo Fisher Scientific, Inc.) for 10 min, then with saline to rinse, and lastly MicroFil (Flow Tech Inc., Carver, MA) catalyzed at a viscosity appropriate for small vessels (5 mL lead-based contrast agent:2.5 mL diluent:0.25 mL curing agent). Afterwards, perfused mice were carefully stored at 4°C overnight to cure the contrast agent. The following day, MFP or tumor samples were harvested and stored in D-PBS. Microcomputed tomographic imaging (μ CT) was accomplished using a SCANCO Medical μ CT50 (Scanco USA, Inc., Wayne, PA). μ CT image slices were constrained using manual selection of the sample outline and processed with a Gaussian filter at a consistent global threshold via the Scanco Medical μ CT Evaluation Program before 3-dimensional reconstruction [170].

4.2.7 *Enzyme-linked Immunosorbence Assay (ELISA)*

The R&D Systems DuoSet ELISA kit (Minneapolis, MN) was used for ELISA assays. In brief, Nunc MaxiSorp high affinity plates (Thermo Fisher, Inc.) were incubated with capture antibody overnight at room temperature. The plate was washed with 0.05%

Tween 20 (Sigma Aldrich) in D-PBS (wash buffer), and then blocked with 1% bovine serum albumin in D-PBS (reagent diluent). Plates were washed, and 100 μ L sample diluted in reagent diluent was added to each well and incubated for 2 h at room temperature, then washed. The detection antibody was added to each well and incubated for 2 h at room temperature, then washed. Streptavidin-HRP was added to each well and allowed to incubate for 20 min at room temperature, followed by addition of substrate solution (R&D systems). 2 N sulfuric acid (VWR Chemicals BDH, Radnor, PA) was used to stop the reaction, and the absorbance read at 450 nm, 540 nm, and 570 nm on a BioTek Synergy H4 Hybrid Multimode Microplate Reader (Winooski, VT).

4.2.8 *Fluorescent Tracers*

500 nm red fluorescent (580/605 excitation/emission) carboxylate-modified microspheres were purchased from Thermo Fisher Scientific, Inc. 10 kDa (5 nm) Alexa Fluor 647 dextran was purchased from Thermo Scientific, Inc. 500 kDa (30 nm) amino-dextran (Thermo Fisher Scientific, Inc.) was covalently labeled by incubation with Alexa Fluor 700-*N* hydroxysuccinimide-ester dye (Thermo Fisher Scientific, Inc.) in 0.1 M NaHCO₃ at pH 8.4 for 4 h on a tube rocker. Alexa Fluor 700 dextran-dye conjugates were purified from unreacted free dye by Sepharose CL-6B gravity column chromatography after conjugation. Purified dextran-fluorophore conjugates were further confirmed free of unconjugated dye by a second Sepharose CL-6B column analysis [65]. All reagents were used and maintained under sterile conditions. Hydrodynamic sizes were confirmed pre-injection by dynamic light scattering using a Zetasizer Nano ZS (Malvern Instruments, Ltd.).

4.2.9 *Tracer Injections*

Fluorescent tracers suspended in saline were co-infused by syringe pump at a rate of ~ 300nL/s directly into the center of the tumors for tumor-bearing groups, or into the MFP for naïve groups, using a 31G needle while mice were under isoflurane anesthesia. 500 nm red fluorescent microspheres (19 pM), 30 nm Alexa Fluor 700 dextran (4.8 μM), and 10 nm Alexa Fluor 647 dextran (4.8 μM) were co-infused in 20 μL of saline total. Mice were euthanized via CO₂ asphyxiation at the prescribed times post-tracer injections for each experiment.

4.2.10 *Tracer Biodistribution Analyses*

At 4, 24, and 72 h post-tracer injection, mice were sacrificed and the tumor or MFP injection site, MFP-draining and contralateral non-draining inguinal and axillary LNs, spleen, lungs, liver, and kidneys were harvested and homogenized with a FastPrep-24 Automated Homogenizer. Whole tissue homogenate fluorescence was measured with a Synergy H4 BioTek plate reader (BioTek Instruments, Inc.), compensation was applied, and fluorescent tracer amounts, and concentrations were calculated from standard curves made by spiking individual tissue homogenates with tracer solution.

4.2.11 *LN Mapping*

Naïve or d 11 E0771-bearing C57/Bl6 mice were injected with 30 nm Alexa Fluor 647 dextran in the center of the tumor or the fourth (inguinal) MFP. Animals were sacrificed 24 h later, and LNs imaged on a LICOR Odyssey imaging system (Lincoln, NE).

4.2.12 *mAb Biodistribution*

Anti-PD1 mAb was mixed with either *N*-hydroxysuccinimide Ester-Alexa Fluor 610, Alexa Fluor 647, or Alexa Fluor 700 (Thermo Scientific Inc.) at 6 molar excess for 6 h. Fluorophore-labeled mAbs were cleaned of free dye using 7 kDa molecular weight cutoff Zeba spin columns, suspended in sterile saline, and mAb concentration determined by bicinchoninic acid assay (Thermo Scientific, Inc). Mice were intradermally (i.d.) injected in the forearm or flank or alternatively i.v. via the jugular vein with each of the three dye-labeled mAb, varying the site of each dye with each mouse, to ensure that labeling did not impact accumulation. 24 h after administration, the inguinal, axillary, and brachial LNs contralateral and ipsilateral to the i.d. injection site was excised, homogenized, and fluorescence analyzed as described above.

4.2.13 Therapeutic Evaluation

E0771 tumors were implanted on d 0 and measured using calipers every 48 h beginning at d 3. On d 11 of tumor growth, 100 μ g of anti-PD1 mAb (BioXCell) was administered in one of three injection routes: i.d. in the flank to target the inguinal (primary) TdLN, i.d. in the forearm to target the axillary (secondary) TdLN, or i.v. via the jugular vein. Isotype control mAb was administered i.d. in the flank in control animals. Animals were randomized and researchers blinded until sacrifice 5 d later, when lymphocytes were analyzed as described above.

4.2.14 Statistical Analysis

The data are represented as the mean accompanied by SEM, and statistics were calculated using GraphPad Prism 6, 7, and 8 software (GraphPad Software, Inc.). Statistical

significance was defined as $p < 0.05$, 0.01, 0.005, and 0.001, respectively, unless otherwise specified. AUC was calculated using the built-in Prism analysis tool.

4.3 Results

4.3.1 *E0771 Mammary Tumor Growth is Associated with TME-localized Immune Suppression and Vascular Remodelling*

Quantities of various TILs within E0771 tumors implanted in the MFP were evaluated at various stages of E0771 tumor progression (Figure 4.1a). Lymphocytes (CD45⁺), particularly T cells, infiltrated the TME at early stages, but their numbers within the TME progressively decreased during tumor growth (Figure 4.1b), in line with reports of initial immune responses in human patients deteriorating in late-stage disease [32]. At these later tumor stages, however, the number of PDL1-expressing CD45⁺ and CD45⁻ cells within the TME were strongly increased (Figure 4.1c), a trend recapitulating those seen in advanced human disease [139, 171]. Total DC (CD45⁺CD11c⁺B220⁻CD3⁻) levels within the TME trended towards a reduction in infiltration at all analyzed stages (Figure 4.1b), whereas Treg and MDSC levels increased significantly (~ tenfold higher) relative to the naïve tissue (Figure 4.1c).

Priming of tumor Ag-specific CD8⁺ T cells was evaluated in two stages of E0771 tumor growth in order to delineate the influence of disease stage on TME-localized antitumor immunity. As such, CFSE-labeled OT-I cells were adoptively transferred into CD45.1 animals bearing E0771-OVA tumors at either early (d7) or late (d21) stage. Tracing of proliferative response by monitoring CFSE dilution revealed tumor Ag-specific proliferation of tumor-infiltrating T cells to be attenuated in d21 as compared to d7 tumors

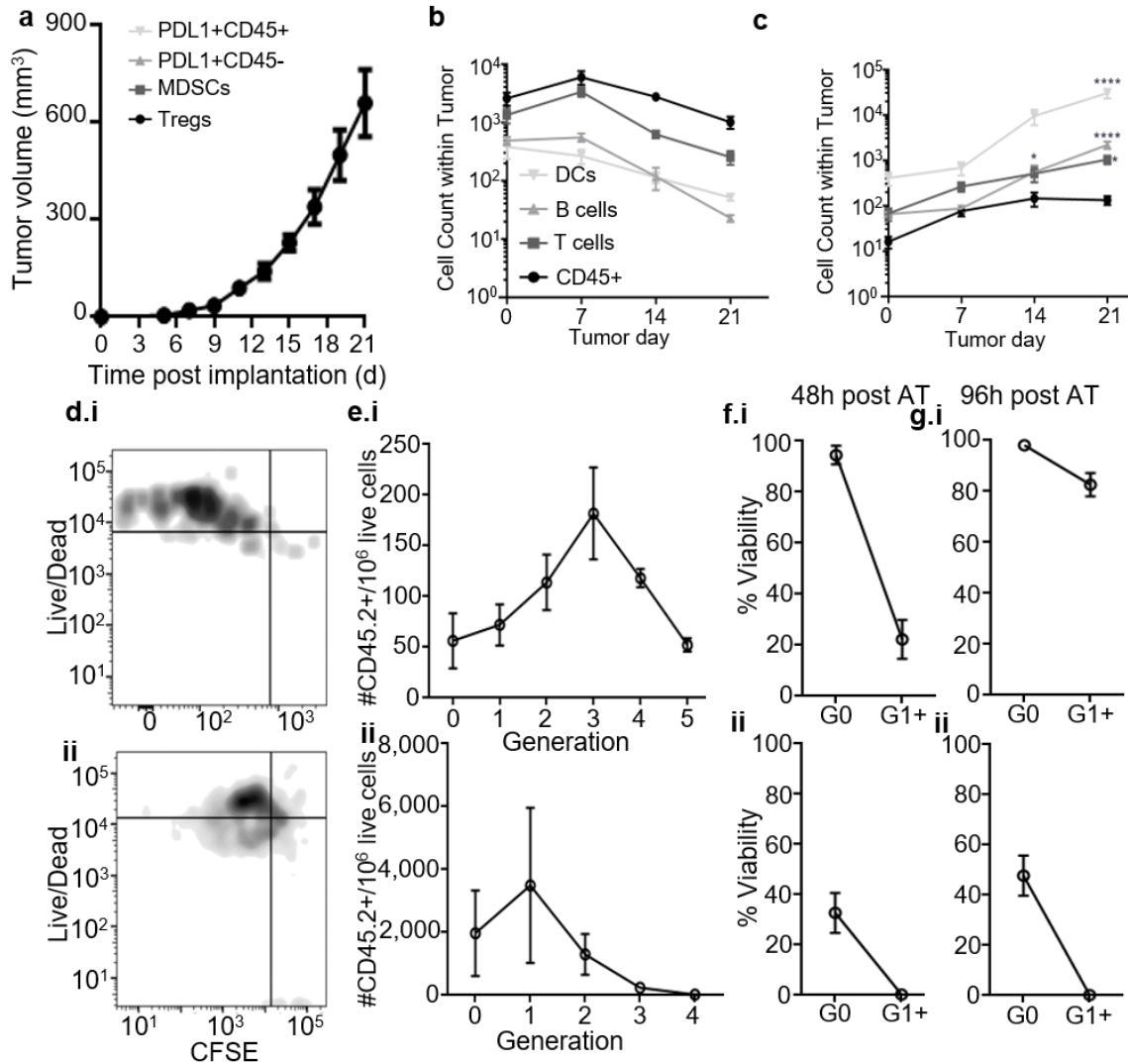


Figure 4.1: The tumor immune microenvironment remodels throughout E0771 disease progression and supports poor priming and viability of tumor Ag-specific CD8⁺ T cells. (a) E0771 tumor growth after implantation in the fourth MFP. Number of major (CD45⁺; DC, CD45⁺CD11c⁺B220⁻CD3⁻; B cells, CD45⁺B220⁺CD11c⁻CD3⁻; T cells, CD45⁺CD3⁺B220⁻) (b) and immunosuppressive (PDL1⁺CD45⁺; PDL1⁺CD45⁻; MDSC, CD45⁺CD11b⁺Gr1⁺; Tregs, CD45⁺CD3⁺B220⁻CD4⁺CD8⁻FoxP3⁺CD25⁺) (c) immune cell subsets in the TME. Representative CFSE versus Zombie live/dead staining (d) and quantification of number of live (e) and % viable (f-g) CD45.2⁺CD3⁺CD8⁺ donor OT-I T cells adoptively transferred within TME in each proliferating generation in d7 (i) or 21 (ii) CD45.1 E0771-OVA tumor-bearing mice 48 (e-f) or 96 (g) h post-transfer. * indicates significance by two-way ANOVA with Tukey's comparison (** indicates p<0.0001); n=5-6 mice.**

(Figure 4.1d, e), peaking at 3 generations (3 divisions) for d7 tumors and 1 generation (1 division) for d21 tumors 96 h post-adoptive transfer. Cell viability of all proliferating cells was also severely diminished at both tumor stages (Figure 4.1d, f). Cells that had not proliferated (G0) were more likely to remain viable (Figure 4.1f), indicating that activation or proliferation processes contributed to cell death in this tissue [172–174]. Unproliferated, tumor Ag-specific CD8⁺ T cells in d21 tumors also exhibited significantly reduced viability as compared to those infiltrating d7 tumors (Figure 4.1f), further demonstrating the suppressive environment in late stage tumors. Thus, tumor Ag-specific T cells in the TME show limited proliferation and low viability which progressively worsens with disease progression, coinciding with localized immune suppression (Figure 4.1c).

Remodeling of the tumor vasculature, another cancer hallmark [121, 175], in the E0771 model was also evaluated. μ CT analysis of perfused tumors at various times post-implantation revealed the vasculature to expand throughout tumor development and progression (Figure 4.2a), as indicated by measured vascular volume (Figure 4.2b), surface area (Figure 4.2c), and relative vascular volume compared to total tissue volume (Figure 4.2d), and most substantially so in late stage (d21) disease. These changes were accompanied by an increase in tumor levels of vaso endothelial growth factor (VEGF)-A (Figure 4.2e), an angiogenic growth factor both broadly implicated in neoangiogenesis and the regulation of vascular permeability [176–179] as well as highly expressed and associated with poor survival in TNBC [180–182]. The MFP concentration of VEGF-C, a lymphangiogenic growth factor that modulates lymphatic drainage functions [183, 184] and in melanoma has been implicated in regulating immune microenvironments [98], also decreased with the presence of a tumor, but did not progressively diminish with disease

progression (Figure 4.2f). The tumor vasculature of TNBC E0771 tumors thus concurrently remodels with the tumor immune microenvironment throughout disease progression.

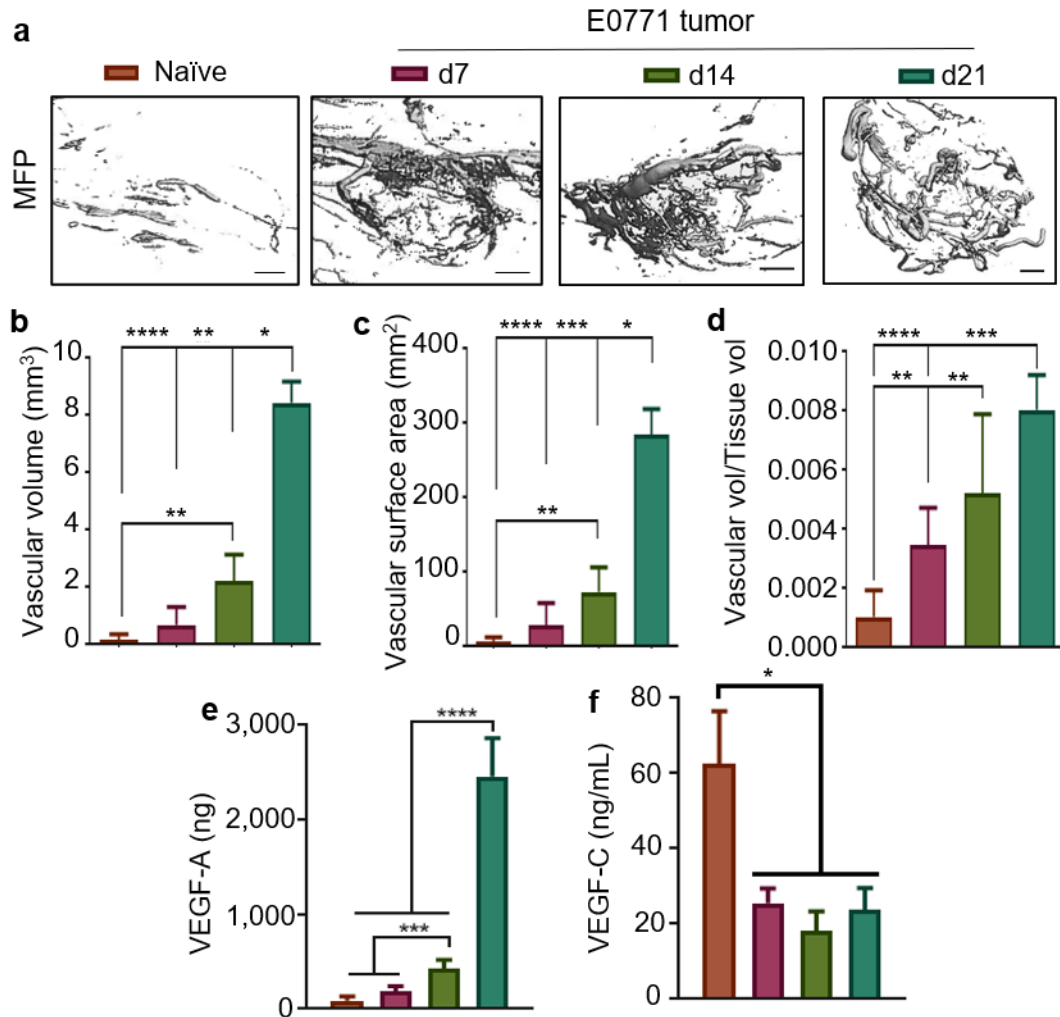


Figure 4.2: The tumor vasculature remodels throughout E0771 disease progression. Representative images (a) and quantification of mean vascular volume (b), surface area (c), and vessel diameter (d) of micro-computed tomography 3D reconstructions of the MFP or E0771 tumors. VEGF-A (e) and VEGF-C (f) levels in the naïve or tumor-bearing MFP throughout disease progression. * indicates significance by two-way ANOVA with Tukey's comparison (* indicates $p < 0.05$; ** indicates $p < 0.01$; *** indicates $p < 0.005$; **** indicates $p < 0.001$); $n = 5-6$ mice; scale bars indicate 1mm.

4.3.2 E0771 Disease Progression Effects on Lymphoid Tissue Immune Microenvironments and Molecular Dissemination from the TME

Given the potential for the complex molecular and cellular crosstalk between tumors and lymphoid tissues [61, 65, 94, 165, 167, 169, 185–187] to be influenced by tumor vascular remodeling (Figure 4.3) and reports of immune suppressive features in lymphoid tissues and in circulation of human patients [33–36, 103], the immune microenvironments of lymphoid tissues in the E0771 model were evaluated. Major cell subtypes in the TdLN or the NdLN as well as the spleen were found to remain largely unchanged throughout tumor progression (Figure 4.3a-c). In the TdLN, however, levels of cells exhibiting immune suppressive phenotypes, including MDSCs, Tregs, and PDL1 expressing CD45⁺ cells, remained relatively consistent across disease stage (Figure 4.3d). However, the abundance of PDL1⁺CD45⁻ cells, which manifest as a result from either LN metastasis or stromal cell expression of PDL1, was increased in later disease stages (Figure 4.3d). Overall, TdLNs were largely spared of tumor-induced immune suppression, particularly in early stage disease. Spleens of tumor-bearing animals, in contrast, demonstrated increased MDSC levels at early disease stage (d7), alterations that persist throughout disease progression (Figure 4.3e). Levels of non-hematopoietic cells expressing PDL1 were found to decline in d7 tumor-bearing animals but progressively increase in later stages (Figure 4.3e). Levels of CD45⁺ cells expressing PDL1 also increased in spleens of d21 tumor bearing animals. The spleen thus demonstrates immunosuppression, albeit at lower levels as compared to the tumor, beginning at the commencement of tumor development and progression. In the NdLN, levels of non-hematopoietic cells expressing PDL1 increase progressively, while other immunosuppressive cells, including MDSCs and

Tregs, trend towards decreasing below levels seen in the naïve MFP (Figure 4.3f). Of note, PDL1 expression in tumors exists in a regulatory loop controlled by CD8⁺ T cell production of IFN- γ [188]. As such, we measured IFN- γ in both the tumor and TdLN microenvironments, and found that the presence of a tumor decreased IFN- γ concentration within the MFP (Figure 4.3g), while IFN- γ concentration was maintained at similar levels within the TdLN throughout tumor development and progression (Figure 4.3h). Thus, we interpret these PDL1 expression levels as being tumor-intrinsic immunosuppression and not due to increased CD8⁺ T cell presence or activation in the TME.

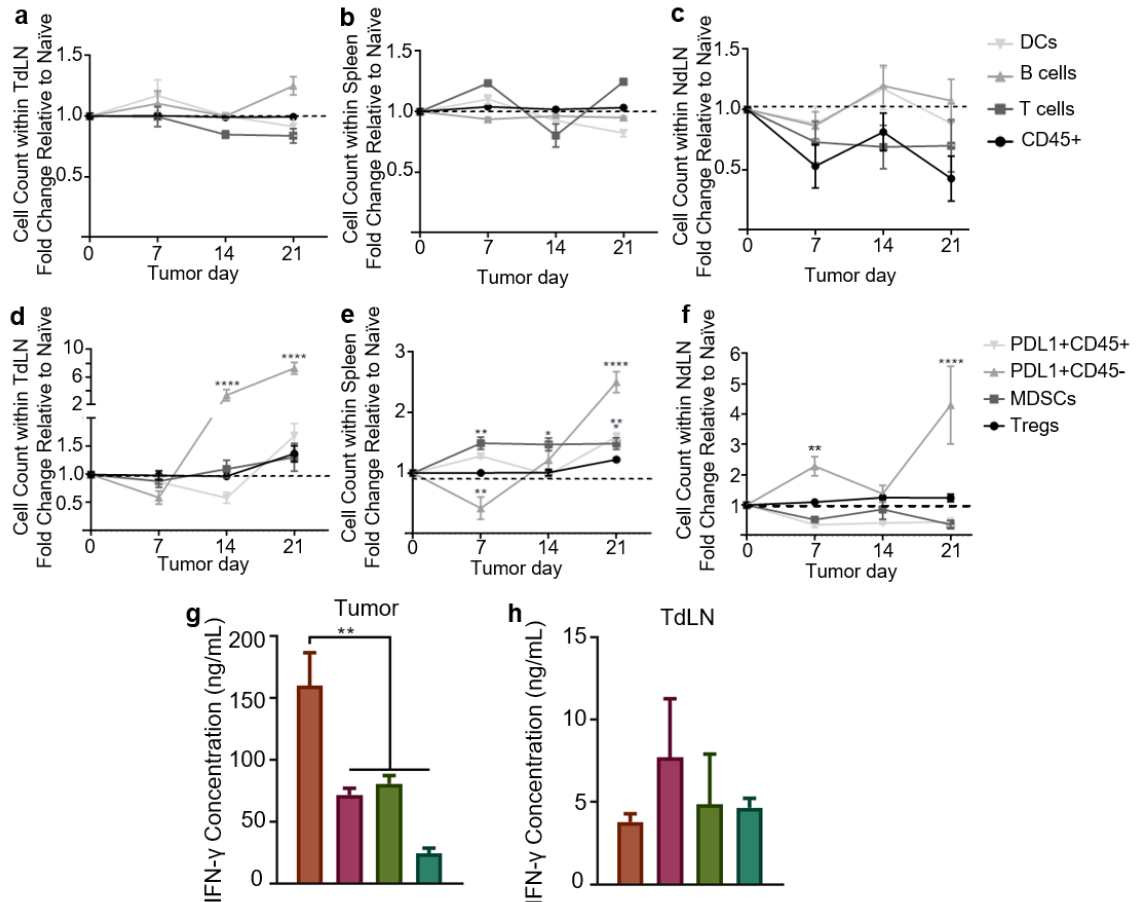


Figure 4.3: E0771 progression alters lymphoid tissue microenvironments. Fold change in the relative number of immune (CD45⁺, DC, B cells, T cells) (a-c) and immunosuppressive (PDL1⁺CD45⁺, PDL1⁺CD45⁻, MDSC, Tregs) (d-f) in the dLN (a,

d), spleen (d, e), and NdLN (c, f) relative to naïve tissue; IFN- γ concentration in the tumor (g) and dLN (h) microenvironments throughout disease progression. * indicates significance by two-way ANOVA with Tukey's comparison (1-f) or one-way ANOVA with Tukey's comparison (g-h) (indicates $p < 0.01$; **** indicates $p < 0.001$); n=5-6 mice.**

Remodeling of these lymphoid tissue microenvironments are suggestive of crosstalk with the E0771 TME that is disease stage dependent. To reveal if disease-associated tumor remodeling (Figure 4.1, Figure 4.2) impacts on dissemination from the TME into lymphoid tissues is associated with differences in immune suppression within lymphoid tissues that result from disease, we utilized a panel of differently sized tracers labeled with fluorophores with minimal spectral overlap to simultaneously probe various mechanisms of molecular dissemination from the MFP (Figure 4.4a) through fluorescence quantification of harvested, homogenized tissues. Macromolecules permeable to the blood vasculature (< 5 nm) rapidly diffuse through the tumor interstitium to be cleared into the blood whereas larger molecules are instead retained within the interstitium (Figure 4.4a). If smaller than the approximate tissue pore size (< 100 nm), macromolecules are subjected to interstitial flows to be drained to and taken up within lymphatic vasculature, in contrast to larger macromolecules and particulates (> 500 nm) that are instead locally retained and cleared in their intact form into lymphatic tissues only by the actions of phagocytic APCs (Figure 4.4a). A panel of tracers consisting of 5 versus 30 and 500 nm tracers were thus used to probe blood versus lymphatic clearance pathways, respectively, with the latter pair delineating passive lymphatic drainage versus cell-mediated trafficking (Figure 4.4a, b). This cocktail of tracers was infused into the naïve MFP as a single injection, and fluorescent content in relevant tissues assessed 4, 24, and 72 h later to confirm expected size- and time-dependent distribution profiles. 500, but not 5 or 30, nm tracers were found to be retained

at the injection tissue at high levels (Figure 4.4c). With respect to lymphatic uptake, 30 nm tracers accumulated within LN to the highest extents that peaked at 4 h post-injection (Figure 4.4d). 5 nm tracers show a similar pattern of dLN access, but at much lower levels,

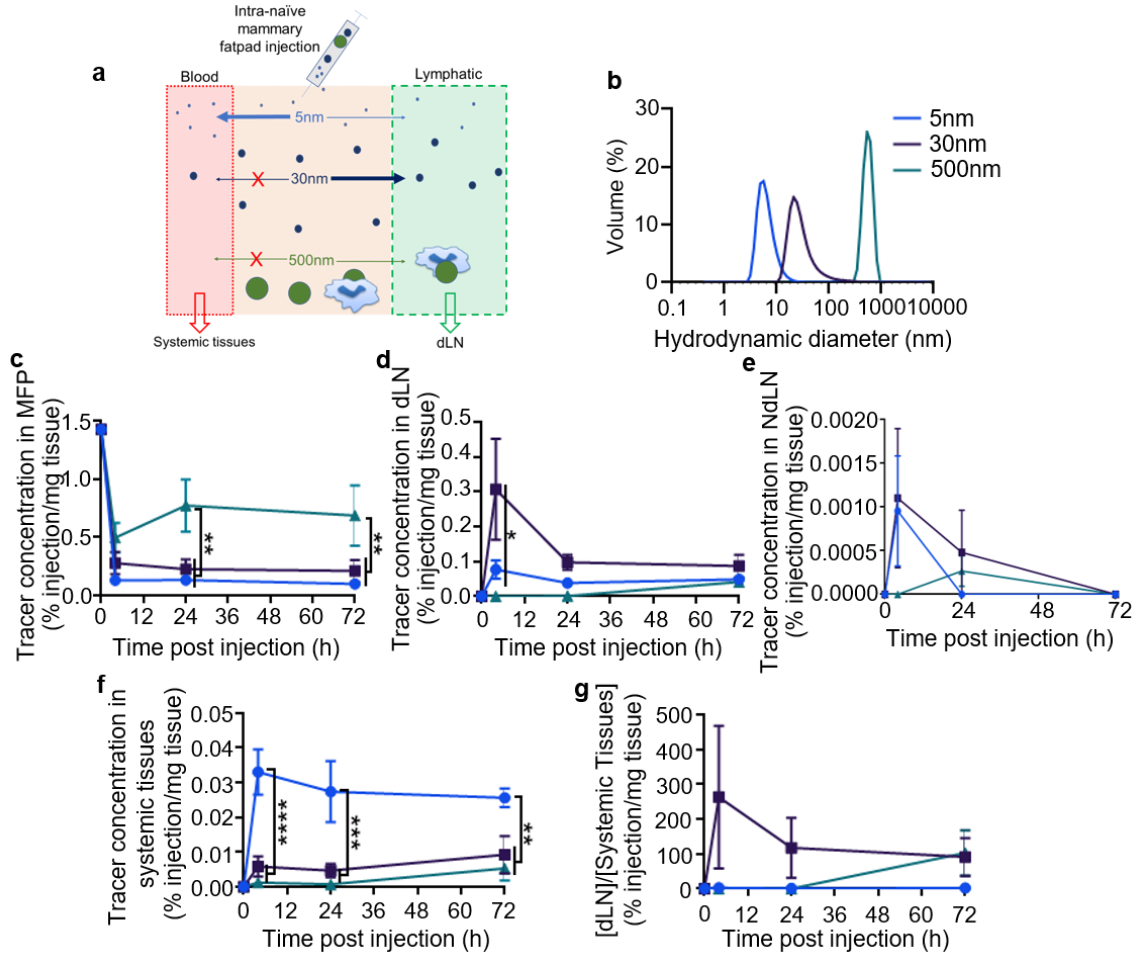


Figure 4.4: Dynamics of macromolecular distribution from the MFP are size-dependent. (a) Schematic of molecular clearance routes from the intra-mammary fatpad. (b) Dynamic light scattering tracer measurements. (c) Tracer retention at the mammary fatpad injection site over 72 h. (d-f) Tracer accumulation within draining (d) and non-draining (e) LN and spleen, liver, lungs, kidneys (f) over 72 h post injection in the mammary fatpad. (g) Relative tracer concentration within dLN compared to systemic tissues (liver, lungs, spleen, and kidneys) from 0-72 h. * indicates significance by two-way ANOVA with Tukey comparison (* indicates $p < 0.05$; ** indicates $p < 0.01$; *** indicates $p < 0.005$; **** indicates $p < 0.001$); $n = 5-6$ mice.

while 500 nm tracers show no detectable accumulation until 72 h after injection (Figure 4.4d), in line with the slower process of active, cell-mediated transport [81, 100, 189]. One hundred-fold higher levels of tracer accumulation within LNs ipsilateral compared to contralateral to the MFP site of injection are indicative of this transport being lymphatic-mediated (Figure 4.4d, e). 5 nm tracers, which are blood-permeable, rapidly access systemic tissues, followed by a slight decline, while 30 and 500 nm tracers accumulate gradually throughout time in systemic tissues (Figure 4.4f). These transport patterns allow for significant concentration (~2 orders of magnitude higher) of 30 nm tracers in the dLN compared to systemic tissues early on; very low concentration of 5 nm tracer in dLN relative to systemic tissues; and a late peak in 500 nm tracer dLN accumulation at 72 h, a time scale consistent with being mediated by lymphatic trafficking cells [81, 100, 189] (Figure 4.4g).

This tracer panel was injected i.t. into animals bearing d7, 14, or 21 E0771 tumors and levels of fluorescent tracer accumulations within each tissue analyzed. Retention of 500 nm tracers at the site of injection was largely unchanged throughout tumor progression compared to the naïve MFP, but 30 and 5 nm tracers were retained to greater extents in d7 versus d14 and 21 tumors, respectively (Figure 4.5a). These changes are indicative of altered vascular functions within these diseased tissue microenvironments and consistent with increased tumor vascular volume (d14 and 21) and VEGF-A levels (d21) at these disease stages (Figure 4.2a-e). Indeed, accumulation of i.t. injected 5 nm tracers within kidneys, and 500 nm tracers in the liver was increased in late stage (d21) disease (Figure 4.5b) when the most profound levels of measured vascular remodeling within the TME were observed (Figure 4.2), suggestive of increased clearance into the tumor vasculature.

Likewise, 30 nm tracer access to the spleen decreased in d7 and 14 tumors, but increased in late stage (d21) disease when 5 and 500 nm tracer accumulation in blood-rich tissues was increased (Figure 4.5b). This increase coincided with increases in PDL1 expression by CD45⁻ and CD45⁺ cells within spleens of d21 E0771 tumor-bearing animals (Figure 4.1e). Accumulation by MFP-injected tracer within spleens of tumor-bearing relative to naïve mice did not coordinate with increased splenic MDSC frequencies, however. Changes in expression of PDL1 by splenic cells, but no MDSCs are thus synchronous with altered tumor vascular permeability/function profiles in the E0771 TNBC model.

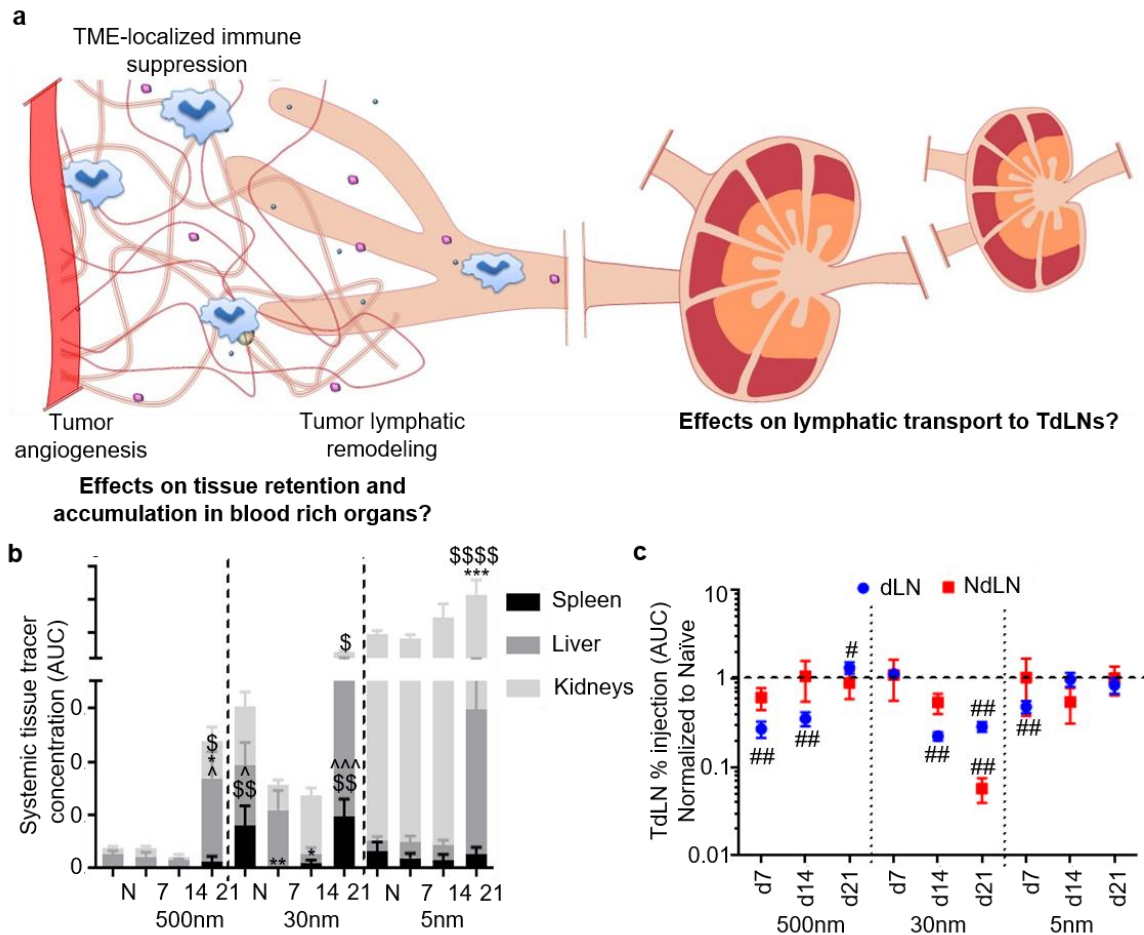


Figure 4.5: Molecular dissemination from breast tumors is altered by E0771 disease and progression. (a) Vascular and lymphatic remodeling of the TME may impact

molecular dissemination into systemic tissues versus dLN. (b) Tracer accumulation within systemic tissues (spleen, liver, and kidneys) of naïve (N) and d 7, 14, and 21 tumor-bearing animals over 72 h post-injection as quantified as concentration AUC. (c) Relative change in levels of tracer accumulation within the dLN and NdLN over 72 h post-injection quantified as % injection AUC. * indicates significance relative to naïve; \$ indicates significance relative to d7, and ^ indicates significance relative to d14, all by two-way ANOVA with Tukey's comparison; # indicates significance relative to theoretical value of 1.0 by one-sample t test (*, ^, \$, # indicate p<0.05; **, \$\$, ### indicate p<0.01; ^^^ indicates p<0.005; \$\$\$\$ indicates p<0.001); n=5-6 mice.

Tumor lymphatic transport was assessed by measurement of accumulation of tracers injected into the MFP within LNs. 500 nm tracer injected into the MFP accumulated within TdLNs at reduced levels as early as d7 post-tumor implantation (Figure 4.5c). This is suggestive of vascular and lymphatic remodeling of the MFP induced by the tumor diminishing cell trafficking from the TME, effects sustained at d14 but reversed by d21 (Figure 4.5c). Tumors had no effect on 30 nm tracer accumulation within the primary TdLN in early-stage (d7) disease but accumulation was dramatically reduced at later stages (Figure 4.5c). Accumulation of 5 nm tracer within TdLN was reduced in d7 tumor-bearing animals but overall levels were unchanged relative to the naïve (tumor-free) MFP at later tested stages (Figure 4.5c). In support of these observed changes in tracer accumulation being associated with altered tumor lymphatic transport, levels of accumulation with NdLNs remained unchanged irrespective of the tumor, save for reduced levels of 30 nm tracer measured in NdLNs of d21 tumor-bearing animals (Figure 4.5c). Thus, lymphatic mediated cell trafficking was initially inhibited by tumor growth but recovered in late stage disease. Lymphatic drainage on the other hand was sustained early in tumor development but then decreased substantially as disease progressed, diminutions that coincided with increased PDL1 expression by CD45⁺ cells within LNs (Figure 4.4d). Immune suppression

within the TdLNs is thus coincident with disease stages when tumor Ag would presumably be locally less abundant.

4.3.3 Primary and Secondary TdLNs are Niches Enriched in Factors Derived from the TME that Support Lymphocyte Viability, Ag Experience, and Proliferation

Antitumor immunity has been observed within lymphoid tissues of TNBC patients [35, 44, 165, 169]. The likelihood of priming and cell expansion occurring locally, irrespective of the locally immune suppressed state, within spleens versus LNs within the tumor lymphatic drainage basin was thus evaluated in the E0771 model using the tracer system. Disease associated changes in transport to axillary LNs that drain the primary LN (inguinal) draining the MFP [190], referred to as the secondary dLN, were measured in the context of E0771 TNBC to evaluate their potential to support antigenic priming (Figure 4.6a, b). Accumulation by tracer injected into the naïve MFP in the secondary dLN followed the same tracer size- and time-dependent trends as the primary dLN, but at a lower magnitude (Figure 4.6c, d). In a tumor context, levels of MFP injected 30 nm tracer access that is sustained for primary TdLNs in early stage disease (d7) were instead enhanced for secondary TdLNs in early stage disease (d7, Figure 4.6c-e). At later stages (d14 and 21) when tracer access to primary TdLNs is substantially reduced, accumulation within secondary TdLNs also diminished, but only to levels similar to that for LNs draining the naïve MFP (Figure 4.6c, d). 500 and 5 nm tracer access to both TdLNs remained low and relatively unchanged (Figure 4.6c-e). Thus, lymphatic transport to secondary TdLNs is increased or remains relatively unchanged during disease progression. This is suggestive of the entire lymphatic drainage basin and both (primary and secondary) TdLNs being bathed in tumor-derived material, including tumor Ag. The high level of relative

enrichment in factors derived from the TME within primary TdLNs compared to systemic tissues is also seen in secondary TdLNs, save in late stage (d21) disease (Figure 4.6f-g).

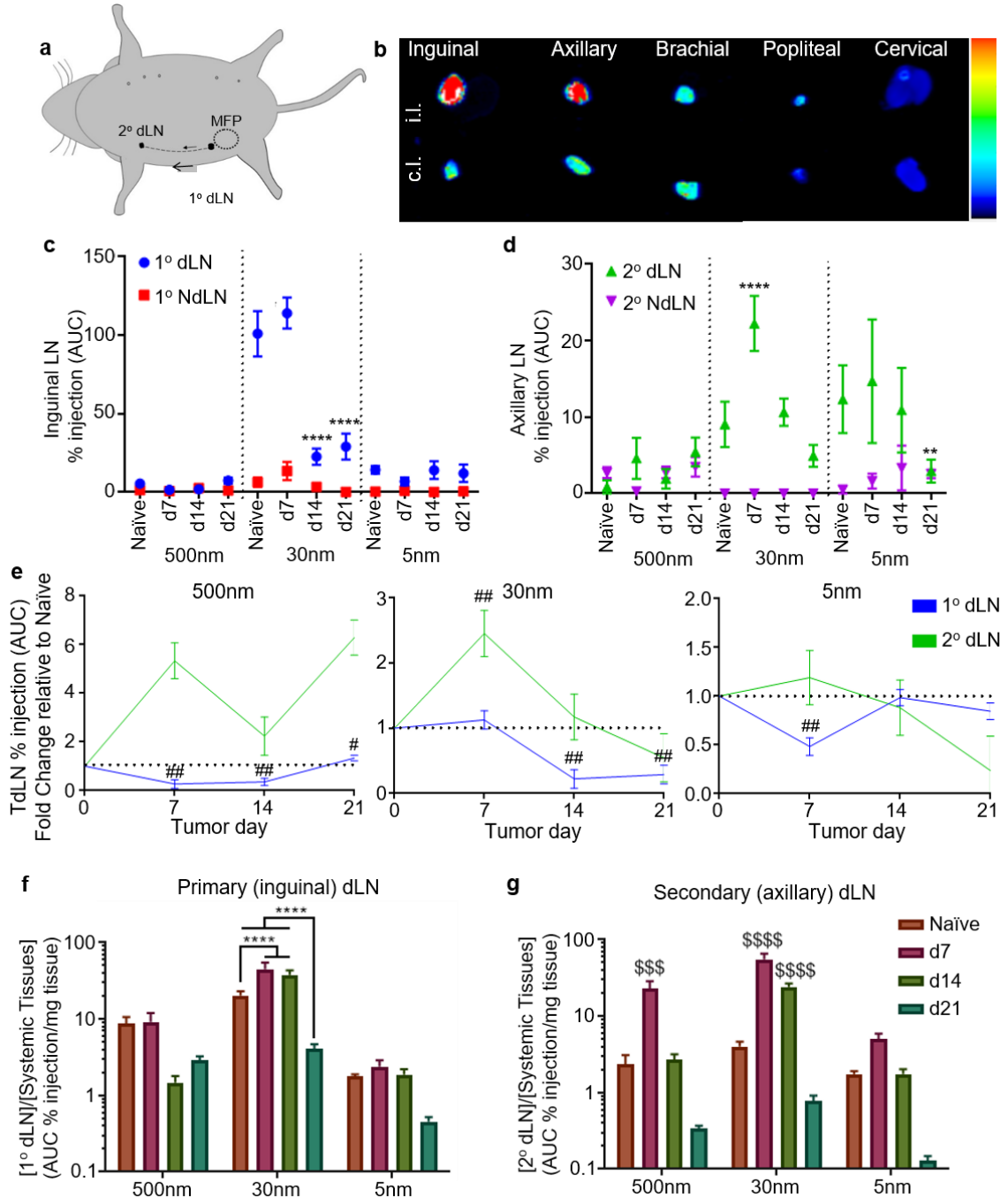


Figure 4.6: E0771 disease progression impacts accumulation of intra-MFP injected tracers within inguinal and axillary LNs. (a) Schematic showing approximate locations of fourth (inguinal) MFP [location of tumor implantation], dLNs (inguinal

and axillary), and contralateral nipples as reference points. (b) IVIS images of excised draining (ipsilateral) and non-draining (contralateral) inguinal, axillary, brachial, popliteal, and cervical LNs 24 h after injection of Alexa Fluor 647-labelled 500 kDa (30 nm) dextran into MFP. Levels of tracer accumulation in the inguinal (1^o) (c) and axillary (2^o) (d) dLN and NdLNs over 72 h post-injection during tumor development quantified as % injection AUC. (e) Fold change in tracer accumulation within TdLNs over 72 h post-injection in the MFP (% injection AUC) relative to naïve animals. Ratio of tracer concentrations within primary (f) and secondary (g) dLNs relative to systemic tissues (liver, kidneys, spleen, lungs) of 72 h post injection the mammary fatpad of naïve or E0771 tumor bearing animals at different stages of disease as quantified by concentration AUC. * indicates significance by two-way ANOVA with Tukey's comparison; # indicates significance relative to theoretical value of 1.0 using one-sample t test; \$ indicates significance relative to all other groups by two-way ANOVA with Tukey's post-hoc test (# indicates p<0.05; **, ## indicate p<0.01; \$\$\$ indicates p<0.005; ****, \$\$\$\$ indicate p<0.001); n=5-6 mice

The relative propensity for various lymphoid tissues to support extratumoral priming by CD8⁺ T cells against tumor Ag was next assessed by evaluation of responses by CFSE-labeled OT-I CD8⁺ T cells adoptively transferred 2 d prior into E0771-OVA tumor-bearing animals within primary and secondary TdLNs, NdLNs, and spleens. In early d7 E0771 tumors, proliferation was robust in both primary and secondary TdLNs (Figure 4.7a,b.i), with a ~4 order of magnitude increase in cell density compared to the TME [peak generation cell count of 200 (Figure 4.1) versus 10,000 per 10⁶ total live cells]. Proliferation also appeared somewhat more advanced compared to within the TME, with peak generation cell counts being roughly equivalent between G3 and 4 within the primary and secondary TdLNs (Figure 4.7b.i) compared to G3 within the TME (Figure 4.7e.i). In contrast, proliferation of tumor Ag-specific CD8⁺ T cells in animals bearing d21 tumors was severely limited by comparison, more closely mirroring cell responses seen within the TME (Figure 4.7a,b.ii). Nonetheless, expansion in lymphoid tissues resulted in a higher number of proliferating cells compared to the tumor (Figure 4.7c). This led to substantial numbers of tumor-specific T cells in both primary and secondary TdLNs (Figure

4.7c). These lymphoid tissue-resident tumor Ag-specific CD8⁺ T cells were also largely (>80%) viable (Figure 4.7d, e), with the exception of unproliferated cells 48 h post-transfer into d7 tumor-bearing animals (Figure 4.7d,e), in sharp contrast to the low viability of these cells within the TME (Figure 4.1d, f). Notably, proliferated and unproliferated donor cells exhibited the highest viability in both primary and secondary TdLNs regardless of tumor

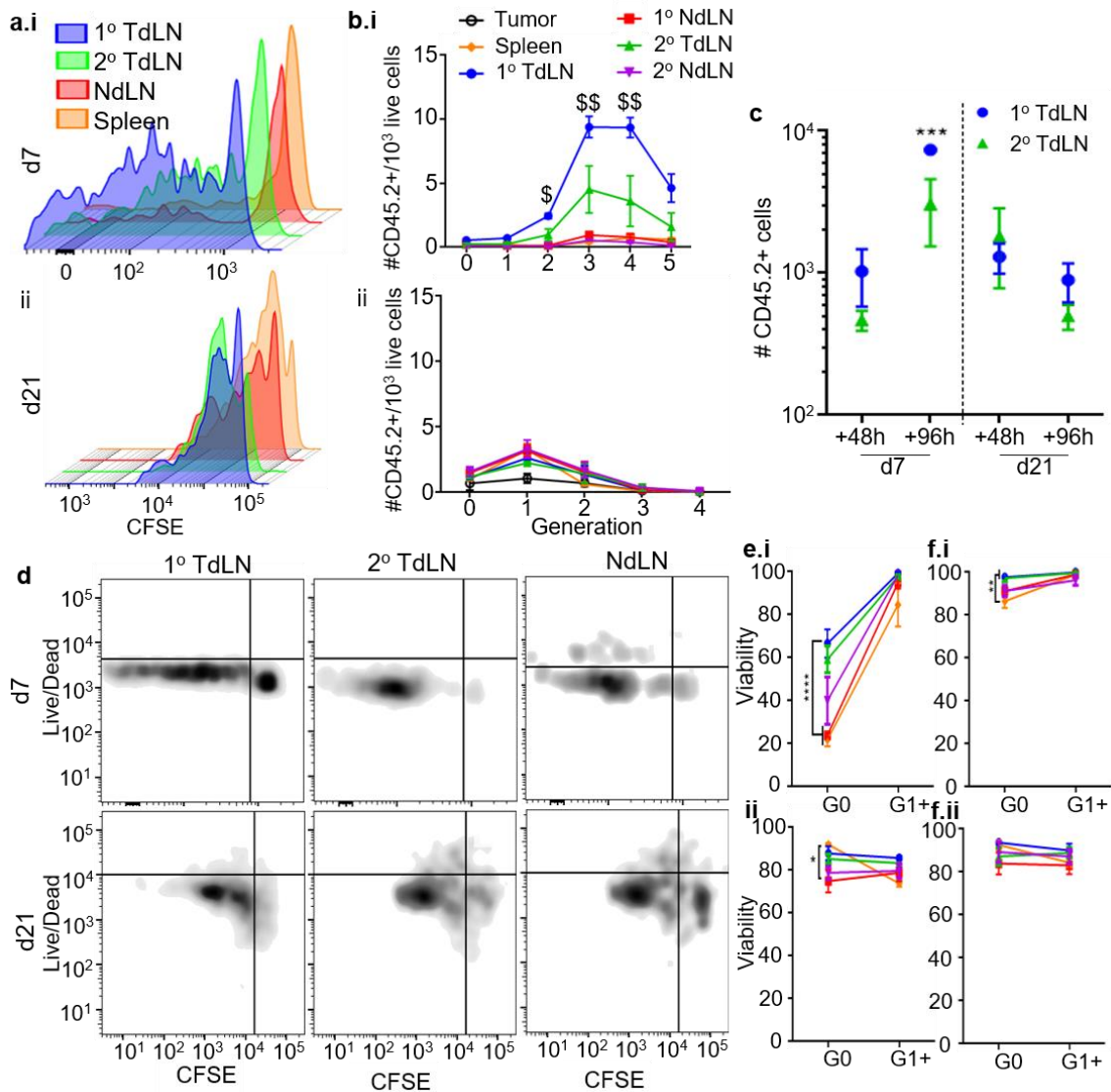


Figure 4.7: Tumor Ag-specific T cell priming occurs in E0771 TdLNs. Representative CFSE dilution plots (a) and relative densities of each proliferative generation per 10³ cells (b) of OT-I CD8⁺CD45.2⁺ donor T cells 48 h post-adoptive

transfer into d 7 (i) and 21 (ii) E0771-OVA tumor-bearing CD45.1 animals within lymphoid tissues and TME. Total number (c), representative Zombie live/dead and CFSE staining flow cytometry plots (d) and viability (e-f) of tumor Ag-specific (OT-I) CD8⁺CD45.2⁺ T cells 48 (c-e) or 96 h (f) post-adoptive transfer in 1^o (inguinal) and 2^o (axillary) dLNs (c-f), NdLNs (d-f), spleens (e-f), or TMEs (e-f) of d 7 or 21 E0771-OVA tumor-bearing animals. * indicates significance by two-way ANOVA with Tukey's comparison; \$ indicates significance relative to all other groups (including tumor) by RM ANOVA; n=5-6 mice.

stage (Figure 4.7d, e). Lymphoid tissues highly enriched in factors derived from the TME thus support both proliferation and viability among tumor-specific T cells, effects diminished in later-stage disease when these environments exhibit immune suppression.

Phenotypes of TME- and lymphoid tissue-resident T cells were also assessed in E0771 tumor-bearing animals. Viable tumor-specific CD8⁺ T cells within both tumors and primary TdLNs draining early-stage tumors showed high extents of activation (CD44⁺) and Ag experience (PD1⁺) (Figure 4.8a, b), while cells in the spleen of these animals were primarily naïve (CD44⁻) (Figure 4.8a, b). Within secondary TdLN, roughly 50% of cells were both naïve and Ag-experienced (Figure 4.8a, b). As a whole, this indicates that the tumor along with primary and secondary TdLNs demonstrate higher levels of Ag experience in early stage E0771 tumors, while cells in the spleen remain in a more naïve state. In late-stage tumor-bearing animals, on the other hand, CD8⁺ T cells were more evenly distributed between naïve and Ag-experienced subtypes in the primary TdLN and spleen, changes that are consistent with decreased lymphatic drainage and increased levels of splenic accumulation, respectively (Figure 4.8a, b). Among PD1⁺ cells, most tumor-specific cells within lymphoid tissues were in the stem-like (Tcf1⁺Tim3⁻) state [40, 41] in both early and late stage disease (Figure 4.8c). However, a majority were Tim3⁺Tcf1⁻, characteristic of an effector/exhausted state [40, 41] in the TME (Figure 4.8c). We next

analyzed expression of CD25, a marker for activation, and found that CD45.2⁺ cells were most activated in the tumor 96 h after transfer on both d7 and 21 (Figure 4.8d). However, on d7 of tumor growth, cells in the primary TdLN showed slight expansion in activation relative to the secondary TdLN and spleen, and at d21, cells in the secondary TdLN show high levels of activation. Thus, not only are these cells expanding and experiencing Ag, but they are becoming activated. As exhausted cells can express activation markers, we

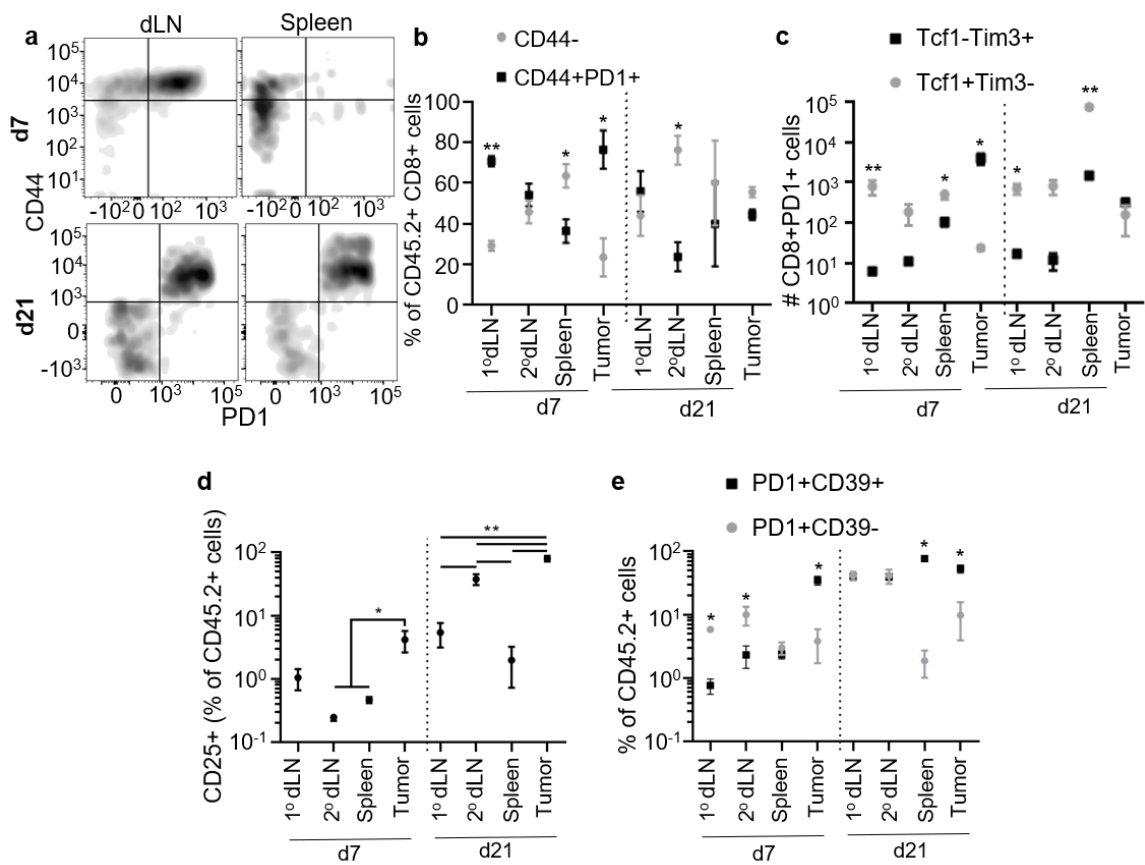


Figure 4.8: Quality of endogenous CD8⁺ T cells within lymphoid tissues and TME changes during E0771 disease progression. Representative CD44 and PD1 flow cytometry staining (a), fraction of CD44⁻ versus CD44⁺PD1⁺ of total CD8⁺ T cells (b), number of Tim3⁺Tcf1⁻ or Tcf1⁺Tim3⁻ PD1⁺CD8⁺ T cells (c), fraction of CD44⁺CD25⁺ cells of CD45.2⁺ cells (d), and fraction of PD1⁺CD39⁻ versus PD1⁺CD39⁺ of CD45.2⁺CD44⁺ cells (e) in lymphoid tissues (a-e) or TME (b-e) of d 7 or 21 E0771 tumor-bearing animals. * indicates significance by Mann-Whitney U test (* indicates p < 0.05, ** indicates p < 0.01); n=5-6 mice.

next compared CD39 levels, a marker for exhaustion [149]. This revealed that in early stage (d7) disease, primary and secondary TdLNs, cells were not exhausted (CD39⁺), but primarily PD1⁺CD39⁻, while cells within the tumor were mostly exhausted (CD39⁺PD1⁺) (Figure 4.8e). In d21 tumor-bearing animals, TdLNs harbored a more even split between exhausted and Ag-experienced cells; however, both the spleen and tumor contained primarily exhausted cells (Figure 4.8e). Thus, cells within the TdLNs are activated and likely to be functional, with the primary and secondary TdLN showing the highest activation on d7 and 21, respectively, while cells in the tumor are exhausted. TdLNs thus maintain a population of Ag-experienced CD8⁺ T cells which have the potential to be invigorated by ICB.

4.3.4 Both Primary and Secondary TdLNs are Therapeutic Targets for ICB Immunotherapy

The sustained Ag access, increased T cell priming, and delayed onset of immune suppression in the diseased MFP TdLNs is suggestive of their potential as therapeutic targets in the context of ICB. To test this hypothesis, responses to a single d11 administration of anti-PD1 ICB directed to the primary (via flank injection) or secondary TdLN (via forelimb injection) compared to systemic administration (i.v. via the jugular vein) were assessed, with isotype mAb control injected in the flank as control (Figure 4.9a, b). Previous reports demonstrate that accumulation in LNs draining E0771 tumors is maintained at similar levels in the TdLNs to those shown here in the naïve dLN [14]. Responses to directed delivery revealed by monitoring tumor growth revealed that targeting ICB to either TdLN resulted in transient tumor shrinkage, in contrast to systemic ICB (Figure 4.9c). At 5 d after treatment, LN-directed treatment increased the number of

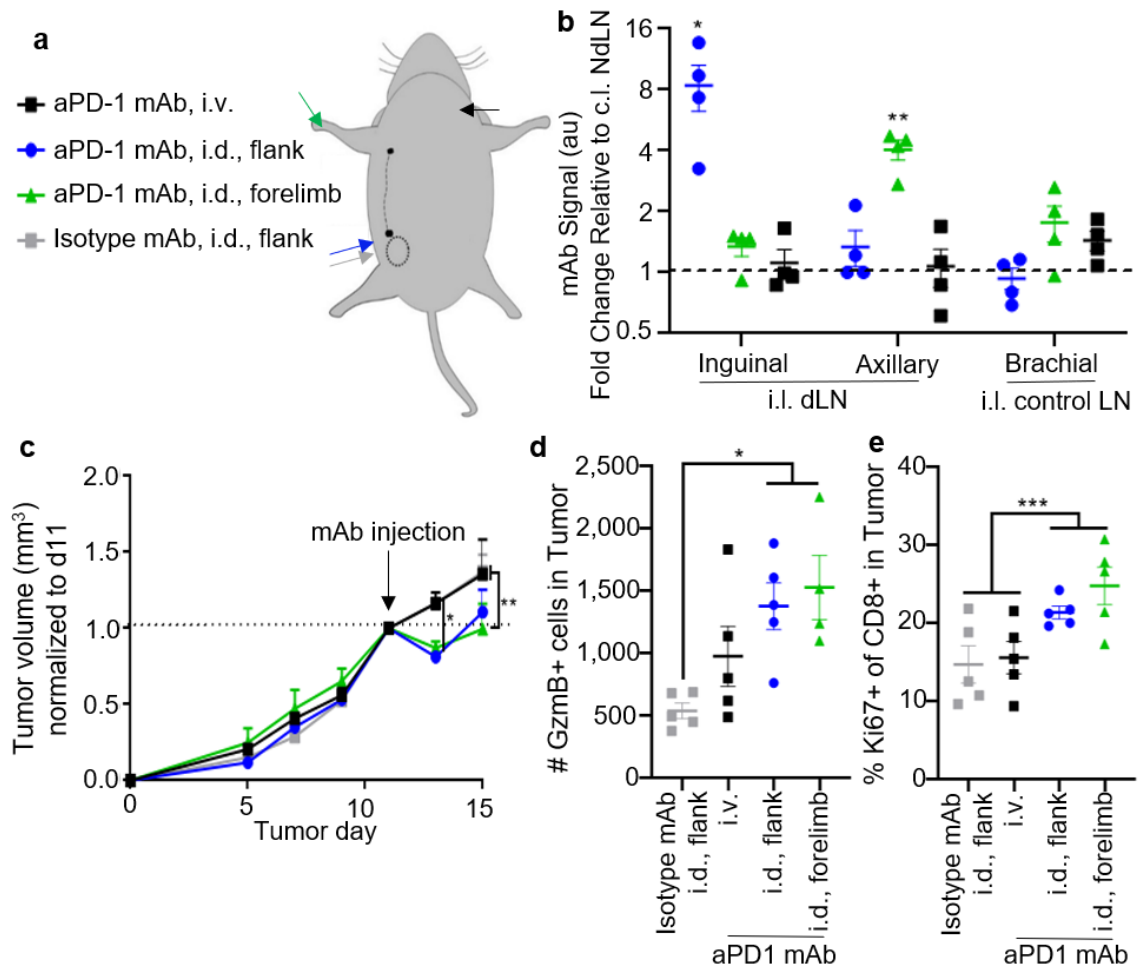


Figure 4.9: Locoregional administration of mAb directed to either 1° or 2° TdLN improves therapeutic and immunomodulatory effects of α PD1 ICB. (a) Schematic depicting routes of i.d. injection targeting 1° (blue, grey) or 2° (green) dLNs versus systemic administration (i.v., black). (b) Fluorescently labeled mAb signal in inguinal, axillary, or brachial (as control) LNs 24 h after i.d. injection in the flank (targeting 1° TdLN), i.d. in the forelimb (targeting 2° TdLN), or i.v. in the jugular vein relative to LNs contralateral to the tumor (NdLN). (c) Relative tumor size in response to treatment with 100 μ g α PD1 mAb on d11. Number of GzmB⁺ (d) and frequency of Ki67⁺ (e) expressing CD8⁺ T cells in the TME in animals on d 15 after tumor implantation. * indicates significance by two-way (a) or one-way (b-e) ANOVA with Tukey's comparison (* indicates $p < 0.05$; ** indicates $p < 0.01$; * indicates $p < 0.001$); $n = 5-6$ animals.**

GzmB-expressing effector CD8⁺ T cells within the TME (Figure 4.9d), along with the frequency of actively proliferating (Ki67⁺) cells (Figure 4.9e), compared to treatment with

either α PD1 intraperitoneally (i.p.) or isotype mAb i.d. as control. Interestingly, neither the number of GzmB-expressing or frequency of Ki67-expressing CD8⁺ T cells was unchanged within the primary or secondary TdLNs or NdLNs based on the route of administration. This implies that T cells primed within the TdLN after targeted delivery of anti-PD1 mAb induces LN-resident T cells to recirculate and reach the TME as functional and proliferating T cells, an interpretation that needs to be confirmed. Thus, by directing ICB mAb to TdLNs, sites of retained Ag access (Figure 4.6), sustained proliferation (Figure 4.7), and Ag experience (Figure 4.8) that results in the generation of a reservoir of tumor-specific stem-like CD8⁺ T cells (Figure 4.8), the response to immunotherapy is enhanced, with resulting functional improvements in T cell phenotype within the tumor itself.

4.4 Discussion

TNBC is a deadly disease impacting millions each year, with very few effective therapeutic treatments [2, 3, 27]. Immunotherapies have shown clinical benefit in treating many solid tumor malignancies, but the only currently approved ICB therapies for TNBC result in responses in just ~16% of patients [29]. A critical hurdle to advancing immunotherapy as an effective approach to combat TNBC is addressing the multiple pathways of immune suppression that result in immunotherapeutic resistance. In particular, there is a growing consensus that T cells require survival niches in order to effectively respond to immunotherapy and result in antitumor effects [160, 191, 192]. As such, overcoming immune exclusion and suppression within the TME is a critical hurdle to improving immunotherapeutic efficacy.

Antitumor T cell responses were assessed during tumor progression in the syngeneic E0771 murine model of TNBC and revealed the importance of non-tumor tissues in the development of these responses. As others have shown in additional preclinical tumor models [151], TME-localized CD8⁺ T cells exhibit poor viability. Those CD8⁺ T cells within the TME that are viable also exhibit limited proliferation and an exhausted phenotype. Thus, CD8⁺ T cells within the TME have a severely diminished likelihood of resulting in robust antitumor effects. In distinct contrast, CD8⁺ T cell survival was high in LNs draining the TME but not in other LNs or spleens. TdLNs also contained high concentrations of Ag-experienced CD8⁺ T cells, an unsurprising observation given these tissues being highly enriched with factors such as tumor Ag, derived from the TME by virtue of lymphatic transport. Notably, a high fraction of these cells exhibit a stem-like phenotype, implicating their potential to proliferate and respond to ICB [40, 41]. Indeed, delivery of anti-PD1 mAb to TdLN using locoregional mAb administration resulted in improved therapeutic effects that were associated with increased tumor infiltration of degranulated effector (GzmB⁺) and proliferating (Ki67⁺) CD8⁺T cells as compared to conventional systemic (i.p.) therapy. Although the proliferation of TdLN-resident CD8⁺ T cells decreased with tumor progression, viability and the stem-like phenotype are maintained in late stage disease. These results support the potential for TdLNs as drug targets to improve ICB response rates and efficacy in TNBC, a hypothesis supported by the improved therapeutic effects of TdLN-directed anti-PD1 in this model.

Tumor development and progression in the syngeneic E0771 murine model of TNBC was shown to result in immune suppression localized to the TME that extended to lymphoid tissues in a manner that was disease stage dependent. Specifically, increased

PDL1 expression within spleens and LNs coincided with altered functions of the tumor vasculature that regulate clearance from the MFP microenvironment, as determined by increased accumulation of i.t. injected tracers in these tissues. Proliferation of tumor Ag-specific CD8⁺ T lymphocytes within both spleens and LNs was also diminished at these disease stages. Remodeling of the tumor vasculature is thus associated with altered immune microenvironments within lymphoid tissues with regulatory functions relevant to antitumor immunity. Unsurprisingly, results also support the concept that these vascular barriers modulate Ag access within lymphoid tissues. At earlier disease stages when tracer accumulation within systemic tissues and PDL1 expression by cells within spleens was decreased or relatively unchanged, CD8⁺ T cell priming was modest to low. However, at later stages when the tumor vasculature had most substantially expanded, levels of vascular permeability-enhancing VEGF-A [176–179] were the highest, and i.t. administered tracers accumulated within systemic tissues to the greatest measured extents, Ag experience and proliferation by CD8⁺ T cells was increased. Though levels of VEGF-C were unchanged during tumor growth, lymphatic drainage was diminished when VEGF-A in the TME was most increased, namely in d14 and d21 E0771 tumors, an observation consistent with the vasculature's role in regulating interstitial pressures and thus the driving force for lymphatic uptake and function [193–195]. Priming of tumor-reactive CD8⁺ T cells within TdLNs was also sustained in early (d7) but not late (d21) stage when cell mediated or lymphatic drainage transport functions, respectively, were diminished in the tumor. Whether the low extent of CD8⁺ T cell priming at d21 results from these decreased levels of TdLN accumulation by lymph-accessing species in the TME or coincident local immune suppression, however, remains unresolved. Given the association of CD8⁺ T cell immunity

with TNBC patient survival [42–44], these results are in line with other reports implicating neoangiogenesis as impairing both survival and responses to therapy in breast cancer [181, 182, 196]. How tumor vascular remodeling might be therapeutically mitigated to improve the effects of immunotherapy in TNBC, however, has yet to be systemically explored.

Lymphatic tissues form networks through which Ag can be disseminated, resulting in access by multiple LNs in a network to tumor Ag in order to elicit lymphocyte priming against tumor Ag. This is particularly important in breast cancer, in which the sentinel LN (primary TdLN) is often resected, but secondary TdLNs are left intact given the waning of complete LN dissection [197–199]. In the context of ICB, delivery of anti-PD1 mAb to either primary or secondary TdLN resulted in improved therapeutic effects compared to conventional systemic therapy. This suggests that locoregional therapy that results in delivery of ICB mAb to LNs draining the TME (either sentinel or secondary TdLNs) is an approach potentially relevant to both neoadjuvant and adjuvant therapeutic application of ICB when sentinel LN biopsy has been performed.

In conclusion, the potential for lymphoid tissues to mediate extratumoral priming of CD8⁺ T cell immunity seen in human TNBC patients was evaluated in the syngeneic E0771 mammary carcinoma mouse model. Results in this model demonstrate TdLNs to be lymphoid tissue niches that support the survival and antigenic priming of CD8⁺ T lymphocytes against lymph-draining Ag. LNs within the tumor lymphatic drainage basin therefore represent a unique, potential tumor immunity reservoir in TNBC for which strategies may be developed to improve the effects of ICB immunotherapy.

CHAPTER 5. NOVEL ENGINEERED *IN VIVO* PLATFORM FOR PHYSIOLOGICALLY RELEVANT BREAST CANCER IMMUNOTHERAPEUTIC TESTING

Breast cancer is the most common cancer among women worldwide, but immunotherapies, one of the most promising tools in the fight against cancer, have yet to reach their full potential for use in breast cancer. This is in part due to insufficient preclinical mouse models to test breast cancer immunotherapies. Here, we develop a novel, *in vivo*, clinically relevant mouse model of breast cancer, which directs immune responses in order to more closely mimic human disease. This is then used as a test bed, revealing differential responses to cancer vaccines based on local tumor immune status.

5.1 Introduction

Breast cancer affects approximately 2.3 million people annually [2, 200]. Immunotherapies are one of the most promising tools in the fight against breast cancer; however, response rates in the clinic are disappointingly low – no vaccine therapies have been approved for breast cancer, despite successes in melanoma and prostate cancer [57, 58]. This suggests an unmet need in understanding the differences in patient responses, and tools to develop new and better immunotherapeutic strategies for patients who are less likely to respond to currently approved immunotherapies.

Currently, a significant amount of research is dedicated to understanding different types of immune responses to cancer. Immunologically “hot” tumors generally have more immune infiltration as a whole, while “cold” tumors simply contain fewer immune cells

[25]. In addition to the broad total immune infiltration stratification, other stratifications have been identified, with the potential to influence immunotherapy responses – among immune-infiltrated (hot) tumors, macrophages and CD8⁺ T cells have been shown to have opposite impacts on patient survival, and on responses to chemotherapy [201]. Likewise, neutrophils and CD8⁺ T cells form unique signatures in human TNBC samples that induce opposing ICB responses [139]. Finally, PD1 expression by CD8⁺ T cells impacts survival opposite to Treg infiltration, demonstrating opposing roles within the same cell subtype [202]. Each of these opposing immune responses have potential ramifications on immunotherapy responses [139, 201]. Thus, many different immune cell signatures have ramifications on overall survival, and immunotherapy and chemotherapy responses. Uncovering these factors which influence therapeutic responses and survival was done both based on analysis of data from human patients, and through experimentation with preclinical models.

Immunotherapy testing is currently accomplished primarily using preclinical mouse models. These mouse models for breast cancer include PDX, GEMMs, and syngeneic tumor models [108]. In PDX, a portion of the patient's tumor is introduced into an immunocompromised or humanized mouse [108]. However, only ~40% of attempts to generate these xenografts succeed in immunocompromised mice [109]. Additionally, immunotherapy responses in xenografts applied to humanized mice can be variable and don't always match responses in actual patients [110–112], making PDX insufficient for immunotherapeutic testing. Alternatively, GEMMs have oncogenic material inserted in the mouse genome in distinct locations to induce tumor formation; one example being the MMTV-PyMT model in which the polyoma tumor virus is expressed in the MFP to

spontaneously form breast tumors in mice [114]. The spontaneous nature of these responses more closely mimics the progression of human tumor pathological characteristics [114, 203]. However, tumor development is extremely variable in location, number of tumors, etc. [204, 205], which presumably induces variation in immune responses, making testing of immunotherapies exceedingly challenging and often impossible. Finally, syngeneic mouse models consist of immortalized mouse tumor cell lines, suspended in either Matrigel or saline, injected into syngeneic, immunocompetent mice [108, 206]. These are commonly used in the field of immunoengineering due to their ease of implementation and the use of immunocompetent mice. However, each cell line tends to induce a different immune response based on tumor cell-intrinsic characteristics (ie. PDL1 expression, antigenicity, etc.) [139], making the study of the varied responses in human tumors impossible in these models. Thus, current preclinical models for immunotherapeutic testing are insufficient in their potential to close the current gaps in immunotherapy responses in the clinic.

Here, we utilize engineered hydrogels which have the potential to direct immune responses [207] in a mouse model of TNBC, to direct anti-tumor immune responses, more closely mimicking the varied patterns of immune responses against human breast tumors. We then use this as a test bed to show that immune status of the tumor alters responses to a cancer “vaccine”.

5.2 Materials and Methods

5.2.1 Cell Culture

E0771 cells (obtained from Swartz Laboratory, EPFL, Lausanne, Switzerland) were cultured in DMEM (Gibco, Thermo Fisher Scientific, Inc.) with 10% heat-inactivated

fetal bovine serum (Gibco, Thermo Fisher Scientific, Inc.) and 1% penicillin/streptomycin/amphotericin B (Life Technologies). Py230 cells (obtained from ATCC, Manassas, VA) were cultured in F-12K medium (Corning, VWR International, Inc.) with 5% heat-inactivated fetal bovine serum (Gibco, Thermo Fisher Scientific, Inc.), 1% penicillin/streptomycin/amphotericin B (Life Technologies), and 0.1% MITO+ serum extender (Corning, VWR International, Inc.). Cells were maintained at 37°C and 5% CO₂ and passaged at ~70-80% confluency using 0.05% (E0771) or 0.25% (Py230) Trypsin-EDTA (Thermo Fisher Scientific, Inc.).

5.2.2 *Animal Tumor Models*

All protocols were approved by the Institutional Animal Care and Use Committee. C57Bl/6 or Nod-Scid-Gamma (NSG) mice were purchased at 6 wks of age from Jackson Laboratory (Bar Harbor, ME). MMTV-PyMT mice were the gracious gift of the Graham lab at Emory University, and bred in house. MMTV-PyMT mice were monitored on a weekly basis throughout tumor development and progression to ensure rodent health. For MMTV-PyMT transplant studies, tumors were excised at approximately 200 mm³ in ellipsoidal volume. After excision, MMTV-PyMT tumors were separated using 18G needles and incubated in 1 mg/mL collagenase D (Sigma Aldrich) in D-PBS for 60 min at 37°C with 5% CO₂. Tumors were then separated by pushing through a 70 µm cell strainer (Greiner Bio-One) twice, washed with D-PBS, and counted for implantation. 5-500 x 10³ E0771 cells, 0.25-1 x 10⁶ Py230 cells, or 1-10 x 10⁶ MMTV-PyMT tumor cells in 30 µL of appropriate scaffold were injected in the fourth (inguinal) MFP. Animals were monitored every 1-3 days during tumor growth. Tumor dimensions were measured with calipers in three dimensions and reported as ellipsoidal volume. Animals were euthanized

if they displayed signs of rodent illness (weight loss >10%, hunched, ungroomed appearance) or if the tumor reached 15 mm in any dimension.

5.2.3 *Flow Cytometry*

Tumor, LN, and spleen samples were excised from animals after CO₂ asphyxiation. Tumor samples were broken up using 18G needles and incubated with 1 mg/mL collagenase D (Sigma Aldrich) in D-PBS for 4 h at 37°C. LN samples were incubated with 1 mg/mL collagenase D (Sigma Aldrich) in D-PBS for 75 min at 37°C. Following collagenase incubation, samples were pushed through 70 µm cell strainers (Greiner Bio-One), washed with D-PBS, pelleted, and plated at appropriate dilutions in a 96-well U-bottom plate (VWR International, Inc.). Spleen capsules were disrupted using 18G needles, pushed through 70 µm cell strainers (Greiner Bio-One), washing with D-PBS, pelleted, and resuspended in 1 mL red blood cell lysis buffer (Sigma Aldrich) for 7 min at room temperature. Samples were blocked with CD16/CD32 antibody (clone 2.4G2, Tonbo Biosciences, San Diego, CA) for 5 min on ice, washed, and stained with a fixable viability dye Zombie Aqua (1:100 dilution, Biolegend, Inc.) for 30 min at room temperature, before quenching with 0.1% bovine serum albumin in D-PBS (flow cytometry buffer). Antibodies were obtained from Biolegend, Inc. unless otherwise specified, and prepared at the following dilutions on the basis of preliminary titrations: APC-Cy7 anti-mouse CD45 (0.625:100), Alexa Fluor 700 anti-mouse CD11b (1.25:100), Brilliant Violet 605 anti-mouse CD64 (2.5:100), Brilliant Violet 711 anti-mouse Ly6C (2.5:100), FITC anti-mouse MerTK (1:100), PerCP anti-mouse Ly6G (eBioscience, Thermo Fisher Scientific, Inc.; 2.5:100), PE-Cy7 anti-mouse CD11c (1.25:100), Brilliant Violet 421 anti-mouse MHC-II (1.25:100), PE anti-mouse CD86 (5:100), and Brilliant Violet 786 anti-mouse F4/80

(2.5:100) for APC panel; or PerCP anti-mouse CD45 (0.625:100), Brilliant Violet 711 anti-mouse CD3 (1.25:100), APC-Cy7 anti-mouse CD4 (0.15625:100), FITC anti-mouse CD8 (0.3125:100), Brilliant Violet 786 anti-mouse PD1 (1.25:100), Alexa Fluor 700 anti-mouse CD25 (1:100), and Brilliant Violet 421 anti-mouse CD44 (5:100) for T cell panel. APC panel samples were then washed and incubated in IC fixation buffer (eBioscience, Thermo Fisher Scientific, Inc.) for 60 min at room temperature in the dark. Cells were then incubated with APC anti-mouse CD206 (2.5:100) in IC permeabilization buffer (eBioscience, Thermo Fisher Scientific, Inc.) for 60 min at room temperature in the dark. T cell panel samples were washed and resuspended in FoxP3/Transcription factor fixation/permeabilization solution (eBioscience, Thermo Fisher Scientific, Inc.) for 60 min on ice in the dark. Cells were then incubated with PE anti-mouse FoxP3 (5:100) in FoxP3/Transcription factor fixation/permeabilization buffer (eBioscience, Thermo Fisher Scientific, Inc.) for 75 min on ice in the dark. Both APC and T cell panel samples were resuspended in flow cytometry buffer and kept at 4°C for a maximum of 48 hours before analysis using a customized BD LSRFortessa (BD Biosciences). Compensation was performed using ArC (for live/dead) or UltraComp (for antibodies) compensation beads (Thermo Fisher Scientific, Inc.) and data analyzed using FlowJo software version 10 (FlowJo LLC, Ashland, OR).

5.2.4 *Gel Formulation*

PEG-4MAL hydrogels were prepared as described previously [208]. Briefly, PEG-4MAL macromer (molecular mass of 22,000; Laysan Bio, Inc, Arab, AL) was dissolved in 4-(2-hydroxyethyl)piperazine-1-ethanesulfonic acid (HEPES) buffer (10 mM in D-PBS, pH 7.4). Adhesive and crosslinking peptides were custom synthesized by GenScript

Biotech (Piscataway, NJ). Adhesive peptides RGD (GRGDSPC) and RDG (GRDGSPC) were dissolved in HEPES buffer at 5 mM (5 x final ligand density, for a final 1 mM ligand concentration and mixed with PEG-4MAL at a 2:1 PEG-4MAL/ligand ratio to generate functionalized PEG-4MAL precursor. Bis-cysteine crosslinking peptide (GCRDVPMSMRGGDRGD) was dissolved in HEPES at a density corresponding to 1:1 maleimide to cysteine ratio after accounting for maleimide groups reacted with adhesive peptide. Cells were resuspended at 5 x final density in sterile saline and kept on ice. A final density of 8.33×10^6 cells were encapsulated in all hydrogels. The functionalized PEG-4MAL (PEG-4MAL:ligand) and cell mixture was combined with the crosslinker at 2:1:1:1 volume ratio (PEG-4MAL:ligand:cells:crosslinker) immediately before injection.

5.2.5 *IVIS Imaging*

Animals were anesthetized using isoflurane anesthesia and placed in a PerkinElmer IVIS Spectrum CT. Alexa Fluor 750 signal was collected every other day until signal was at or below signal from saline-injected animals or animals reached endpoint due to tumor growth.

5.2.6 μ CT

Animals were perfused with D-PBS at the heart followed by neutral buffered formalin (Thermo Fisher Scientific, Inc.) for 5 min, then with saline to rinse, and MicroFil contrast agent (Flow Tech Inc.) catalyzed at viscosity appropriate for small vessels (5 mL lead-based contrast agent, 2.5 mL diluent, 0.25 mL curing agent). Perfused mice were carefully stored at 4°C overnight to cure. The following day, tumors were excised, and imaged using a Scanco Medical μ CT50. μ CT image slices were constrained using manual

selection of the sample outline and processed with a Gaussian filter at a consistent global threshold via the Scanco Medical μ CT Evaluation Program before 3-dimensional reconstruction [170].

5.2.7 *Cytokine Analysis*

Tumor, LN, and spleen samples were excised from animals, flash frozen using liquid nitrogen, and stored at -80°C . BioPlex lysis buffer (Bio-Rad) was prepared and 100 μL added to each sample. Tissues were mashed using P200 pipette tips until a smooth solution formed. Samples were oscillated at 4°C for 20 min, spun down, and tissue lysate collected and frozen at -80°C . The following day, total protein content was measured using Pierce bicinchoninic acid assay (Thermo Fisher Scientific, Inc.). Milliplex MAP 32-plex mouse cytokine/chemokine magnetic bead panel (Millipore Sigma) was used to assess cytokine and chemokine content in samples. In brief, samples were added to plate at appropriate dilutions with premixed magnetic beads (Milliplex) in assay buffer (Milliplex) and incubated on a plate shaker overnight at 4°C . Samples were then placed in magnetic plates, decanted, and washed. Detection antibodies (Milliplex) were added to each sample and incubated for 1 hr at 4°C on plate shaker. Streptavidin-PE (Milliplex) was added directly to each well and incubated for 30 min at 4°C on plate shaker. Samples were then placed in magnetic plate, decanted, and washed. Samples were resuspended in 100 μL drive fluid and analyzed using a MagPix system (Luminex, Austin, TX).

5.2.8 *Therapeutic Studies*

E0771 tumor cells (50,000 cells) were implanted in immunocompetent C57/B16 mice in saline, Matrigel, PEG-RGD, or PEG-RDG, and tumors measured every other day.

Animals were randomized among cages and researchers were blinded to scaffold. Animals were randomly pre-assigned to a therapeutic group. Once tumors reached $\sim 100 \text{ mm}^3$ in ellipsoidal volume, animals received first treatment and had reached d 0. Animals assigned to receive CpG therapy received $3 \mu\text{g}$ ODN 1826 (CpG, InvivoGen, Inc., San Diego, CA) in $30 \mu\text{L}$ sterile saline intratumorally on d 0 and d 7. Animals assigned to isotype mAb group were given $100 \mu\text{g}$ each of rat IgG2a anti-trinitrophenol (BioXCell) and polyclonal Armenian hamster IgG (BioXCell) intraperitoneally on d 0, 3, and 6. Tumor volume and animal weight was monitored every other day until animals reached the predetermined endpoint (tumor size of 15 mm in any dimension or if the animal displayed signs of rodent illness).

5.2.9 *Statistical Analysis*

Data are represented as the mean accompanied by SEM, and statistics were calculated using GraphPad Prism 6 and 8 software (GraphPad Software, Inc.). Statistical significance was defined as $p < 0.05$, 0.01, 0.005, 0.001 unless otherwise specified.

5.3 **Results**

5.3.1 *Current Mouse Models of Breast Cancer are Insufficient for Immunotherapeutic Testing*

While expensive, GEMMs are currently thought of as the most physiologically relevant mouse model to study cancer development [26]. We thus assessed tumor growth in MMTV-PyMT [114] mice on a C57/B16 background, and found remarkable variation between animals in terms of size of tumors throughout development (Figure 5.1a).

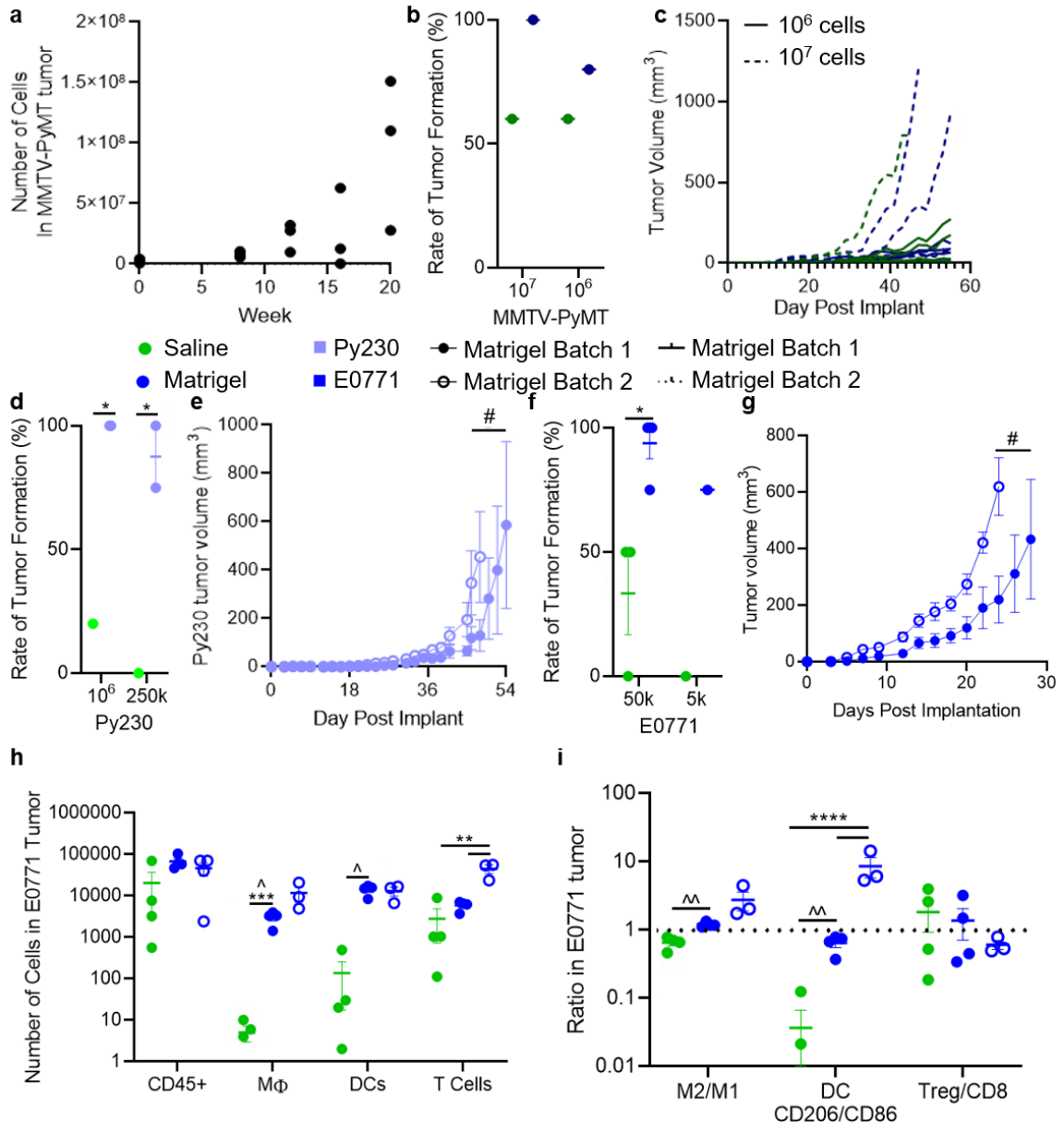


Figure 5.1: Current preclinical models of breast cancer are insufficient. (a) Number of cells in excised MMTV-PyMT tumors at wks 8, 12, 16, and 20, and wild-type litter mates (wk 0). **(b)** Rate of tumor formation after transplantation of MMTV-PyMT tumor cells into C57/Bl6 mice, and tumor growth **(c)**. **(d)** Rate of tumor formation at two cell doses in Py230 cell lines, implanted in saline and Matrigel, along with tumor growth curves **(e)**. **(f)** Rate of tumor formation of E0771 cells at two different doses in saline and Matrigel, and tumor growth curves **(g)**. Number of total lymphocytes (CD45⁺), macrophages, DCs, and T cells **(h)** and phenotype of macrophages, DCs, and T cells **(i)** in E0771 tumors at d 7 post implantation in saline or two different batches of Matrigel. * indicates significance by two-way ANOVA with Tukey’s post-hoc comparison; # indicates significance by RM ANOVA with

Tukey's post-hoc comparison; ^ indicates significant difference in variance by Brown-Forsythe test; n=4-5 animals (*, #, ^ indicate p<0.05; **, ^^ indicate p<0.01; * indicates p<0.005; **** indicates p<0.001).**

These variations in tumor growth make immunotherapeutic testing in these models challenging and excessively expensive. As such, we excised MMTV-PyMT tumors and reimplanted tumor cell suspensions into immunocompetent C57/Bl6 mice. Cells were suspended in Matrigel, a commonly used compound generated from mouse sarcomas [209, 210]; or saline, the common alternative to Matrigel, which is simply sterile water with Na⁺ and Cl⁻ and thus likely to have less batch to batch variation. Implantation in saline resulted in only 60% tumor formation at a dose of either 10⁶ or 10⁷ cells (Figure 5.1b). Matrigel resulted in 100% tumor formation at a cell dose of 10⁷ cells (Figure 5.1a), but growth patterns were inconsistent (Figure 5.1c). While advantageous in their pathological development's relevance to human disease, MMTV-PyMT tumors thus seem relatively inconsistent in tumor growth, either *in situ*, or after transplantation into immunocompetent mice.

In order to address the limitations of MMTV-PyMT tumors, we next assessed growth patterns of Py230 cells, a cell line derived from MMTV-PyMT mice thought to be less differentiated compared to typical immortalized cell lines [211]. Py230 cells were implanted into C57/Bl6 mice at a cell dose of either 0.25 x 10⁶ or 10⁶ cells, suspended in saline or Matrigel. Only 2/10 of the animals that received 10⁶ cells, and none of the animals which received 0.25 x 10⁶ cells in saline developed tumors (Figure 5.1d). However, 100% and ~90% of animals receiving 10⁶ and 0.25 x 10⁶ cells in Matrigel (Figure 5.1d) developed tumors. Since Matrigel seemed to be more consistent, we next assessed the impact of

different batches of Matrigel on tumor growth, and found that tumor latency (Figure 5.1e) differed between the two batches of Matrigel.

The majority of preclinical immunotherapeutic studies are conducted using immortalized cell lines [212] such as the E0771 TNBC line. Since this is the more commonly used model, we next determined whether E0771 cells recapitulated the trends seen with Py230 cells and transplanted MMTV-PyMT tumors. Of E0771 cells implanted in saline, ~33% and 0% of animals developed tumors after implantation of 50×10^3 and 5×10^3 cells, respectively (Figure 5.1f), mimicking the low rates of tumor formation seen in other models assessed here (Figure 5.1b, d). Tumors developed at much higher rates (75-90%, Figure 5.1f) when implanted in Matrigel, but again, there was a significant difference in tumor latency (Figure 5.1g) between batches of Matrigel.

As consistent immune responses are inherent to consistent immunotherapeutic responses, we confirmed whether the immunological responses to tumors were consistent in E0771 tumors implanted in saline or two different batches of Matrigel. Among major immune cell subtypes (total CD45⁺, macrophages, DCs, and T cells), saline tumors had vastly different infiltration, varying by >2 orders of magnitude between tumors (Figure 5.1h). Each individual batch of Matrigel was much more consistent, varying by less than 0.5 orders of magnitude (Figure 5.1h). This variation in macrophage and DC infiltration was significantly higher in saline tumors than Matrigel tumors (Figure 5.1h). In terms of phenotype of major cell types, measured by M2:M1 ratio of macrophages, CD206:CD86 ratio of DCs, and Treg:CD8⁺ T cell ratio, saline tumors also induced vastly different phenotypes among these cells, again a variation significantly higher than Matrigel tumors among M2:M1 ratio and CD206:CD86 ratio among tumor-resident DCs (Figure 5.1i). Each

batch of Matrigel was consistent in immune response, but the number of T cells varied significantly between batches of Matrigel, and macrophage infiltration trended towards a difference (Figure 5.1h). DC phenotype also varied between the two batches used (Figure 5.1i). This batch to batch variation in Matrigel tumors is likely to impair reproducibility and consistency of results, a major impediment to progress in development of immunotherapeutics, and likely to vary considerably beyond what was captured in the two batches analyzed here. Thus, in three different types of mouse models spanning from GEMMs to orthotopically implanted immortalized cell lines, tumor latency and immune infiltration were inconsistent, making these models insufficient for immunotherapeutic testing and likely contributing to poor reproducibility and application to human disease.

5.3.2 An Engineered Hydrogel System Induces Consistent and Controllable Breast Tumors

In order to address the limitations in current systems, we generated an engineered hydrogel system with controllable degradation and crosslinking rates [213–217], and with the potential for conjugation of adhesive ligands to direct immune responses [207] (Figure 5.2a). This system consists of 4-armed PEG maleimide (PEG-4MAL) conjugated using VPM crosslinker and either RGD or RDG [208, 217] (Figure 5.2a). PEG-4MAL was maintained at low pH prior to injection and mixed with crosslinker immediately before injection to allow for consistent gel formation after injection into the MFP. Both Py230 and E0771 cells implanted in these PEG gels induced tumors in 100% of animals (Figure 5.2b). Tumor growth was consistent between batches of PEG, but differed based on adhesive ligand tethered to the scaffold (i.e. RGD vs RDG, Figure 5.2c), and latency was rapid relative to saline (Figure 5.2c). To assess consistency of immune responses to

hydrogels, tumors were implanted in two different batches of PEG hydrogel, prepared >1 year apart, and immune infiltration assessed d7 post-tumor implantation. This revealed that the number of total lymphocytes (by CD45⁺), macrophages, DCs, and T cells were consistent between batches, with no significant difference in number or variability (Figure 5.2d). Likewise, macrophage phenotype (M2:M1 ratio) and DC phenotype (CD206:CD86 ratio) were equivalent between PEG batches (Figure 5.2e). T cell subset (Treg:CD8⁺ T cell ratio) differed between batches (Figure 5.2e); however, this difference replicated trends seen at d2 in the first batch of PEG, potentially indicating that the difference between batches at d7 was due to slight differences in persistence of T cell subset. Overall, this batch to batch comparison demonstrated improved applicability to immunotherapeutic testing compared to traditional models (Figure 5.1). Finally, to address inconsistency in Matrigel degradation [218], we assessed degradation of PEG scaffolds. The PEG scaffolds degraded in a two-stage fashion, with an initial quick loss of signal followed by ~35 days of slow degradation *in vivo*, trends were due to the inclusion of tumor cells (i.e. Scaffold alone and scaffolds implanted with tumor cells degraded with the same patterns), or adhesive ligand (RGD vs RDG, Figure 5.2f). This is in contrast to Matrigel, which has been shown to degrade inconsistently *in vivo* [218]. Thus, this hydrogel system solved inconsistencies in current preclinical model systems.

As adhesive ligands, and RGD in particular, are likely to impact vasculature and angiogenesis within scaffolds [219, 220], μ CT was used to assess vasculature in animals perfused with Microfil. This revealed that PEG-RGD tumors had higher vascularization (Figure 5.2g), which seemed to be more central within the tumor (Figure 5.2h) compared to PEG-RDG tumors at early stage (d7). This difference disappeared in later stage tumors,

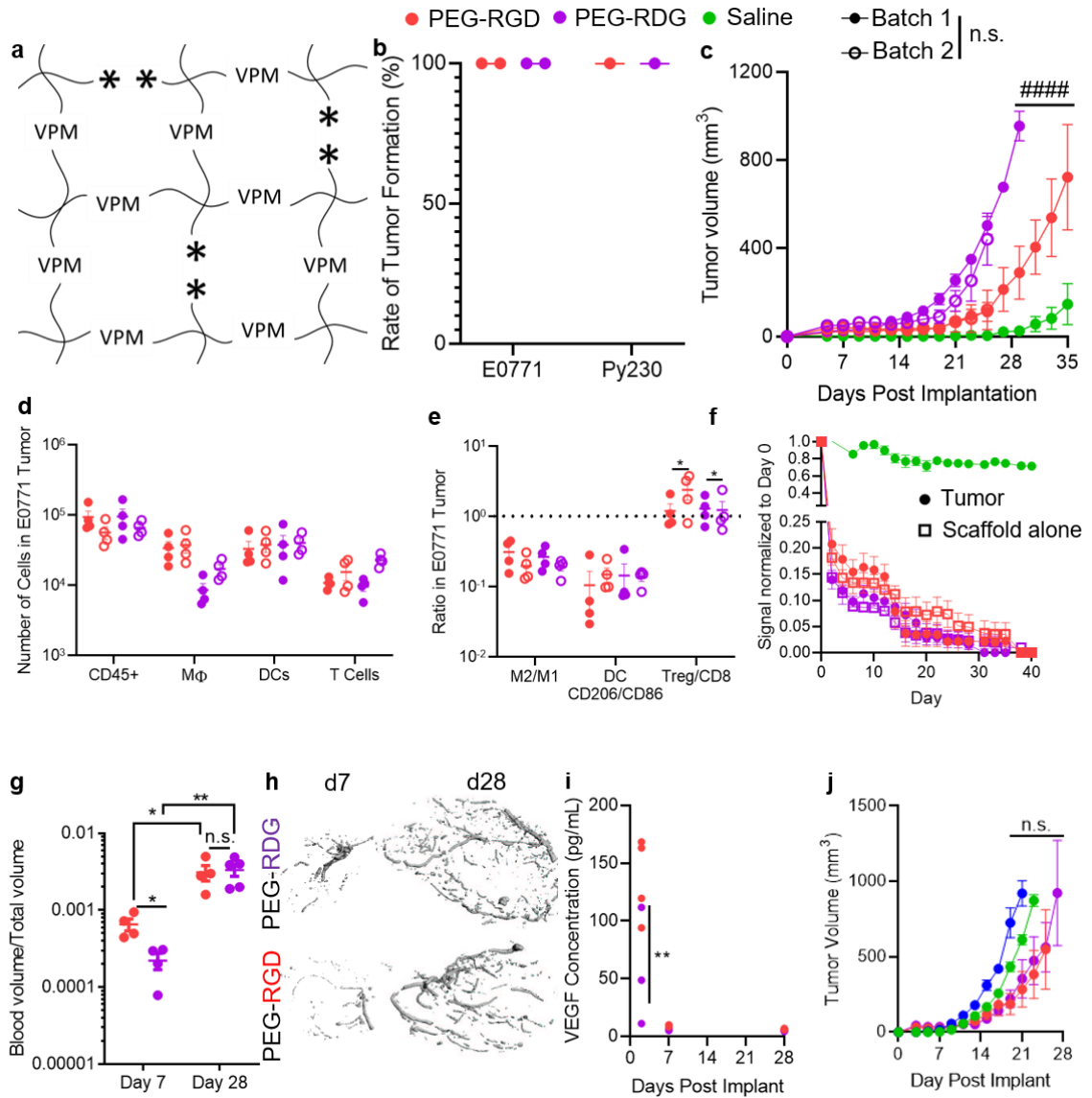


Figure 5.2: Engineered hydrogels induce consistent and controllable tumor immune microenvironments. (a) Hydrogels consisting of PEG-4MAL, with VPM crosslinkers, adhesive ligands (stars). PEG hydrogels induce consistent tumor formation (b) and growth (c). Number of total lymphocytes (CD45⁺), macrophages, DCs, and T cells (d) and phenotype of macrophages, DCs, and T cells (e) in E0771 at d7 implanted in two separate batches of PEG scaffolds prepared >1 year apart. (f) Degradation of Alexa Fluor 750-labelled PEG scaffolds relative to d0 signal, measured by IVIS imaging. (g) Blood volume relative to total tissue volume in tumors implanted in PEG scaffolds at d7 and d28 after implantation, measured by μ CT, with representative images in (h). (i) VEGF concentration of tumors implanted in PEG scaffolds at d2, 7, and 28. (j) Growth of tumors in PEG scaffolds after implantation in immunodeficient NSG mice. * indicates significance by two-way ANOVA with Tukey's post-hoc comparison; # indicates significance by RM

ANOVA with Tukey's post-hoc comparison (n.s., not significant; * indicates $p < 0.05$; ** indicates $p < 0.01$; #### indicates $p < 0.001$); n=4-5 animals.

with both tumor types showing enhanced vascularization relative to d7 (Figure 5.2g-h). These vascularization trends followed an early difference in the concentration of VEGF-A in PEG-RGD tumors relative to PEG-RDG tumors, a difference which was lost in later stage tumors (Figure 5.2i).

Based on the enhanced cell adhesivity of the RGD ligand relative to RDG [213, 214, 221] and the enhanced vascularization of PEG-RGD tumors, one would expect PEG-RGD tumors to have lower tumor latencies and faster growth rates relative to PEG-RDG tumors; however, the opposite was true (Figure 5.2j). We hypothesized that this was due to differential immune responses to these gels [207]. To interrogate this hypothesis, E0771 tumors were implanted in each scaffold into NSG mice which are immunodeficient [222]. This revealed no statistical difference in tumor growth or latency between PEG gels, saline, or Matrigel (Figure 5.2j), supporting our hypothesis. Thus, our engineered hydrogel system induces differential, but consistent, tumor growth based on adhesive ligand that seems to be directed by immune responses to the tumor and scaffold.

5.3.3 Hydrogel-tethered Adhesive Ligands Allow for Induction of Different Immune Microenvironments

In order to further explore ramifications of adhesive ligand on immune responses to tumors in PEG gels, flow cytometry and Luminex assays were utilized to assess immune cell infiltration and cytokine/chemokine levels. This revealed that PEG-RGD tumor-resident DCs displayed higher activation levels relative to PEG-RDG tumors, as measured by CD206:CD86 ratio (Figure 5.3a). As CD8⁺ T cells tend to co-localize with CD86⁺ DCs

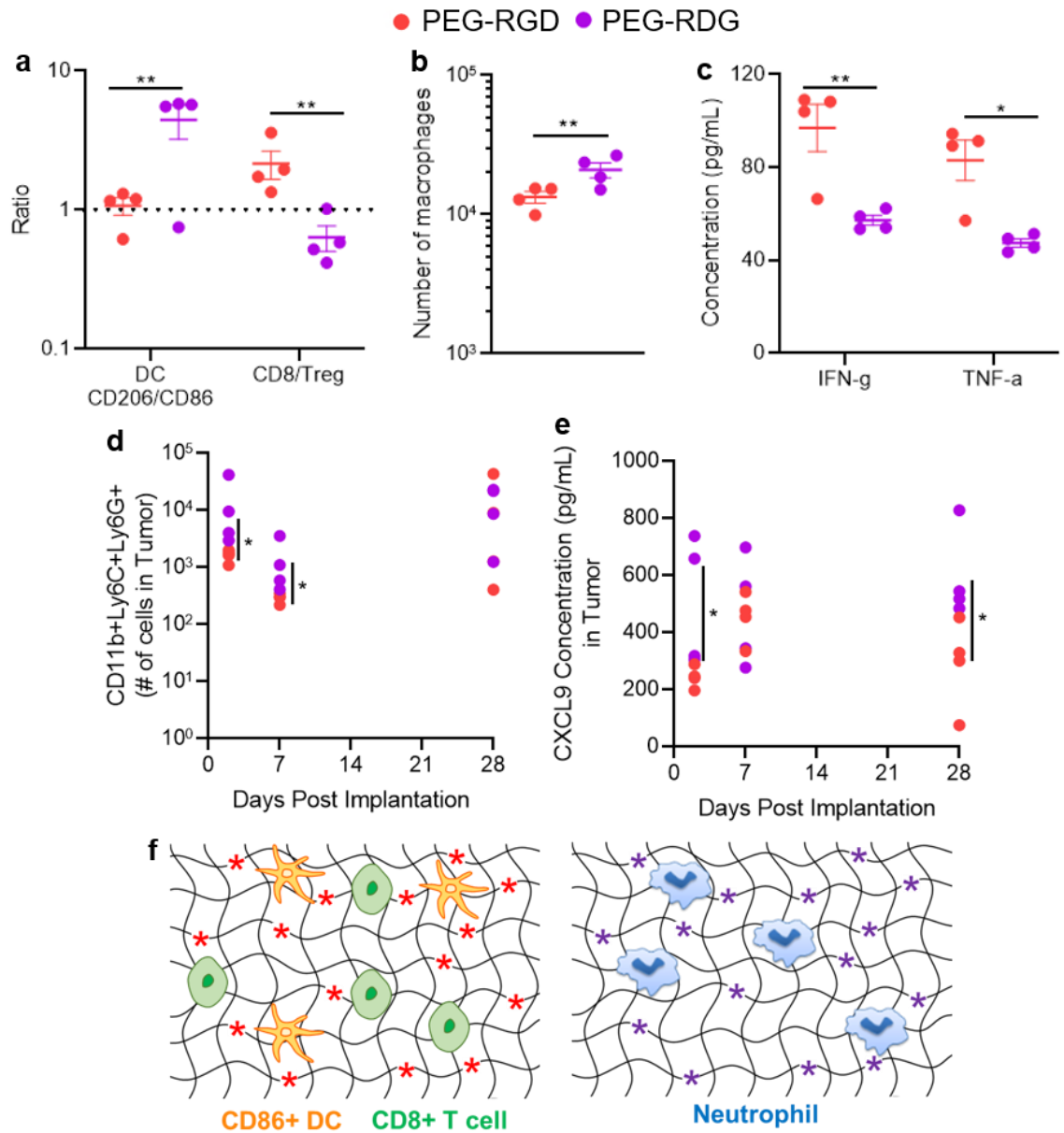


Figure 5.3: Adhesive ligands alter immune responses in engineered hydrogels. (a) CD206:CD86 ratio among DCs and CD8⁺T cell:Treg ratio among T cells infiltrating PEG tumors at d2. **(b)** Number of macrophages within PEG tumors at d2. **(c)** IFN- γ and TNF- α concentration in PEG tumors at d2. **(d)** Number of CD11b⁺Ly6C⁺Ly6G⁺ cells within PEG tumors at d2, d7, and d28. **(e)** Concentration of CXCL9 within PEG tumors at d2, d7, and d28. **(f)** Resulting immune infiltration from RGD (left) and RDG (right) ligands. * indicates significance by one-way ANOVA with Tukey's post-hoc comparison; n=4 animals.

[160], we assessed T cell responses, which revealed that PEG-RGD tumors also had a higher CD8⁺ T cell:Treg ratio compared to PEG-RDG tumors (Figure 5.3a). CD8⁺ T cell infiltration has been associated with decreased macrophage infiltration [201], so we next analyzed the number of macrophages within these early stage tumors. This showed that PEG-RGD tumors had fewer macrophages (Figure 5.3b), aligning with previous reports. The PEG-RGD tumors also had higher concentrations of IFN- γ and TNF- α (Figure 5.3c), cytokines associated with a Th1 response [223]. A higher Th1 response and increased DC activation is expected to coincide with slower tumor growth, as in immunologically hot tumors [25], as we see in these tumors (Figure 5.3c). PEG-RDG tumors, contrastingly, had higher CD11b⁺Ly6G⁺Ly6C⁺ cell infiltration (Figure 5.3d), a cell subtype likely to be neutrophils in the context of cancer [139, 224–227]. CXCL9, a chemokine which can be attributed to neutrophils [228], was also higher in PEG-RDG tumors compared to PEG-RGD tumors (Figure 5.3e). Thus, PEG-RGD tumors induced a primarily CD8⁺ T cell, CD86⁺ DC-driven Th1 response, while PEG-RDG tumors induced a neutrophil response (Figure 5.3f). Previous work has demonstrated that human TNBC tumors tend to develop one of three immune signatures: immune-infiltrated responses driven by neutrophils; immune-infiltrated responses driven by M1 macrophages and CD8⁺ T cells; and immunologically “cold” tumors, generally devoid of immune cells [139, 201]. Here, we were able to engineer a system which mimics the two immune-infiltrated tumor subsets relevant to human TNBC, with PEG-RGD tumors demonstrating a CD8⁺ T cell-driven response, and PEG-RDG tumors demonstrating a neutrophil-driven response.

As both the tumor cells and adhesive ligands tethered to the hydrogel have the potential to alter immune status of developing tumors, we compared infiltration in scaffolds

implanted with or without tumor cells. Phenotype of DCs (CD206:CD86 ratio) and type of T cell (by CD8⁺ T cell:Treg ratio) were identical within PEG-RGD scaffolds implanted with or without tumor cells, indicating that the inclusion of RGD within the scaffold drove this Th1 response (Figure 5.4a). However, within PEG-RDG scaffolds, the CD206:CD86 ratio among DCs trended higher, while the CD8:Treg ratio was lower in scaffolds containing the tumor cells, indicating a tumor cell-driven, not adhesive ligand-driven response (Figure 5.4b). The number of macrophages within each scaffold was independent of whether tumor cells were included (Figure 5.4c-d), indicating that differences seen in Figure 5.3b were directed by the adhesive ligand. Thus, it seems that the Th1 response seen in PEG-RGD scaffolds was directed by the adhesive ligand engineered within the system, while the response in these factors in PEG-RDG scaffolds was tumor-driven. Among neutrophils, which defined PEG-RDG scaffolds, initial infiltration (at d2) was not different between scaffolds implanted with or without tumor cells when implanted with either RGD or RDG (Figure 5.4e-f). However, at d7 and d28, scaffolds implanted with tumor cells had higher neutrophil infiltration (Figure 5.4e-f), indicating a primarily tumor-driven response. Thus, the neutrophil dynamics seen in Figure 5.4d seem to be initially due to adhesive ligand-driven responses, and in later stages (when effects of adhesive ligand are lost), due to a tumor-driven response. As a whole, this indicates that the factors which differentiated the two systems (Figure 5.4f) are due to inclusion of the adhesive ligand, indicating successful engineering of the local microenvironment, and broader applications of this technology to modulate different aspects of responses.

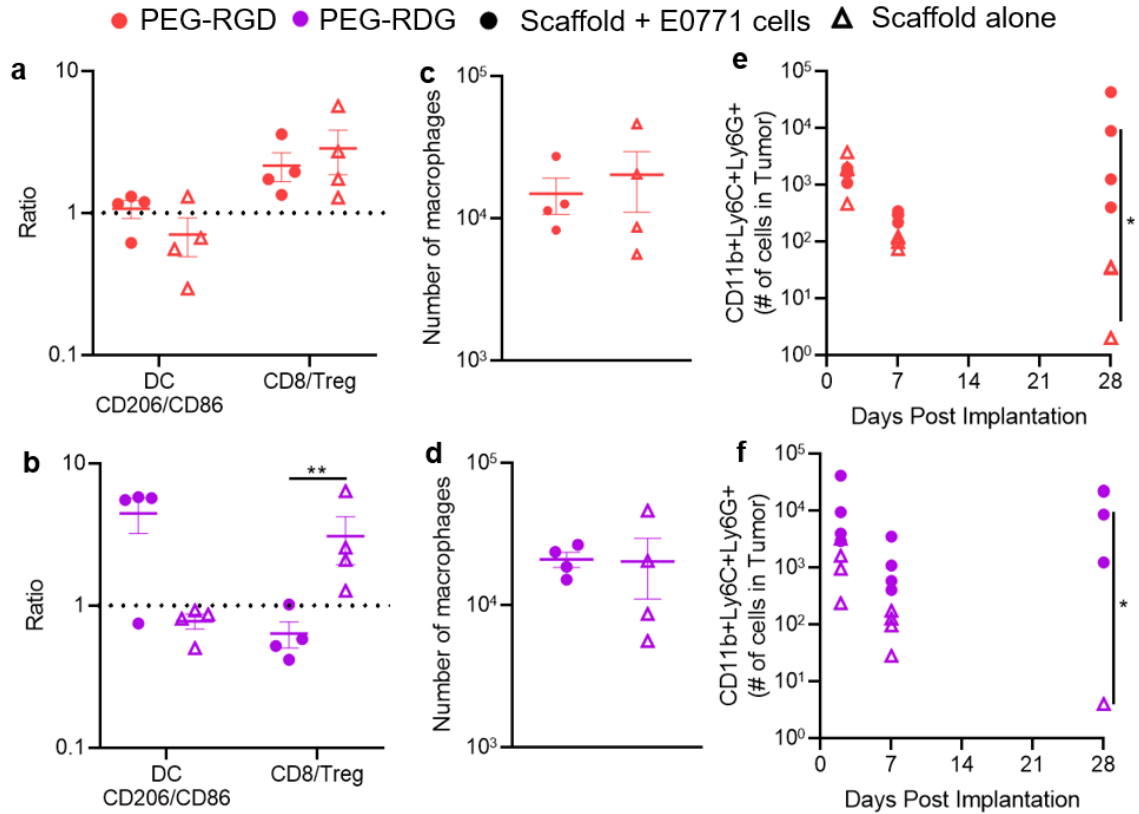


Figure 5.4: Immune status is affected by both tumor-specific and adhesive ligand-specific responses. CD206:CD86 ratio of CD11c⁺ cells (DCs) and ratio of CD8⁺ T cells to CD4⁺ Tregs in PEG-RGD (a) and PEG-RDG (b) scaffolds with or without E0771 cells. Number of macrophages in PEG-RGD (c) and PEG-RDG (d) scaffolds with or without E0771 cells. Number of CD11b⁺Ly6C⁺Ly6G⁺ cells in PEG-RGD (e) and PEG-RDG (f) scaffolds. * indicates significance by two-way ANOVA with Tukey's post-hoc comparison (* indicates p<0.05; ** indicates p<0.01); n=4 mice.

5.3.4 Novel Engineered System Can Be Used to Test Immunotherapeutic Regimens for Breast Cancer

In order to assess the potential of this engineered system to predict immunotherapeutic responses, we assessed responses of tumors to a cancer “vaccine”, in the form of intratumorally injected CpG, a TLR9 agonist. Tumors implanted in saline, Matrigel, and PEG-RGD tumors showed little response to CpG treatment by tumor burden (Figure 5.5a), while tumors implanted in PEG-RDG showed significant reductions in

tumor burden (Figure 5.5a), which resulted in enhanced survival of mice with PEG-RDG tumors treated with CpG (Figure 5.5b). This aligns with an activation of the Th1 response previously absent in these tumors (Figure 5.4). This indicates that vaccine therapy may be optimal for patients with a predominantly Th2 and neutrophil-driven response in the clinic and shows the potential for this technology to demonstrate clinically relevant phenomena.

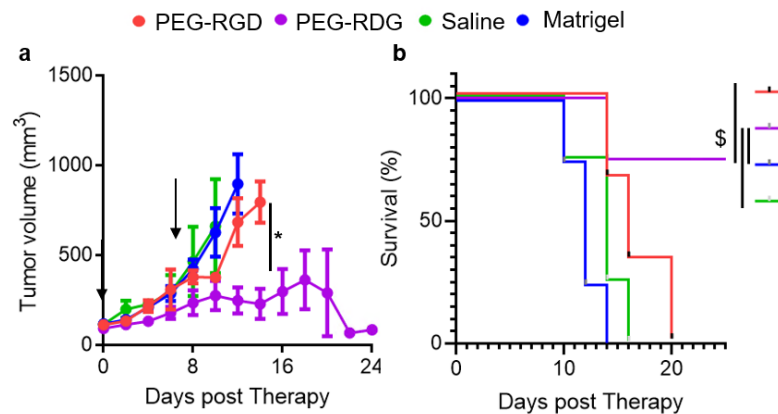


Figure 5.5: Altered tumor immune microenvironments direct responses to cancer vaccine. CpG vaccine responses by tumor volume (a) and survival (b) after i.t. treatment on d0 and 7. Arrows (a) indicate days of treatment. * indicates significance by RM-ANOVA with Tukey's post-hoc test; \$ indicates significance by Log-rank test (*, \$ indicate $p < 0.05$).

5.4 Conclusion

Through this work, we have engineered a novel, *in vivo*, physiologically relevant model of breast cancer for immunotherapeutic testing, which improves upon currently insufficient preclinical models. This system ameliorates limitations with PDXs, as it is much less expensive and tumors form 100% of the time across multiple independent experiments; GEMMs, as both the number of tumors and immune responses against those tumors are consistent and controllable; and current syngeneic models, as the immune response is consistent between batches and can be modulated to more closely mimic

different immune responses observed in clinical samples. This was then tested using a clinically relevant immunotherapy, which revealed that immune infiltration into the tumor altered therapeutic responses to a cancer “vaccine.” As only a subset of human patients respond to immunotherapies, enhancing understanding of what directs responses would be a massive clinical improvement, and would likely enhance patient survival. Thus, by engineering a novel *in vivo* preclinical model, limitations in current models have been addressed, and new understandings of how immunotherapeutic responses are directed can be utilized to enhance breast cancer patient survival.

This system has significant ramifications beyond the current uses as well – because the adhesive ligand within the scaffold can direct immune responses, other adhesive ligands, or immunomodulatory agents, could be tethered to the scaffold to further direct immune responses against the developing tumor. Additionally, this could be applied far beyond breast tumors, particularly to other solid tumor types for which current immunotherapeutic strategies are lacking, in order to better predict immune responses and develop novel, more effective anti-cancer treatments.

CHAPTER 6. CONCLUSIONS

6.1 Conclusions

Solid tumors remain significant clinical problems, affecting millions of people annually. Immunotherapies have evolved as extremely promising tools in the fight against cancer, but only work in a limited subset of patients. Through this work, we have developed two novel engineered biomaterial technologies, a synthetic Ag system and an *in vivo* platform for immunotherapeutic testing. These biomaterial techniques were implemented to better understand the integration of the lymphatic system with the TME and immune system in both breast cancer and melanoma; and how local immune milieu impacts tumor remodeling. Each of these investigations uncovered new knowledge which led to enhanced immunotherapeutic efficacy, of either ICB or cancer vaccine therapy.

6.2 Contributions to the Field

6.2.1 *Improved Understanding of T cell Priming and Immune Responses in Melanoma and TNBC*

The mechanisms underlying T cell priming, along with immune infiltration, in different microenvironments of melanoma and TNBC patients are currently poorly understood [17, 51]. In both Chapter 3 and 4, complex and highly advanced immunological assays (12+ color flow cytometry, adoptive transfer studies, vaccination studies, etc.) are utilized to improve upon currently poor understandings of immunological remodeling in melanoma and breast cancers. Through the use of complex engineered immunological assays, we have generated new knowledge regarding the connections between transport

mechanisms, engineered environments, and the immune system, improving upon these understandings. This led us to uncover changes in T cell priming within different microenvironments across multiple stages of disease development and progression, with potential impacts on immunotherapy implementation. This knowledge was combined with insights into molecular dissemination patterns from the TME and immune infiltration in different organs, providing a broader understanding of the immunological remodeling which occurs in both melanoma and TNBC.

6.2.2 Development of Engineered Biomaterial Tools for Preclinical Study

In this work, two biomaterial systems were developed for the study of immune responses in cancer and applied to two different model systems. The synthetic Ag system which allows for probing of responses to either passively drained species or species actively transported by cells. Currently, analyses of Ag responses utilize systems such as scarification, where a virus or model Ag is placed on scratched skin [80], or Ag-secreting tumor systems, wherein tumor cells are modified to express the Ag of interest [166]. In our system, one peptide Ag sequence is tethered to a NP which accesses the LN via passive drainage or a MP which must be actively phagocytosed by migratory cells to reach the LN. This system has high utility as any peptide Ag can be loaded onto the particle system, and the particles can be injected in any administration route, facilitating the use of this system for a number of applications outside of the work discussed here. We used this synthetic Ag system to focus on the mechanism of transport (passive drainage vs. active, cell-mediated transport) after i.d. or i.t. injection, while avoiding confounding factors which exist in current systems. Several previous studies have investigated using drug carriers to target the LN for melanoma therapy [13, 14]. However, these have mainly focused on harnessing

different routes of administration [13, 14] or the enhanced permeability and retention effect [229]. We used this to provide novel insights into mechanisms of transport and the influence specific carriers have on immune response development, for better immunotherapy responses.

Secondly, we developed a novel *in vivo* platform for immunotherapeutic testing. Each of the current mouse models (PDX, GEMM, syngeneic models) of breast cancer have their own strengths and limitations. Unfortunately, no current system allows for manipulation of the immune cells which infiltrate the tumor at implantation. Thus, comparisons between immune infiltration must be done between different cell lines or mouse strains, which can have very different Ags, mutations, and growth patterns. Through this work, we have generated novel systems to model the breast TME. The same cell line can be used, while generating different immune infiltration responses, and thus a more accurate representation of the variability which exists in human disease. This improved modeling will facilitate improvements in the study of breast tumors, with applicability to other cancer types. This has the potential to provide insight into both personalized medicine as immune infiltration can be compared to responses to different immunotherapeutic regimens, and into the development of more universal immunotherapeutic strategies with potential application to a broader patient population.

6.2.3 Insights into Improved Immunotherapeutic Guidelines for the Treatment of Melanoma and TNBC

Through improved understandings of the tumor immune microenvironment in melanoma and TNBC, insight into transport mechanisms and drug carrier systems, and

engineering of the tumor immune microenvironment, new knowledge will be generated pertinent to optimal immunotherapeutic strategies. Current response rates are limited for both of these cancer types, so improved understanding and engineering of these strategies are likely to improve the overall survival rates for this disease, expanding the efficacy of immunotherapies. Currently, only two ICB treatments are approved for breast cancer therapy, and only as second-line treatment for patients who cannot undergo surgery. As such, there is a need for expanded and improved immunotherapies for this disease. Through the work presented here, important information with the potential to inform the application of immunotherapeutic strategies for TNBC and melanoma has been uncovered. We have revealed the ramifications of mechanism of lymphatic transport on LN-resident immune cell targeting, with the potential to impact drug carrier development; shown the TdLN as a reservoir of breast tumor Ag-specific T cells inducible by targeted ICB delivery; and demonstrated the ramifications of Th1-driven versus neutrophil-driven immune responses on therapeutic outcomes in breast cancer.

6.3 Future Directions

6.3.1 Synthetic Ag System Uses Beyond CD8⁺ T Cell Responses in Melanoma

Future work using the synthetic Ag system developed here could be used in many different applications. CD4⁺ T cells within tumors are predominantly thought of in terms of their regulatory status, but the capacity of CD4⁺ helper T cells to modulate cytolytic CD8⁺ T cell responses is increasingly coming to light [230–232]. CD4⁺ helper T cells not only produce cytokines to modulate the local microenvironment [230], but additionally recruit APCs for CD8⁺ T cell priming and have been shown to mediate tumor rejection

[233]. However, this anti-tumor activity is dependent on the phenotype of CD4⁺ T cells, as Tregs can have opposite effects, suppressing anti-tumor immune responses and are associated with poor survival rates [16, 20, 47, 103, 230, 234, 235]. Thus, modulating phenotype of CD4⁺ T cells represents a potentially important target for immunotherapy. To explore the mechanisms of CD4⁺ T cell activation, inclusion of a CD4⁺ Ag, such as OVA₃₂₃₋₃₃₉, an MHCII Ag in the ovalbumin protein, in combination with OT-II, OVA₃₂₃₋₃₃₉ Ag-specific CD4⁺ T cells could provide further insight into ramifications of lymphatic transport on anti-tumor immune responses. By understanding the mechanisms of CD4⁺ T cell activation, new therapeutic targets could be generated to enhance survival in cancer patients. Additionally, this system could be applied to other pathologies, such as viral responses or autoimmune reactions (i.e. Graft versus host disease), to improve understandings of these additional models.

6.3.2 Targeting TdLN in a surgically relevant setting

In Chapter 4, we demonstrated that targeting ICB therapy to any LN in the tumor-draining basin, i.e. LNs that access tumor Ag, enhanced therapeutic responses and generation of functional anti-tumor CD8⁺ T cells. Of note, during breast tumor resection surgery, the primary (sentinel) TdLN is often resected in order to uncover the pathological status of the LN [5, 198, 236, 237]. We hypothesize that targeting a secondary TdLN would still be functional in the context of sentinel LN resection, as lymphatic transport out of the tumor is diminished at this timepoint. However, expanding this work to investigate the impacts of surgical resection of the primary TdLN on the potential for anti-tumor responses in the secondary TdLN would increase the clinical relevance of this work, and demonstrate whether or not the reservoir of CD8⁺ T cells we identified in the secondary TdLN is

relevant in a surgical setting in which the secondary TdLN no longer accesses the primary TdLN or lymph flow via the lateral lymphatic vessels. Additionally, the impacts of secondary TdLN-directed ICB targeting in a more highly metastatic model, such as the 4T1 cell line syngeneic to Balb/C mice, or in the MMTV-PyMT mouse model, both with or without resection of the primary TdLN, would show whether this targeting strategy leads to control of secondary tumors and expand the clinical relevance of this work. Finally, exploring the impacts of targeting other adjuvant strategies, such as the cancer vaccine used in Chapter 5, to TdLNs, would be of interest as an alternative to ICB to further improve survival rates in breast cancer models.

6.3.3 *Broad Application of In Vivo Engineered Breast Cancer Model*

The *in vivo* model of breast cancer developed here could be expanded in multiple directions. First, integration of alternative adhesive ligands or immunomodulatory proteins would allow for modelling of a diverse range of immune responses, and further applicability of this system to human disease. Some examples include integration of GFOGER, an alternative integrin ligand [238, 239]; or integration of colony stimulating factor to alter myeloid cell infiltration [240]. Developing a broader array of immune-directing hydrogels and integrating them with breast tumors could allow for more closer mimicking of the range of immune responses to human tumors. Alternatively, this system could be applied to a diverse range of solid tumors, such as ovarian cancer and colon cancer, for which immunotherapies have been even more limited in their clinical application. Broadening the applications of this system could have ramifications across a broad range of patient populations, and further help predict the most successful therapies in the clinic.

REFERENCES

1. Koolen PGL, Matos TR, Ibrahim AMS, et al (2017) Recurrence Rates Over 20 Years in the Treatment of Malignant Melanoma: Immediate Versus Delayed Reconstruction. *Plast Reconstr Surg - Glob Open* 5:. <https://doi.org/10.1097/GOX.0000000000001378>
2. Siegel RL, Miller KD, Jemal A (2019) Cancer Statistics, 2019. *CA Cancer J Clin* 69:7–34. <https://doi.org/10.3322/caac.21551>
3. Ferlay J, Soerjomataram I, Dikshit R, et al (2015) Cancer incidence and mortality worldwide: Sources, methods and major patterns in GLOBOCAN 2012. *Int J Cancer* 136:E359–E386. <https://doi.org/10.1002/ijc.29210>
4. Arvold ND, Taghian AG, Niemierko A, et al (2019) Age, Breast Cancer Subtype Approximation, and Local Recurrence After Breast-Conserving Therapy. *J Clin Oncol* 29:3885–3891. <https://doi.org/10.1200/JCO.2011.36.1105>
5. van Roozendall LM, Smit LHM, Duijsens GHNM, et al (2016) Risk of regional recurrence in triple-negative breast cancer patients : a Dutch cohort study. *Breast Cancer Res Treat* 156:465–472. <https://doi.org/10.1007/s10549-016-3757-4>
6. Van Der Burg SH, Arens R, Ossendorp F, et al (2016) Vaccines for established cancer: Overcoming the challenges posed by immune evasion. *Nat Rev Cancer* 16:219–233. <https://doi.org/10.1038/nrc.2016.16>
7. Marra A, Viale G, Curigliano G (2019) Recent advances in triple negative breast cancer: The immunotherapy era. *BMC Med* 17:90. <https://doi.org/10.1186/s12916-019-1326-5>
8. Riley RS, June CH, Langer R, Mitchell MJ (2019) Delivery technologies for cancer immunotherapy. *Nat Rev Drug Discov* 18:175–196. <https://doi.org/10.1038/s41573-018-0006-z>
9. Francis DM, Thomas SN (2017) Progress and opportunities for enhancing the delivery and efficacy of checkpoint inhibitors for cancer immunotherapy. *Adv Drug Deliv Rev* 115:33–42. <https://doi.org/10.1016/j.addr.2017.04.011>
10. Larkin J, Chiarion-Sileni V, Gonzalez R, et al (2015) Combined Nivolumab and Ipilimumab or Monotherapy in Untreated Melanoma. *N Engl J Med* 373:23–34. <https://doi.org/10.1056/NEJMoa1504030>
11. Nanda R, Chow LQM, Dees EC, et al (2016) Pembrolizumab in Patients With Advanced Triple-Negative Breast Cancer: Phase Ib KEYNOTE-012 Study. *J Clin Oncol* 34:2460–2467. <https://doi.org/10.1200/JCO.2015.64.8931>

12. O'Melia MJ, Lund AW, Thomas SN (2019) The Biophysics of Lymphatic Transport: Engineering Tools and Immunological Consequences. *iScience* 22:28–43. <https://doi.org/10.1016/j.isci.2019.11.005>
13. Thomas SN, Vokali E, Lund AW, et al (2014) Targeting the tumor-draining lymph node with adjuvanted nanoparticles reshapes the anti-tumor immune response. *Biomaterials* 35:814–824. <https://doi.org/10.1016/j.biomaterials.2013.10.003>
14. Francis DM, Manspeaker MP, Schudel A, et al (2020) Blockade of immune checkpoints in lymph nodes through locoregional delivery augments cancer immunotherapy. *Sci Transl Med* 12:eaay3575
15. Simoni Y, Becht E, Fehlings M, et al (2018) Bystander CD8+ T cells are abundant and phenotypically distinct in human tumour infiltrates. *Nature* 557:575–579. <https://doi.org/10.1038/s41586-018-0130-2>
16. Huang Y, Ma C, Zhang Q, et al (2015) CD4+ and CD8+ T cells have opposing roles in breast cancer progression and outcome. *Oncotarget* 6:17462–17478
17. Marzagalli M, Ebel ND, Manuel ER (2019) Unraveling the crosstalk between melanoma and immune cells in the tumor microenvironment. *Semin Cancer Biol* 59:236–250. <https://doi.org/10.1016/j.semcancer.2019.08.002>
18. Uzzan B, Nicolas P, Cucherat M, Perret G-Y (2004) Microvessel Density as a Prognostic Factor in Women with Breast Cancer: A Systematic Review of the Literature and Meta-Analysis. *Cancer Res* 64:2941–2955. <https://doi.org/10.1158/0008-5472.CAN-03-1957>
19. Hubert M, Gobbini E, Couillault C, et al (2020) IFN-III is selectively produced by cDC1 and predicts good clinical outcome in breast cancer. *Sci Immunol* 5:eaav3942
20. Bates GJ, Fox SB, Han C, et al (2006) Quantification of Regulatory T Cells Enables the Identification of High-Risk Breast Cancer Patients and Those at Risk of Late Relapse. *J Clin Oncol* 24:5373–5380. <https://doi.org/10.1200/JCO.2006.05.9584>
21. Hamid O, Robert C, Daud A, et al (2013) Safety and Tumor Responses with Lambrolizumab (Anti-PD-1) in Melanoma. *N Engl J Med* 369:134–44. <https://doi.org/10.1056/NEJMoa1305133>
22. Hegde PS, Karanikas V, Evers S (2016) The Where, the When, and the How of Immune Monitoring for Cancer Immunotherapies in the Era of Checkpoint Inhibition. *Clin Cancer Res* 22:1865–1874. <https://doi.org/10.1158/1078-0432.CCR-15-1507>
23. Wishart AL, Conner SJ, Guarin JR, et al (2020) Decellularized extracellular matrix scaffolds identify full-length collagen VI as a driver of breast cancer cell invasion in obesity and metastasis. *Sci Adv* 6:eabc3175

24. Jung K, Heishi T, Incio J, et al (2017) Targeting CXCR4-dependent immunosuppressive Ly6Clow monocytes improves antiangiogenic therapy in colorectal cancer. *Proc Natl Acad Sci* 114:10455–10460. <https://doi.org/10.1073/pnas.1710754114>
25. Galon J, Bruni D (2019) Approaches to treat immune hot, altered and cold tumours with combination immunotherapies. *Nat Rev Drug Discov* 18:197–218. <https://doi.org/10.1038/s41573-018-0007-y>
26. Sharpless NE, DePinho RA (2006) The mighty mouse: genetically engineered mouse models in cancer drug development. *Nat Rev Drug Discov* 5:741–754. <https://doi.org/10.1038/nrd2110>
27. Foulkes WD, Smith IE, Reis-Filho JS (2010) Triple-Negative Breast Cancer. *N Engl J Med* 363:1938–1948
28. Erdag G, Schaefer JT, Smolkin ME, et al (2012) Immunotype and Immunohistologic Characteristics of Tumor-Infiltrating Immune Cells Are Associated with Clinical Outcome in Metastatic Melanoma. *Cancer Res* 72:1070–1080. <https://doi.org/10.1158/0008-5472.CAN-11-3218>
29. Schmid P, Adams S, Rugo HS, et al (2018) Atezolizumab and Nab-Paclitaxel in Advanced Triple-Negative Breast Cancer. *N Engl J Med* 379:2108–2121. <https://doi.org/10.1056/NEJMoa1809615>
30. Murphy K, Weaver C (2017) *Janeway's Immunobiology*, 9th ed. Taylor & Francis, New York, NY
31. Sathaporn S, Robins A, Vassanasiri W, et al (2004) Dendritic cells are dysfunctional in patients with operable breast cancer. *Cancer Immunol Immunother* 53:510–518. <https://doi.org/10.1007/s00262-003-0485-5>
32. Gil Del Alcazar CR, Huh SJ, Ekram MB, et al (2017) Immune Escape in Breast Cancer During In Situ to Invasive Carcinoma Transition. *Cancer Discov* 7:1098–1115. <https://doi.org/10.1158/2159-8290.CD-17-0222>
33. Liyanage UK, Moore TT, Joo H-G, et al (2002) Prevalence of Regulatory T Cells Is Increased in Peripheral Blood and Tumor Microenvironment of Patients with Pancreas or Breast Adenocarcinoma. *J Immunol* 169:2756–2761. <https://doi.org/10.4049/jimmunol.169.5.2756>
34. Danilin S, Merkel AR, Johnson JR, et al (2012) Myeloid-derived suppressor cells expand during breast cancer progression and promote tumor-induced bone destruction. *Oncoimmunology* 1:1484–1494
35. van Pul KM, Vuylsteke RJCLM, van de Ven R, et al (2020) Selectively hampered activation of lymph node-resident dendritic cells precedes profound T cell suppression and metastatic spread in the breast cancer sentinel lymph node. *J*

Immunother Cancer 7:133. <https://doi.org/10.1186/s40425-019-0605-1>

36. Foulds GA, Vadakekolathu J, Abdel-Fatah TMA, et al (2018) Immune-phenotyping and transcriptomic profiling of peripheral blood mononuclear cells from patients with breast cancer: Identification of a 3 gene signature which predicts relapse of triple negative breast cancer. *Front Immunol* 9:2028. <https://doi.org/10.3389/fimmu.2018.02028>
37. Nirschl CJ, Suarez-Farinas M, Izar B, et al (2017) IFN γ -Dependent Tissue-Immune Homeostasis Is Co-opted in the Tumor Microenvironment. *Cell* 170:127–141. <https://doi.org/10.1016/j.cell.2017.06.016>
38. Sade-Feldman M, Yizhak K, Bjorgaard SL, et al (2018) Defining T Cell States Associated with Response to Checkpoint Immunotherapy in Melanoma. *Cell* 175:998–1013. <https://doi.org/10.1016/j.cell.2018.10.038>
39. Obeid JM, Erdag G, Smolkin ME, et al (2016) PD-L1, PD-L2 and PD-1 expression in metastatic melanoma: Correlation with tumor-infiltrating immune cells and clinical outcome. *Oncoimmunology* 5:e123107. <https://doi.org/10.1080/2162402X.2016.1235107>
40. Im SJ, Hashimoto M, Gerner MY, et al (2016) Defining CD8 $^{+}$ T cells that provide the proliferative burst after PD-1 therapy. *Nature* 537:417–421. <https://doi.org/10.1038/nature19330>
41. Miller BC, Sen DR, Al Abosy R, et al (2019) Subsets of exhausted CD8 $^{+}$ T cells differentially mediate tumor control and respond to checkpoint blockade. *Nat Immunol* 20:326–336. <https://doi.org/10.1038/s41590-019-0312-6>
42. Mahmoud SMA, Paish EC, Powe DG, et al (2011) Tumor-Infiltrating CD8 $^{+}$ Lymphocytes Predict Clinical Outcome in Breast Cancer. *J Clin Oncol* 29:1949–1955. <https://doi.org/10.1200/JCO.2010.30.5037>
43. Savas P, Virassamy B, Ye C, et al (2018) Single-cell profiling of breast cancer T cells reveals a tissue-resident memory subset associated with improved prognosis. *Nat Med* 24:986–993. <https://doi.org/10.1038/s41591-018-0078-7>
44. Guo L, Cao C, Goswami S, et al (2020) Tumoral PD-1hiCD8 $^{+}$ T cells are partially exhausted and predict favorable outcome in triple-negative breast cancer. *Clin Sci* 134:711–726. <https://doi.org/10.1042/CS20191261>
45. Crespo J, Sun H, Welling TH, et al (2013) T cell anergy, exhaustion, senescence, and stemness in the tumor microenvironment. *Curr Opin Immunol* 25:214–221. <https://doi.org/10.1016/j.coi.2012.12.003>
46. Abe BT, Macian F (2013) Uncovering the mechanisms that regulate tumor-induced T-cell anergy. *Oncoimmunology* 2:1–2. <https://doi.org/10.4161/onci.22679>

47. Mougiakakos D, Choudhury A, Lladser A, et al (2010) Regulatory T Cells in Cancer. *Adv Cancer Res* 107:57–117. [https://doi.org/10.1016/S0065-230X\(10\)07003-X](https://doi.org/10.1016/S0065-230X(10)07003-X)
48. Beyer M, Schultze JL (2006) Regulatory T cells in cancer. *Blood* 108:804–811. <https://doi.org/10.1182/blood-2006-02-002774>.Supported
49. Guermonprez P, Valladeau J, Zitvogel L, et al (2002) Antigen Presentation and T Cell Stimulation by Dendritic Cells. *Annu Rev Immunol* 20:621–667. <https://doi.org/10.1146/annurev.immunol.20.100301.064828>
50. Najafi M, Hashemi Goradel N, Farhood B, et al (2019) Macrophage polarity in cancer: A review. *J Cell Biochem* 120:2756–2765. <https://doi.org/10.1002/jcb.27646>
51. Tower H, Ruppert M, Britt K (2019) The Immune Microenvironment of Breast Cancer Progression. *Cancers (Basel)* 11:1–15
52. Seidel JA, Otsuka A, Kabashima K (2018) Anti-PD-1 and Anti-CTLA-4 Therapies in Cancer: Mechanisms of Action, Efficacy, and Limitations. *Front Oncol* 8:86. <https://doi.org/10.3389/fonc.2018.00086>
53. Rudd CE, Taylor A, Schneider H (2009) CD28 and CTLA-4 coreceptor expression and signal transduction. *Immunol Rev* 229:12–26. <https://doi.org/10.1111/j.1600-065X.2009.00770.x>
54. Ahn E, Araki K, Hashimoto M, et al (2018) Role of PD-1 during effector CD8 T cell differentiation. *Proc Natl Acad Sci* 115:4749–4754. <https://doi.org/10.1073/pnas.1718217115>
55. Brahmer JR, Tykodi SS, Chow LQM, et al (2012) Safety and Activity of Anti-PD-L1 Antibody in Patients with Advanced Cancer. *N Engl J Med* 366:2455–2465. <https://doi.org/10.1056/NEJMoa1200694>
56. Cortes J, Cescon DW, Rugo HS, et al (2020) Pembrolizumab plus chemotherapy versus placebo plus chemotherapy for previously untreated locally recurrent inoperable or metastatic triple-negative breast cancer (KEYNOTE-355): a randomised, placebo-controlled, double-blind, phase 3 clinical trial. *Lancet* 396:1817–1828. [https://doi.org/10.1016/S0140-6736\(20\)32531-9](https://doi.org/10.1016/S0140-6736(20)32531-9)
57. Kantoff PW, Higano CS, Shore ND, et al (2010) Sipuleucel-T Immunotherapy for Castration-Resistant Prostate Cancer. *N Engl J Med* 363:411–422
58. Andtbacka RHI, Kaufman HL, Collichio F, et al (2015) Talimogene Laherparepvac Improves Durable Response Rate in Patients With Advanced Melanoma. *J Clin Oncol* 33:2780–2788. <https://doi.org/10.1200/JCO.2014.58.3377>
59. Wiseman CL, Kharazi A (2010) Phase I Study with SV-BR-1 Breast Cancer Cell

- Line Vaccine and GMCSF: Clinical Experience in 14 Patients. *Open Breast Cancer J* 2:4–11. <https://doi.org/10.2174/1876817201002010004>
60. Toh U, Sakurai S, Saku S, et al (2020) Early phase II study of mixed 19-peptide vaccine monotherapy for refractory triple-negative breast cancer. *Cancer Sci* 111:2760–2769. <https://doi.org/10.1111/cas.14510>
 61. Wiig H, Swartz MA (2012) Interstitial fluid and lymph formation and transport: Physiological regulation and roles in inflammation and cancer. *Physiol Rev* 92:1005–1060. <https://doi.org/10.1152/physrev.00037.2011>
 62. Huxley VH, Scallan J (2011) Lymphatic fluid: exchange mechanisms and regulation. *J Physiol* 589:2935–2943. <https://doi.org/10.1113/jphysiol.2011.208298>
 63. Dixon JB (2010) Lymphatic Lipid Transport: Sewer or Subway? *Trends Endocrinol Metab* 21:480–487. <https://doi.org/10.1016/j.tem.2010.04.003>
 64. Zawieja DC (2009) Contractile Physiology of Lymphatics. *Lymphat Res Biol* 7:87–96. <https://doi.org/10.1089/lrb.2009.0007>
 65. Rohner NA, Thomas SN (2016) Melanoma growth effects on molecular clearance from tumors and biodistribution into systemic tissues versus draining lymph nodes. *J Control Release* 223:99–108. <https://doi.org/10.1016/j.jconrel.2015.12.027>
 66. Rohner NA, Thomas SN (2017) Flexible Macromolecule versus Rigid Particle Retention in the Injected Skin and Accumulation in Draining Lymph Nodes Are Differentially Influenced by Hydrodynamic Size. *ACS Biomater Sci Eng* 3:153–159. <https://doi.org/10.1021/acsbiomaterials.6b00438>
 67. Mondor I, Jorquera A, Sene C, et al (2016) Clonal Proliferation and Stochastic Pruning Orchestrate Lymph Node Vasculature Remodeling. *Immunity* 45:877–888. <https://doi.org/10.1016/j.immuni.2016.09.017>
 68. Junt T, Moseman EA, Iannacone M, et al (2007) Subcapsular sinus macrophages in lymph nodes clear lymph-borne viruses and present them to antiviral B cells. *Nature* 450:110–114. <https://doi.org/10.1038/nature06287>
 69. Phan TG, Grigorova I, Okada T, Cyster JG (2007) Subcapsular encounter and complement-dependent transport of immune complexes by lymph node B cells. *Nat Immunol* 8:992–1000. <https://doi.org/10.1038/ni1494>
 70. Gerner MY, Torabi-Parizi P, Germain RN (2015) Strategically Localized Dendritic Cells Promote Rapid T Cell Responses to Lymph-Borne Particulate Antigens. *Immunity* 42:172–185. <https://doi.org/10.1016/j.immuni.2014.12.024>
 71. Kastentmüller W, Torabi-Parizi P, Subramanian N, et al (2012) A Spatially-Organized Multicellular Innate Immune Response in Lymph Nodes Limits Systemic Pathogen Spread. *Cell* 150:1235–1248. <https://doi.org/10.1016/j.cell.2012.07.021>

72. Heath WR, Belz GT, Behrens GMN, et al (2004) Cross-presentation, dendritic cell subsets, and the generation of immunity to cellular antigens. *Immunol Rev* 199:9–26
73. Sixt M, Kanazawa N, Selg M, et al (2005) The Conduit System Transports Soluble Antigens from the Afferent Lymph to Resident Dendritic Cells in the T Cell Area of the Lymph Node. *Immunity* 22:19–29. <https://doi.org/10.1016/j.immuni.2004.11.013>
74. Roozendaal R, Mempel TR, Pitcher LA, et al (2009) Conduits Mediate Transport of Low-Molecular-Weight Antigen to Lymph Node Follicles. *Immunity* 30:264–276. <https://doi.org/10.1016/j.immuni.2008.12.014>
75. Gretz JE, Norbury CC, Anderson AO, et al (2000) Lymph-borne Chemokines and Other Low Molecular Weight Molecules Reach High Endothelial Venules via Specialized Conduits While a Functional Barrier Limits Access to the Lymphocyte Microenvironments in Lymph Node Cortex. *J Exp Med* 192:1425–1439. <https://doi.org/10.1084/jem.192.10.1425>
76. Reynoso G V., Weisberg AS, Shannon JP, et al (2019) Lymph node conduits transport virions for rapid T cell activation. *Nat Immunol* 20:602–612. <https://doi.org/10.1038/s41590-019-0342-0>
77. Rantakari P, Auvinen K, Jäppinen N, et al (2015) The endothelial protein PLVAP in lymphatics controls the entry of lymphocytes and antigens into lymph nodes. *Nat Immunol* 16:386–396. <https://doi.org/10.1038/ni.3101>
78. Allan RS, Waithman J, Bedoui S, et al (2006) Migratory Dendritic Cells Transfer Antigen to a Lymph Node-Resident Dendritic Cell Population for Efficient CTL Priming. *Immunity* 25:153–162. <https://doi.org/10.1016/j.immuni.2006.04.017>
79. Thomas SN, Rutkowski JM, Pasquier M, et al (2012) Impaired Humoral Immunity and Tolerance in K14-VEGFR-3-Ig Mice That Lack Dermal Lymphatic Drainage. *J Immunol* 189:2181–2190. <https://doi.org/10.4049/jimmunol.1103545>
80. Loo CP, Nelson NA, Lane RS, et al (2017) Lymphatic Vessels Balance Viral Dissemination and Immune Activation following Cutaneous Viral Infection. *Cell Rep* 20:3176–3187. <https://doi.org/10.1016/j.celrep.2017.09.006>
81. Platt AM, Randolph GJ (2013) *Dendritic Cell Migration Through the Lymphatic Vasculature to Lymph Nodes*, 1st ed. Elsevier Inc.
82. Jackson DG (2016) Lymphatic Regulation of Cellular Trafficking. *J Clin Cell Immunol* 5:. <https://doi.org/10.4172/2155-9899.1000258.Lymphatic>
83. Miteva DO, Rutkowski JM, Dixon JB, et al (2010) Transmural Flow Modulates Cell and Fluid Transport Functions of Lymphatic Endothelium. *Circ Res* 106:920–931. <https://doi.org/10.1161/CIRCRESAHA.109.207274>

84. Russo E, Teijeira A, Vaahomeri K, et al (2016) Intralymphatic CCL21 Promotes Tissue Egress of Dendritic Cells through Afferent Lymphatic Vessels. *Cell Rep* 14:1723–1734. <https://doi.org/10.1016/j.celrep.2016.01.048>
85. Teijeira A, Hunter MC, Russo E, et al (2017) T Cell Migration from Inflamed Skin to Draining Lymph Nodes Requires Intralymphatic Crawling Supported by ICAM-1/LFA-1 Interactions. *Cell Rep* 18:857–865. <https://doi.org/10.1016/j.celrep.2016.12.078>
86. Ulvmar MH, Werth K, Braun A, et al (2014) The atypical chemokine receptor CCRL1 shapes functional CCL21 gradients in lymph nodes. *Nat Immunol* 15:623–630. <https://doi.org/10.1038/ni.2889>
87. Braun A, Worbs T, Moschovakis GL, et al (2011) Afferent lymph-derived T cells and DCs use different chemokine receptor CCR7-dependent routes for entry into the lymph node and intranodal migration. *Nat Immunol* 12:879–887. <https://doi.org/10.1038/ni.2085>
88. Schumann K, Lämmermann T, Bruckner M, et al (2010) Immobilized Chemokine Fields and Soluble Chemokine Gradients Cooperatively Shape Migration Patterns of Dendritic Cells. *Immunity* 32:703–713. <https://doi.org/10.1016/j.immuni.2010.04.017>
89. Gunn MD, Tangemann K, Tam C, et al (1998) A chemokine expressed in lymphoid high endothelial venules promotes the adhesion and chemotaxis of naive T lymphocytes. *Proc Natl Acad Sci* 95:258–263. <https://doi.org/10.1073/pnas.95.1.258>
90. Pham THM, Baluk P, Xu Y, et al (2010) Lymphatic endothelial cell sphingosine kinase activity is required for lymphocyte egress and lymphatic patterning. *J Exp Med* 207:17–27. <https://doi.org/10.1084/jem.20091619>
91. Ito K, Morimoto J, Kihara A, et al (2014) Integrin $\alpha 9$ on lymphatic endothelial cells regulates lymphocyte egress. *Proc Natl Acad Sci* 111:3080–3085. <https://doi.org/10.1073/pnas.1311022111>
92. Mendoza A, Fang V, Chen C, et al (2017) Lymphatic endothelial S1P promotes mitochondrial function and survival in naive T cells. *Nature* 546:158–161. <https://doi.org/10.1038/nature22352>
93. Thomas SN, Rohner NA, Edwards EE (2016) Implications of Lymphatic Transport to Lymph Nodes in Immunity and Immunotherapy. *Annu Rev Biomed Eng* 18:207–233. <https://doi.org/10.1146/annurev-bioeng-101515-014413>
94. Stacker SA, Williams SP, Karnezis T, et al (2014) Lymphangiogenesis and lymphatic vessel remodelling in cancer. *Nat Rev Cancer* 14:159–172. <https://doi.org/10.1038/nrc3677>

95. Karnezis T, Shayan R, Caesar C, et al (2012) VEGF-D Promotes Tumor Metastasis by Regulating Prostaglandins Produced by the Collecting Lymphatic Endothelium. *Cancer Cell* 21:181–195. <https://doi.org/10.1016/j.ccr.2011.12.026>
96. Lund AW, Duraes F V., Hirosue S, et al (2012) VEGF-C Promotes Immune Tolerance in B16 Melanomas and Cross-Presentation of Tumor Antigen by Lymph Node Lymphatics. *Cell Rep* 1:191–199. <https://doi.org/10.1016/j.celrep.2012.01.005>
97. Fankhauser M, Broggi MAS, Potin L, et al (2017) Tumor lymphangiogenesis promotes T cell infiltration and potentiates immunotherapy in melanoma. *Sci Transl Med* 9:eaal4712. <https://doi.org/10.1126/scitranslmed.aal4712>
98. Lund AW, Wagner M, Fankhauser M, et al (2016) Lymphatic vessels regulate immune microenvironments in human and murine melanoma. *J Clin Invest* 126:3389–3402. <https://doi.org/10.1172/JCI79434>
99. Kissenpfennig A, Henri S, Dubois B, et al (2005) Dynamics and Function of Langerhans Cells In Vivo: Dermal Dendritic Cells Colonize Lymph Node Areas Distinct from Slower Migrating Langerhans Cells. *Immunity* 22:643–654. <https://doi.org/10.1016/j.immuni.2005.04.004>
100. Kitano M, Yamazaki C, Takumi A, et al (2016) Imaging of the cross-presenting dendritic cell subsets in the skin-draining lymph node. *Proc Natl Acad Sci* 113:1044–1049. <https://doi.org/10.1073/pnas.1513607113>
101. Baitsch L, Baumgaertner P, Devêvre E, et al (2011) Exhaustion of tumor-specific CD8+ T cells in metastases from melanoma patients. *J Clin Invest* 121:2350–2360. <https://doi.org/10.1172/JCI46102>
102. Liu Z, Kim JH, Falo LDJ, You Z (2009) Tumor Regulatory T Cells Potently Abrogate Antitumor Immunity. *J Immunol* 182:6160–6167. <https://doi.org/10.4049/jimmunol.0802664>
103. Nakamura R, Sakakibara M, Nagashima T, et al (2009) Accumulation of regulatory T cells in sentinel lymph nodes is a prognostic predictor in patients with node-negative breast cancer. *Eur J Cancer* 45:2123–2131. <https://doi.org/10.1016/j.ejca.2009.03.024>
104. Rohner NA, McClain J, Tuell SL, et al (2015) Lymph node biophysical remodeling is associated with melanoma lymphatic drainage. *FASEB J* 29:4512–4522. <https://doi.org/10.1096/fj.15-274761>
105. Riedel A, Shorthouse D, Haas L, et al (2016) Tumor-induced stromal reprogramming drives lymph node transformation. *Nat Immunol* 17:1118–1127. <https://doi.org/10.1038/ni.3492>
106. Hirosue S, Vokali E, Raghavan VR, et al (2014) Steady-State Antigen Scavenging,

- Cross-Presentation, and CD8⁺ T Cell Priming: A New Role for Lymphatic Endothelial Cells. *J Immunol* 192:5002–5011. <https://doi.org/10.4049/jimmunol.1302492>
107. Lane RS, Femel J, Breazeale AP, et al (2018) IFN γ -activated dermal lymphatic vessels inhibit cytotoxic T cells in melanoma and inflamed skin. *J Exp Med* 215:3057–3074. <https://doi.org/10.1084/jem.20180654>
 108. Breitenbach M, Hoffmann J (2018) Editorial: Cancer Models. *Front Oncol* 8:401. <https://doi.org/10.3389/fonc.2018.00401>
 109. Stewart E, Federico SM, Chen X, et al (2017) Orthotopic patient-derived xenografts of paediatric solid tumours. *Nature* 549:96–100. <https://doi.org/10.1038/nature23647>
 110. Capasso A, Lang J, Pitts TM, et al (2019) Characterization of immune responses to anti-PD-1 mono and combination immunotherapy in hematopoietic humanized mice implanted with tumor xenografts. *J Immunother Cancer* 7:1–16. <https://doi.org/10.1186/s40425-019-0518-z>
 111. Wang M, Yao LC, Cheng M, et al (2018) Humanized mice in studying efficacy and mechanisms of PD-1-targeted cancer immunotherapy. *FASEB J* 32:1537–1549. <https://doi.org/10.1096/fj.201700740R>
 112. Snowden E, Porter W, Hahn F, et al (2017) Immunophenotyping and Transcriptomic Outcomes in PDX-Derived TNBC Tissue. *Mol Cancer Res* 15:429–438. <https://doi.org/10.1158/1541-7786.MCR-16-0286-T>
 113. Heyer J, Kwong LN, Lowe SW, Chin L (2010) Non-germline genetically engineered mouse models for translational cancer research. *Nat Rev Cancer* 10:470–480. <https://doi.org/10.1038/nrc2877>
 114. Guy CT, Cardiff RD, Muller WJ (1992) Induction of Mammary Tumors by Expression of Polyomavirus Middle T Oncogene: A Transgenic Mouse Model for Metastatic Disease. *Mol Cell Biol* 12:954–961. <https://doi.org/10.1128/MCB.12.3.954>
 115. Killion JJ, Radinsky R, Fidler IJ (1998) Orthotopic models are necessary to predict therapy of transplantable tumors in mice. *Cancer Metastasis Rev* 17:279–284. <https://doi.org/10.1023/A:1006140513233>
 116. Yu JW, Bhattacharya S, Yanamandra N, et al (2018) Tumor-immune profiling of murine syngeneic tumor models as a framework to guide mechanistic studies and predict therapy response in distinct tumor microenvironments. *PLoS One* 13:e0206223. <https://doi.org/10.1371/journal.pone.0206223>
 117. Mosely SIS, Prime JE, Sainson RCA, et al (2017) Rational Selection of Syngeneic Preclinical Tumor Models for Immunotherapeutic Drug Discovery. *Cancer*

Immunol Res 5:29–41. <https://doi.org/10.1158/2326-6066.CIR-16-0114>

118. O’Melia MJ, Rohner NA, Manspeaker MP, et al (2020) Quality of CD8 + T cell immunity evoked in lymph nodes is compartmentalized by route of antigen transport and functional in tumor context. *Sci Adv* 6:eabd7134
119. Klechevsky E, Morita R, Liu M, et al (2008) Functional Specializations of Human Epidermal Langerhans Cells and CD14+ Dermal Dendritic Cells. *Immunity* 29:497–510. <https://doi.org/10.1016/j.immuni.2008.07.013>
120. De Vries IJM, Krooshoop DJEB, Scharenborg NM, et al (2003) Effective Migration of Antigen-pulsed Dendritic Cells to Lymph Nodes in Melanoma Patients Is Determined by Their Maturation State. *Cancer Res* 63:12–17
121. Hanahan D, Weinberg RA (2011) Hallmarks of Cancer: The Next Generation. *Cell* 144:646–674. <https://doi.org/10.1016/j.cell.2011.02.013>
122. Shields JD, Borsetti M, Rigby H, et al (2004) Lymphatic density and metastatic spread in human malignant melanoma. *Br J Cancer* 90:693–700. <https://doi.org/10.1038/sj.bjc.6601571>
123. Shayan R, Karnezis T, Murali R, et al (2012) Lymphatic vessel density in primary melanomas predicts sentinel lymph node status and risk of metastasis. *Histopathology* 61:702–710. <https://doi.org/10.1111/j.1365-2559.2012.04310.x>
124. Zhang S, Yi S, Zhong D, et al (2017) Intratumoral and peritumoral lymphatic vessel density both correlate with lymph node metastasis in breast cancer. *Sci Rep* 7:40364
125. Mori D, Yamasaki F, Shibaki M, Tokunaga O (2007) Lateral peritumoral lymphatic vessel invasion can predict lymph node metastasis in esophageal squamous cell carcinoma. *Mod Pathol* 20:694–700. <https://doi.org/10.1038/modpathol.3800786>
126. Lin M, Ma S-P, Lin H-Z, et al (2010) Intratumoral as well as peritumoral lymphatic vessel invasion correlates with lymph node metastasis and unfavourable outcome in colorectal cancer. *Clin Exp Metastasis* 27:123–132. <https://doi.org/10.1007/s10585-010-9309-0>
127. Hara T, Makino T, Yamasaki M, et al (2020) Peritumoral Lymphatic Vessels Associated with Resistance to Neoadjuvant Chemotherapy and Unfavorable Survival in Esophageal Cancer. *Ann Surg Oncol* 27:3762–3769
128. Cremasco V, Woodruff MC, Onder L, et al (2014) B cell homeostasis and follicle confines are governed by fibroblastic reticular cells. *Nat Immunol* 15:973–981. <https://doi.org/10.1038/ni.2965>
129. Astarita JL, Cremasco V, Fu J, et al (2015) The CLEC-2-podoplanin axis controls the contractility of fibroblastic reticular cells and lymph node microarchitecture. *Nat Immunol* 16:75–84. <https://doi.org/10.1038/ni.3035>

130. Lu P, Weaver VM, Werb Z (2012) The extracellular matrix: A dynamic niche in cancer progression. *J Cell Biol* 196:395–406. <https://doi.org/10.1083/jcb.201102147>
131. Pickup MW, Mouw JK, Weaver VM (2014) The extracellular matrix modulates the hallmarks of cancer. *EMBO Rep* 15:1243–1253
132. Maarouf OH, Uehara M, Kainath V, et al (2018) Repetitive ischemic injuries to the kidneys result in lymph node fibrosis and impaired healing. *JCI Insight* 3:1–17. <https://doi.org/10.1172/jci.insight.120546>
133. Huang L, Deng J, Xu W, et al (2018) CD8+ T cells with high TGF- β 1 expression cause lymph node fibrosis following HIV infection. *Mol Med Rep* 18:77–86. <https://doi.org/10.3892/mmr.2018.8964>
134. Kityo C, Makamdop KN, Rothenberger M, et al (2018) Lymphoid tissue fibrosis is associated with impaired vaccine responses. *J Clin Invest* 128:2763–2773
135. van der Vlies AJ, O’Neil CP, Hasegawa U, et al (2010) Synthesis of Pyridyl Disulfide-Functionalized Nanoparticles for Conjugating Thiol-Containing Small Molecules, Peptide, and Proteins. *Bioconjug Chem* 21:653–662
136. Fletcher AL, Malhotra D, Turley SJ (2011) Lymph node stroma broaden the peripheral tolerance paradigm. *Trends Immunol* 32:12–18. <https://doi.org/10.1016/j.it.2010.11.002>
137. Broggi MAS, Schmalzer M, Lagarde N, Ross SW (2014) Isolation of Murine Lymph Node Stromal Cells. *J Vis Exp* e51803. <https://doi.org/10.3791/51803>
138. Inaba K, Turley S, Yamaide F, et al (1998) Efficient Presentation of Phagocytosed Cellular Fragments on the Major Histocompatibility Complex Class II Products of Dendritic Cells. *J Exp Med* 188:2163–2173. <https://doi.org/10.1084/jem.188.11.2163>
139. Kim IS, Gao Y, Welte T, et al (2019) Immuno-subtyping of breast cancer reveals distinct myeloid cell profiles and immunotherapy resistance mechanisms. *Nat Cell Biol* 21:1113–1126. <https://doi.org/10.1038/s41556-019-0373-7>
140. Hirosue S, Kourtis IC, van der Vlies AJ, et al (2010) Antigen delivery to dendritic cells by poly(propylene sulfide) nanoparticles with disulfide conjugated peptides: Cross-presentation and T cell activation. *Vaccine* 28:7897–7906. <https://doi.org/10.1016/j.vaccine.2010.09.077>
141. Jeanbart L, Ballester M, de Titta A, et al (2014) Enhancing Efficacy of Anticancer Vaccines by Targeted Delivery to Tumor-Draining Lymph Nodes. *Cancer Immunol Res* 2:436–447. <https://doi.org/10.1158/2326-6066.CIR-14-0019-T>
142. Porgador A, Yewdell JW, Deng Y, et al (1997) Localization, Quantitation, and In

- Situ Detection of Specific Peptide-MHC Class I Complexes Using a Monoclonal Antibody. *Immunity* 6:715–726. [https://doi.org/10.1016/S1074-7613\(00\)80447-1](https://doi.org/10.1016/S1074-7613(00)80447-1)
143. Stoitzner P, Tripp CH, Eberhart A, et al (2006) Langerhans cells cross-present antigen derived from skin. *Proc Natl Acad Sci* 103:7783–7788. <https://doi.org/10.1073/pnas.0509307103>
 144. Colonna M, Trinchieri G, Liu Y-J (2004) Plasmacytoid dendritic cells in immunity. *Nat Immunol* 5:1219–1226. <https://doi.org/10.1038/ni1141>
 145. Reddy ST, Rehor A, Schmoekel HG, et al (2006) In vivo targeting of dendritic cells in lymph nodes with poly(propylene sulfide) nanoparticles. *J Control Release* 112:26–34. <https://doi.org/10.1016/j.jconrel.2006.01.006>
 146. Schudel A, Sestito LF, Thomas SN (2018) S-nitrosated poly(propylene sulfide) nanoparticles for enhanced nitric oxide delivery to lymphatic tiss. *J Biomed Mater Res - Part A* 106A:1463–1475. <https://doi.org/10.1002/jbm.a.36348>
 147. Schudel A, Chapman AP, Yau M-K, et al (2020) Programmable multistage drug delivery to lymph nodes. *Nat Nanotechnol* 15:491–499. <https://doi.org/10.1038/s41565-020-0679-4>
 148. Wollenberg A, Mommaas M, Oppel T, et al (2002) Expression and Function of the Mannose Receptor CD206 on Epidermal Dendritic Cells in Inflammatory Skin Diseases. *J Invest Dermatol* 118:327–334. <https://doi.org/10.1046/j.0022-202x.2001.01665.x>
 149. Gupta PK, Godec J, Wolski D, et al (2015) CD39 Expression Identifies Terminally Exhausted CD8+ T Cells. *PLoS Pathog* 11:1–21. <https://doi.org/10.1371/journal.ppat.1005177>
 150. Kaech SM, Ahmed R (2001) Memory CD8+ T cell differentiation: initial antigen encounter triggers a developmental program in naive cells. *Nat Immunol* 2:415–422. <https://doi.org/10.1038/87720.Memory>
 151. Horton BL, Williams JB, Cabanov A, et al (2018) Intratumoral CD8+ T-Cell Apoptosis is a Major Component of T-Cell Dysfunction and Impedes Antitumor Immunity. *Cancer Immunol Res* 6:14–24. <https://doi.org/10.1158/2326-6066.CIR-17-0249>
 152. Davidson S, Efremova M, Riedel A, et al (2020) Single-Cell RNA Sequencing Reveals a Dynamic Stromal Niche That Supports Tumor Growth. *Cell Rep* 31:107628. <https://doi.org/10.1016/j.celrep.2020.107628>
 153. Kim MK, Kim J (2019) Properties of immature and mature dendritic cells: phenotype, morphology, phagocytosis, and migration. *RSC Adv* 9:11230–11238. <https://doi.org/10.1039/C9RA00818G>

154. Gerner MY, Mescher MF (2009) Antigen Processing and MHC-II Presentation by Dermal and Tumor-Infiltrating Dendritic Cells. *J Immunol* 182:2726–2737. <https://doi.org/10.4049/jimmunol.0803479>
155. Clausen BE, Stoitzner P (2015) Functional specialization of skin dendritic cell subsets in regulating T cell responses. *Front Immunol* 6:534. <https://doi.org/10.3389/fimmu.2015.00534>
156. Munn DH, Sharma MD, Hou D, et al (2004) Expression of indoleamine 2,3-dioxygenase by plasmacytoid dendritic cells in tumor-draining lymph nodes. *J Clin Invest* 114:280–290. <https://doi.org/10.1172/JCI200421583.280>
157. Essner R, Kojima M (2002) Dendritic cell function in sentinel nodes. *Oncol* 16:27–31
158. Malhotra D, Fletcher AL, Astarita J, et al (2012) Transcriptional profiling of stroma from inflamed and resting lymph nodes defines immunological hallmarks. *Nat Immunol* 13:499–510. <https://doi.org/10.1038/ni.2262>
159. Binnewies M, Roberts EW, Kersten K, et al (2018) Understanding the tumor immune microenvironment (TIME) for effective therapy. *Nat Med* 24:541–550. <https://doi.org/10.1038/s41591-018-0014-x>
160. Jansen CS, Prokhnevskaya N, Master VA, et al (2019) An intra-tumoral niche maintains and differentiates stem-like CD8 T cells. *Nature* 576:465–470. <https://doi.org/10.1038/s41586-019-1836-5>
161. Stylianopoulos T, Economides E-A, Baish JW, et al (2015) Towards Optimal Design of Cancer Nanomedicines: Multi-stage Nanoparticles for the Treatment of Solid Tumors. *Ann Biomed Eng* 43:2291–2300. <https://doi.org/10.1007/s10439-015-1276-9>
162. Taube JM, Klein A, Brahmer JR, et al (2014) Association of PD-1, PD-1 Ligands, and Other Features of the Tumor Immune Microenvironment with Response to Anti-PD-1 Therapy. *Clin Cancer Res* 20:5064–5074. <https://doi.org/10.1158/1078-0432.CCR-13-3271>
163. Sharma P, Allison JP (2015) The future of immune checkpoint therapy. *Science* (80-) 348:56–61. <https://doi.org/10.1126/science.aaa8172>
164. O’Melia MJ, Manspecker MP, Thomas SN (2021) Tumor-draining lymph nodes are survival niches that support T cell priming against lymphatic transported tumor antigen and effects of immune checkpoint blockade in TNBC. *Cancer Immunol Immunother*. <https://doi.org/10.1007/s00262-020-02792-5>
165. Wang T, Wang C, Wu J, et al (2017) The Different T-cell Receptor Repertoires in Breast Cancer Tumors, Draining Lymph Nodes, and Adjacent Tissues. *Cancer Immunol Res* 5:148–157. <https://doi.org/10.1158/2326-6066.CIR-16-0107>

166. Crosby EJ, Wei J, Yang XY, et al (2017) Complimentary mechanisms of dual checkpoint blockade expand unique T-cell repertoires and activate adaptive anti-tumor immunity in triple-negative breast tumors. *Oncoimmunology* 7:e1421891. <https://doi.org/10.1080/2162402x.2017.1421891>
167. Shiota T, Miyasato Y, Ohnishi K, et al (2016) The Clinical Significance of CD169-Positive Lymph Node Macrophage in Patients with Breast Cancer. *PLoS One* 11:1–13. <https://doi.org/10.1371/journal.pone.0166680>
168. Reddy ST, Van Der Vlies AJ, Simeoni E, et al (2007) Exploiting lymphatic transport and complement activation in nanoparticle vaccines. *Nat Biotechnol* 25:1159–1164. <https://doi.org/10.1038/nbt1332>
169. Chang AY, Bhattacharya N, Mu J, et al (2013) Spatial organization of dendritic cells within tumor draining lymph nodes impacts clinical outcome in breast cancer patients. *J Transl Med* 11:1–12
170. Duvall CL, Taylor WR, Weiss D, Gulberg RE (2004) Quantitative microcomputed tomography analysis of collateral vessel development after ischemic injury. *Am J Physiol - Hear Circ Physiol* 287:H302–H310. <https://doi.org/10.1152/ajpheart.00928.2003>
171. Li X, Li M, Lian Z, et al (2016) Prognostic Role of Programmed Death Ligand-1 Expression in Breast Cancer: A Systematic Review and Meta-Analysis. *Target Oncol* 11:753–761. <https://doi.org/10.1007/s11523-016-0451-8>
172. Green DR, Droin N, Pinkoski M (2003) Activation-induced cell death in T cells. *Immunol Rev* 193:70–81. <https://doi.org/10.1034/j.1600-065X.2003.00051.x>
173. Kabelitz D, Pohl T, Pechhold K (1993) Activation-induced cell death (apoptosis) of mature peripheral T lymphocytes. *Trends Immunol* 14:338–339
174. Ucker DS, Hebshi LD, Blomquist JE, Torbett BE (1994) Physiological T-Cell Death: Susceptibility is Modulated by Activation, Aging, and Transformation, but the Mechanism is Constant. *Immunol Rev* 142:273–299. <https://doi.org/10.1111/j.1600-065X.1994.tb00893.x>
175. Hanahan D, Weinberg RA (2000) The Hallmarks of Cancer. *Cell* 100:57–70. <https://doi.org/10.1007/s00262-010-0968-0>
176. Shibuya M (2011) Vascular Endothelial Growth Factor (VEGF) and Its Receptor (VEGFR) Signaling in Angiogenesis: A Crucial Target for Anti- and Pro-Angiogenic Therapies. *Genes and Cancer* 2:1097–1105. <https://doi.org/10.1177/1947601911423031>
177. Carmeliet P, Jain RK (2011) Principles and mechanisms of vessel normalization for cancer and other angiogenic diseases. *Nat Rev Drug Discov* 10:417–427

178. Nagy JA, Dvorak AM, Dvorak HF (2012) Vascular Hyperpermeability, Angiogenesis, and Stroma Generation. *Cold Spring Harb Perspect Med* 2:1–14. <https://doi.org/10.1101/cshperspect.a006544>
179. Nagy JA, Feng D, Vasile E, et al (2006) Permeability properties of tumor surrogate blood vessels induced by VEGF-A. *Lab Invest* 86:767–780. <https://doi.org/10.1038/labinvest.3700436>
180. Schneider BP, Gray RJ, Radovich M, et al (2013) Prognostic and Predictive Value of Tumor Vascular Endothelial Growth Factor Gene Amplification in Metastatic Breast Cancer Treated with Paclitaxel with and without Bevacizumab; Results from ECOG 2100 Trial. *Clin Cancer Res* 19:1281–1289. <https://doi.org/10.1158/1078-0432.CCR-12-3029>
181. Su J-C, Mar A-C, Wu S-H, et al (2016) Disrupting VEGF-A paracrine and autocrine loops by targeting SHP-1 suppresses triple negative breast cancer metastasis. *Sci Rep* 6:28888. <https://doi.org/10.1038/srep28888>
182. Bahnassy A, Mohanad M, Ismail MF, et al (2015) Molecular biomarkers for prediction of response to treatment and survival in triple negative breast cancer patients from Egypt. *Exp Mol Pathol* 99:303–311. <https://doi.org/10.1016/j.yexmp.2015.07.014>
183. Sweat RS, Sloas DC, Murfee WL (2014) VEGF-C Induces Lymphangiogenesis and Angiogenesis in the Rat Mesentery Culture Model. *Microcirculation* 21:532–540. <https://doi.org/10.1111/micc.12132>
184. Vaahtomeri K, Karaman S, Mäkinen T, Alitalo K (2017) Lymphangiogenesis guidance by paracrine and pericellular factors. *Genes Dev* 31:1615–1634. <https://doi.org/10.1101/gad.303776.117>
185. Pucci F, Garris C, Lai CP, et al (2016) SCS macrophages suppress melanoma by restricting tumor-derived vesicle-B cell interactions. *Science* (80-) 352:242–246. <https://doi.org/10.1126/science.aaf1328>
186. Hood JL, San Roman S, Wickline SA (2011) Exosomes Released by Melanoma Cells Prepare Sentinel Lymph Nodes for Tumor Metastasis. *Cancer Res* 71:3792–3801. <https://doi.org/10.1158/0008-5472.CAN-10-4455>
187. Broggi MAS, Maillat L, Clement CC, et al (2019) Tumor-associated factors are enriched in lymphatic exudate compared to plasma in metastatic melanoma patients. *J Exp Med* 216:1091–1107. <https://doi.org/10.1084/jem.20181618>
188. Spranger S, Spaapen RM, Zha Y, et al (2013) Up-Regulation of PD-L1, IDO, and Tregs in the Melanoma Tumor Microenvironments Is Driven by CD8+ T Cells. *Sci Transl Med* 5:200ra116. <https://doi.org/10.1126/scitranslmed.3006504>
189. Schineis P, Runge P, Halin C (2019) Cellular traffic through afferent lymphatic

- vessels. *Vascul Pharmacol* 112:31–41. <https://doi.org/10.1016/j.vph.2018.08.001>
190. Harrell MI, Iritani BM, Ruddell A (2008) Lymph Node Mapping in the Mouse. *J Immunol Methods* 332:170–174. <https://doi.org/10.1016/j.jim.2007.11.012>
 191. Cabrita R, Lauss M, Sanna A, et al (2020) Tertiary lymphoid structures improve immunotherapy and survival in melanoma. *Nature* 577:561–565. <https://doi.org/10.1038/s41586-019-1914-8>
 192. Petitprez F, de Reyniès A, Keung EZ, et al (2020) B cells are associated with survival and immunotherapy response in sarcoma. *Nature* 577:556–560. <https://doi.org/10.1038/s41586-019-1906-8>
 193. Cursiefen C, Chen L, Borges LP, et al (2004) VEGF-A stimulates lymphangiogenesis and hemangiogenesis in inflammatory neovascularization via macrophage recruitment. *J Clin Invest* 113:1040–1050. <https://doi.org/10.1172/JCI200420465.1040>
 194. Hirakawa S, Kodama S, Kunstfeld R, et al (2005) VEGF-A induces tumor and sentinel lymph node lymphangiogenesis and promotes lymphatic metastasis. *J Exp Med* 201:1089–1099. <https://doi.org/10.1084/jem.20041896>
 195. Halin C, Tobler NE, Vigl B, et al (2007) VEGF-A produced by chronically inflamed tissue induces lymphangiogenesis in draining lymph nodes. *Blood* 110:3158–3167. <https://doi.org/10.1182/blood-2007-01-066811>
 196. Rahma OE, Hodi FS (2019) The Intersection between Tumor Angiogenesis and Immune Suppression. *Clin Cancer Res* 25:5449–5457. <https://doi.org/10.1158/1078-0432.CCR-18-1543>
 197. Naik AM, Fey J, Gemignani M, et al (2004) The Risk of Axillary Relapse After Sentinel Lymph Node Biopsy for Breast Cancer Is Comparable With That of Axillary Lymph Node Dissection. *Ann Surg* 240:462–471. <https://doi.org/10.1097/01.sla.0000137130.23530.19>
 198. Pesce C, Morrow M (2013) The Need for Lymph Node Dissection in Nonmetastatic Breast Cancer. *Annu Rev Med* 64:119–129. <https://doi.org/10.1146/annurev-med-052511-135500>
 199. Giuliano AE, Hunt KK, Ballman K V., et al (2011) Axillary Dissection vs No Axillary Dissection in Women With Invasive Breast Cancer and Sentinel Node Metastasis. *J Am Med Assoc* 305:569–575. <https://doi.org/10.1001/jama.2011.90>
 200. Sung H, Ferlay J, Siegel RL, et al (2021) Global cancer statistics 2020: GLOBOCAN estimates of incidence and mortality worldwide for 36 cancers in 185 countries. *CA Cancer J Clin* 0:1–41. <https://doi.org/10.3322/caac.21660>
 201. DeNardo DG, Brennan DJ, Rexhepaj E, et al (2011) Leukocyte Complexity Predicts

- Breast Cancer Survival and Functionally Regulates Response to Chemotherapy. *Cancer Discov* 1:0F54-0F67. <https://doi.org/10.1158/2159-8274.CD-10-0028>
202. Sun S, Fei X, Mao Y, et al (2014) PD-1+ immune cell infiltration inversely correlates with survival of operable breast cancer patients. *Cancer Immunol Immunother* 63:395–406. <https://doi.org/10.1007/s00262-014-1519-x>
 203. Lin EY, Jones JG, Li P, et al (2003) Progression to Malignancy in the Polyoma Middle T Oncoprotein Mouse Breast Cancer Model Provides a Reliable Model for Human Diseases. *Am J Pathol* 163:2113–26. [https://doi.org/10.1016/S0002-9440\(10\)63568-7](https://doi.org/10.1016/S0002-9440(10)63568-7)
 204. Qiu TH, Chandramouli GVR, Hunter KW, et al (2004) Global expression profiling identifies signatures of tumor virulence in MMTV-PyMT-transgenic mice: Correlation to human disease. *Cancer Res* 64:5973–5981. <https://doi.org/10.1158/0008-5472.CAN-04-0242>
 205. Lifsted T, Le Voyer T, Williams M, et al (1998) Identification of inbred mouse strains harboring genetic modifiers of mammary tumor age of onset and metastatic progression. *Int J Cancer* 77:640–644. [https://doi.org/10.1002/\(SICI\)1097-0215\(19980812\)77:4<640::AID-IJC26>3.0.CO;2-8](https://doi.org/10.1002/(SICI)1097-0215(19980812)77:4<640::AID-IJC26>3.0.CO;2-8)
 206. Bao L, Matsumura Y, Baban D, et al (1994) Effects of inoculation site and Matrigel on growth and metastasis of human breast cancer cells. *Br J Cancer* 70:228–232. <https://doi.org/10.1038/bjc.1994.284>
 207. Olingy CE, et al Pseudotime Analysis of Temporal Immune Cell Recruitment to Synthetic Hydrogels. *In preparation*.
 208. Cruz-Acuña R, Quirós M, Huang S, et al (2018) PEG-4MAL hydrogels for human organoid generation, culture, and in vivo delivery. *Nat Protoc* 13:2102–2119. <https://doi.org/10.1038/s41596-018-0036-3>
 209. Kleinman HK, Martin GR (2005) Matrigel: Basement membrane matrix with biological activity. *Semin Cancer Biol* 15:378–386. <https://doi.org/10.1016/j.semcancer.2005.05.004>
 210. Benton G, Arnaoutova I, George J, et al (2014) Matrigel: From discovery and ECM mimicry to assays and models for cancer research. *Adv Drug Deliv Rev* 79:3–18. <https://doi.org/10.1016/j.addr.2014.06.005>
 211. Biswas T, Gu X, Yang J, et al (2014) Attenuation of TGF- β signaling supports tumor progression of a mesenchymal-like mammary tumor cell line in a syngeneic murine model. *Cancer Lett* 346:129–138. <https://doi.org/10.1016/j.canlet.2013.12.018>
 212. Boehm JS, Hahn WC (2004) Immortalized cells as experimental models to study cancer. *Cytotechnology* 45:47–59. <https://doi.org/10.1007/s10616-004-5125-1>

213. Weaver JD, Headen DM, Aquart J, et al (2017) Vasculogenic hydrogel enhances islet survival, engraftment, and function in leading extrahepatic sites. *Sci Adv* 3:e1700184. <https://doi.org/10.1126/sciadv.1700184>
214. Keselowsky BG, Collard DM, García AJ (2003) Surface chemistry modulates fibronectin conformation and directs integrin binding and specificity to control cell adhesion. *J Biomed Mater Res - Part A* 66A:247–259. <https://doi.org/10.1002/jbm.a.10537>
215. Reyes CD, Petrie TA, García AJ (2008) Mixed Extracellular Matrix Ligands Synergistically Modulate Integrin Adhesion and Signaling. *J Cell Physiol* 217:450–458. <https://doi.org/10.1002/jcp.21512>
216. Petrie TA, Raynor JE, Dumbauld DW, et al (2010) Multivalent Integrin-Specific Ligands Enhance Tissue Healing and Biomaterial Integration. *Sci Transl Med* 2:45ra60. <https://doi.org/10.1126/scitranslmed.3001002>
217. Phelps EA, Enemchukwu NO, Fiore VF, et al (2012) Maleimide Cross-Linked Bioactive PEG Hydrogel Exhibits Improved Reaction Kinetics and Cross-Linking for Cell Encapsulation and In Situ Delivery. *Adv Mater* 24:64–70. <https://doi.org/10.1002/adma.201103574>
218. Aisenbrey EA, Murphy WL (2020) Synthetic alternatives to Matrigel. *Nat Rev Mater*. <https://doi.org/10.1038/s41578-020-0199-8>
219. Lee TT, García JR, Paez JI, et al (2015) Light-triggered in vivo activation of adhesive peptides regulates cell adhesion, inflammation and vascularization of biomaterials. *Nat Mater* 14:352–360. <https://doi.org/10.1038/nmat4157>
220. Miroshnikova YA, Rozenberg GI, Cassereau L, et al (2017) $\alpha 5\beta 1$ -Integrin promotes tension-dependent mammary epithelial cell invasion by engaging the fibronectin synergy site. *Mol Biol Cell* 28:2958–2977. <https://doi.org/10.1091/mbc.E17-02-0126>
221. Han WM, Anderson SE, Mohiuddin M, et al (2018) Synthetic matrix enhances transplanted satellite cell engraftment in dystrophic and aged skeletal muscle with comorbid trauma. *Sci Adv* 4:ear4008. <https://doi.org/10.1126/sciadv.aar4008>
222. Ito M, Hiramatsu H, Kobayashi K, et al (2002) Nod/scid/gamma mouse: an excellent recipient mouse model for engraftment of human cells. *Bone* 100:3175–3182. <https://doi.org/10.1182/blood-2001-12-0207>.Supported
223. Raphael I (2016) T cell subsets and their signature cytokines in autoimmune and inflammatory diseases. *Physiol Behav* 176:100–106. <https://doi.org/10.1016/j.cyto.2014.09.011.T>
224. Ostrand-Rosenberg S, Sinha P, Beury DW, Clements VK (2012) Cross-talk between myeloid-derived suppressor cells (MDSC), macrophages, and dendritic cells

- enhances tumor-induced immune suppression. *Semin Cancer Biol* 22:275–281. <https://doi.org/10.1016/j.semcancer.2012.01.011>
225. Bronte V, Brandau S, Chen SH, et al (2016) Recommendations for myeloid-derived suppressor cell nomenclature and characterization standards. *Nat Commun* 7:12150. <https://doi.org/10.1038/ncomms12150>
226. Jahchan NS, Mujal AM, Pollack JL, et al (2019) Tuning the Tumor Myeloid Microenvironment to Fight Cancer. *Front Immunol* 10:1611. <https://doi.org/10.3389/fimmu.2019.01611>
227. Damuzzo V, Pinton L, Desantis G, et al (2015) Complexity and Challenges in Defining Myeloid-Derived Suppressor Cells. *Cytom Part B - Clin Cytom* 88:77–91. <https://doi.org/10.1002/cyto.b.21206>
228. Scapini P, Laudanna C, Pinardi C, et al (2001) Neutrophils produce biologically active macrophage inflammatory protein-3 α (MIP-3 α)/CCL20 and MIP-3 β /CCL19. *Eur J Immunol* 31:1981–1988. [https://doi.org/10.1002/1521-4141\(200107\)31:7<1981::AID-IMMU1981>3.0.CO;2-X](https://doi.org/10.1002/1521-4141(200107)31:7<1981::AID-IMMU1981>3.0.CO;2-X)
229. Iyer AK, Khaled G, Fang J, Maeda H (2006) Exploiting the enhanced permeability and retention effect for tumor targeting. *Drug Discov Today* 11:812–818. <https://doi.org/10.1016/j.drudis.2006.07.005>
230. Kim H-J, Cantor H (2014) CD4 T-cell Subsets and Tumor Immunity: The Helpful and the Not-so-Helpful. *Cancer Immunol Res* 2:91–98. <https://doi.org/10.1158/2326-6066.CIR-13-0216>
231. Tay RE, Richardson EK, Toh HC (2020) Revisiting the role of CD4+ T cells in cancer immunotherapy—new insights into old paradigms. *Cancer Gene Ther* 5–17. <https://doi.org/10.1038/s41417-020-0183-x>
232. Borst J, Ahrends T, Bąbala N, et al (2018) CD4+ T cell help in cancer immunology and immunotherapy. *Nat Rev Immunol* 18:635–647. <https://doi.org/10.1038/s41577-018-0044-0>
233. Qin Z, Blankenstein T (2000) CD4 T Cell-Mediated Tumor Rejection Involves Inhibition of Angiogenesis that Is Dependent on IFN Receptor Expression by Nonhematopoietic Cells. *Immunity* 12:677–686
234. Kamada T, Togashi Y, Tay C, et al (2019) PD-1+ regulatory T cells amplified by PD-1 blockade promote hyperprogression of cancer. *Proc Natl Acad Sci* 116:9999–100008. <https://doi.org/10.1073/pnas.1822001116>
235. Shang B, Liu Y, Jiang S, Liu Y (2015) Prognostic value of tumor-infiltrating FoxP3+ regulatory T cells in cancers: a systematic review and meta-analysis. *Sci Rep* 5:15179. <https://doi.org/10.1038/srep15179>

236. Julian TB, Dusi D, Wolmark N (2002) Sentinel node biopsy after neoadjuvant chemotherapy for breast cancer. *Am J Surg* 184:315–317
237. Naik SH, Corcoran LM, Wu L (2005) Development of murine plasmacytoid dendritic cell subsets. *Immunol Cell Biol* 83:563–570. <https://doi.org/10.1111/j.1440-1711.2005.01390.x>
238. Emsley J, Knight CG, Farndale RW, Barnes MJ (2004) Structure of the Integrin $\alpha 2\beta 1$ -binding Collagen Peptide. *J Mol Biol* 335:1019–1028. <https://doi.org/10.1016/j.jmb.2003.11.030>
239. Knight CG, Morton LF, Onley DJ, et al (1998) Identification in collagen type I of an integrin $\alpha 2\beta 1$ -binding site containing an essential GER sequence. *J Biol Chem* 273:33287–33294. <https://doi.org/10.1074/jbc.273.50.33287>
240. Stanley ER, Chitu V (2014) CSF-1 receptor signaling in myeloid cells. *Cold Spring Harb Perspect Biol* 6:1–21. <https://doi.org/10.1101/cshperspect.a021857>